DIFFUSING COLLOIDAL PROBES OF BIOSPECIFIC INTERACTIONS AND BIOLOGICAL INTERFACES

by
Gregg Anthony Duncan

A dissertation submitted to the Johns Hopkins University in conformity with the requirements for the degree of Doctor of Philosophy

Department of Chemical and Biomolecular Engineering
Johns Hopkins University
Baltimore, MD 21218
May 2014

ABSTRACT

Diffusing Colloidal Probes of Biospecific Interactions and Biological Interfaces
May 2014

Gregg Anthony Duncan, B.S., Florida State University

Weak, biospecific and non-specific macromolecular interactions play a major role in fundamental biological process such as cell adhesion, motility, and signaling and in medicine, macromolecules have been integrated into materials for drug delivery and tissue engineering applications. Direct measurements capable of sensitively detecting weak, specific and non-specific macromolecular interactions at interfaces are needed to better understand their function in biological systems and utility in biomaterials. In this dissertation, diffusing colloidal probe microscopy (DCPM) was used to make direct, quantitative measurements of colloidal interactions mediated by weak, specific protein-carbohydrate interactions and interactions with the surface of live cells mediated by specific and non-specific macromolecular interactions. In addition, models were developed capable of predicting colloid and surface interactions mediated by specific biomolecular interactions with direct input of binding affinities for further characterization of experimental results.

To study reversible protein-carbohydrate interactions, biospecific adsorption of the sugar-binding protein, Concanavalin A (ConA), to dextran-modified colloidal particles was visualized using fluorescent confocal microscopy and colloidal association dynamics mediated by ConA-dextran interactions were quantified using optical video microscopy. Our results demonstrate how aggregation kinetics in colloidal dispersions can be reversibly tuned with competitive ConA-glucose interactions. Direct connections

were established between the observed aggregation kinetics and net particle-particle interactions as a function of ConA and glucose concentration. To model this system, Monte Carlo simulations were developed to model bulk and interfacial biomacromolecular binding. With direct input of dissociation constants, particle-particle interactions were predicted for a range of binding affinities and protein concentrations.

Dark field video microscopy was used to study interactions between live cells and colloidal particles functionalized with natural and synthetic macromolecules all with relevance to bioengineering. With combined real-time particle tracking and cell boundary determination, particle trajectories can be monitored in relation to their distance from cell surfaces. Particle-cell surface binding lifetimes and potentials of mean force were measured for colloids functionalized with polyethylene glycol (PEG), bovine serum albumin (BSA), dextran, and hyaluronic acid (HA). With the modeling tools developed for colloidal interactions mediated by biospecific binding, the interactions of targeted drug delivery nanoparticles with cell surfaces were characterized for target membrane proteins with varying binding affinities and expression levels. These results provide a basis for in-depth characterization of biomolecular interactions and biophysical properties of cell surfaces with a combination of experimental and modeling techniques.

Committee: Prof. Michael Bevan (Chemical and Biomolecular Engineering, Advisor)
Prof. Joelle Frechette (Chemical and Biomolecular Engineering, Reader)
Prof. Sharon Gerecht (Chemical and Biomolecular Engineering)
Prof. D. Howard Fairbrother (Chemistry, Reader)
Prof. Kalina Hristova (Materials Science)

For the shorties ya'll with a special shout-out for K-Dizzle.

ACKNOWLEDGEMENTS

I would like to thank my family and friends for supporting me through the ups and downs of graduate school. My parents have always encouraged me to challenge myself and their support has been invaluable throughout my academic career. My mom especially saw the potential I had to do great things and made sure I was in an academic environment that fostered that. My dad has always been there to give me practical advice and if I had any odd ends that needed be tied together, he would always make time to help out. My brother Rod has also been a great role model with helpful advice and I have seen how his work ethic paid dividends in his academic and professional career. I am also very appreciative of the friends I have made in this department to share in the excitements as well the disappointments that are all too common to us all in working on tough research problems. Whenever I had issues with my work beyond my own expertise, it was easy to find a fellow grad student or professor with the answers for me.

I would like to thank my advisor, Dr. Bevan, who has been an incredible mentor and teacher for me during my Ph.D. He has instilled in me all of the skills needed to perform high-impact research in an ambitious and well-thought out manner. I am very grateful for the freedom I was given to work on challenging problems that interested me most while also keeping the big picture in focus for me. I'd also like to thank my lab mates, both past and present, who have been so helpful in teaching me new techniques and troubleshooting issues I have had. It was also great to work with undergraduate students on my work and I am glad to have had that experience as a research mentor for them. It has been a great lab to work in and I feel I am a better scientist having had this experience.

TABLE OF CONTENTS

LIST OF FIGURES

FIGURE Page

LIST OF TABLES

1. INTRODUCTION

1.1 Significance and Objective*

The interactions between proteins and carbohydrates play important roles in biology and medicine. Biological functions critical to bacteria,[1, 2] yeast,[3, 4, 5] and mammalian cells[6, 7, 8, 9, 10, 11] such as cell-cell signaling, migration, and regeneration are dependent on weak, specific interactions between proteins and carbohydrates. Protein-carbohydrate interactions have been used to engineer biomaterials able to recognize biomolecules and cell or tissue type in the body with high specificity for novel biosensing[12, 13, 14, 15] and targeted drug delivery[16, 17, 18, 19, 20, 21] applications. In order to better understand interactions at living biological interfaces (i.e. cells, tissues) and at biologically active material interfaces (i.e. biosensors, drug delivery particles), force measurement techniques and modeling efforts have allowed for in-depth analysis of biointerfacial systems. The binding affinity between proteins and carbohydrates are generally very weak further complicating their measurement. Highly sensitive, quantitative measurements along with comprehensive models are required to improve the fundamental understanding of behavior in biological systems mediated by specific protein-carbohydrate interactions and for further development and optimization of new biotechnologies that capitalize on these interactions.

Spectroscopic, scanning probe, and diffusing probe techniques have been developed to measure specific biomacromolecular interactions at an interface. Spectroscopic techniques such as dynamic light scattering, surface plasmon resonance, total internal

---

* This dissertation was written in the style of *Langmuir*.

reflection fluorescence microscopy, and ultraviolet-visible spectroscopy use changes in emission in bulk solution or at interfaces to detect specific binding of biomacromolecules and colloids. In scanning probe techniques such as atomic force microscopy, optical tweezers and surface force apparatus, an external force is applied either mechanically or optically and the displacement of the probe can be related to the strength of interaction at the interface mediated by specific biomacromolecular interactions. Diffusing probe techniques such as total internal reflection microscopy and diffusing colloidal probe microscopy use the mobility of colloidal particles due to Brownian motion to measure changes in colloid-surface and colloid-colloid interactions due to specific biomacromolecular interactions at their interface. The advantages and disadvantages of using each technique will be further discussed in the next section, but only from spectroscopic measurement techniques can important parameters on the biomacromolecular scale such as valency, cooperativity, and on/off-rate constants be resolved. However, scanning and diffusing probe techniques are able to measure interfacial forces due to specific binding of biomacromolecules which cannot be measured with spectroscopic techniques.

Modeling techniques can be used to evaluate parameters on both the biomacromolecular and interfacial scale to determine how specific biomacromolecular binding can influence interfacial interactions. Equilibrium and dynamic modeling techniques have been used to model colloidal and surface interactions mediated by biomacromolecular interactions at their interface. Equilibrium modeling such as analytical calculation and Monte Carlo (MC) simulation has been used to predict interfacial potentials of mean force between colloids and surfaces mediated by specific

biomacromolecular interactions. With the appropriate modeling approach, the effects of parameters on the biomacromolecular scale, accessible with spectroscopic methods, can be correlated to observations on the interfacial scale, from scanning and diffusing probe measurements, which allows for further interpretative and predictive power in these systems.

The goal of this dissertation is to develop complementary experimental and modeling techniques to interrogate and characterize colloidal and surface interactions mediated by weak, specific protein-carbohydrate interactions. By developing these techniques in tandem, the interplay of colloidal and surface interactions (e.g. gravity, van der Waals, electrostatics) and biomacromolecular interactions (e.g. non-specific steric interactions and specific binding between macromolecules) can be better interpreted. Diffusing colloidal probe microscopy will be used to measure interfacial interactions mediated by protein-carbohydrate interactions. With kT-scale sensitivity, diffusing colloidal probes are well suited for measurement of interfacial interactions mediated by weak, reversible protein-carbohydrate binding. To model the interactions in these systems, Monte Carlo simulations will be used to predict interfacial interactions mediated by specific biomacromolecular interactions and to better describe how interactions at the biomolecular scale give rise to the observed behavior on the interfacial scale. The two systems presented in this dissertation will demonstrate how to measure and model colloid-colloid interactions and colloid-cell surface interactions mediated by specific and nonspecific biomacromolecular interactions. The results from this work clearly show how diffusing colloidal probes can be used to study nonspecific and specific, reversible biomacromolecular interactions with experimental and simulation techniques to make

connections between phenomena on the colloidal scale to interactions on the biomolecular scale.

1.2 Background

Spectroscopic, scanning probe and diffusing probe techniques are the 3 major classes of measurement techniques used to study specific biomacromolecular interactions at interfaces. In this section, the general principles, systems studied, and limitations of each technique will be discussed. Equilibrium and dynamic modeling techniques can also be used as predictive and instructive tools in determining the impact of specific biomacromolecular interactions on net interfacial interactions. The basic concepts of each modeling technique and systems investigated will also be discussed in this section.

1.2.1 Spectroscopic Techniques

Dynamic light scattering (DLS) and ultraviolet-visible spectroscopy (UV-VIS) are spectroscopic techniques that can be used to measure changes in turbidity of a solution.[22, 23] Both techniques can be used measure specific binding between proteins and colloids where either the amount of adsorption in UV-VIS or scattering in DLS from the molecules and colloids in solution is dependent on their size. The role of solution chemistry, effective concentration, or particle surface chemistry on the binding and aggregation kinetics in these systems can be directly investigated with these techniques. With these measurements, the dynamics of colloidal aggregation mediated by specific protein-carbohydrate interactions systems have been studied.[24, 25, 26, 27] These techniques are limited only to bulk solution measurements and alternative methods are required to study binding and aggregation behavior of biomacromolecules and colloids at interfaces.

Surface plasmon resonance (SPR) and total internal reflection fluorescence microscopy (TIRFM) can be used to study the specific binding of biomacromolecules to a substrate.[28, 29] In SPR, excitation from a light source at a metal-liquid interface causes conversion of photons into surface plasmon waves. The light from the interface is total internally reflected with a reduced intensity due to the surface plasmon waves generated and angle of the reflected light is dependent on the refractive index of the surface. Fluctuations in intensity and angle of the reflected light can then be directly correlated to specific adsorption of biomacromolecules to the surface. Using this technique, SPR sensors can be created where biomacromolecular receptors are attached to a metallic surface to detect the adsorption of the complementary ligand from the bulk solution. This allows for direct and sensitive measurement of specific binding of biomacromolecules at interfaces to determine surface coverage, on/off-rates and binding affinity. SPR sensor arrays have been used extensively to measure weak, specific protein-protein and protein-carbohydrate interactions at interfaces.[30, 31, 32, 33, 34, 35]

TIRFM is also used to measure binding equilibrium and dynamics of biomacromolecules at interfaces. This technique allows fluorescently-tagged biomacromolecules at an interface to be detected with single molecule resolution. In TIRFM, a laser source directed towards a solid/liquid interface is totally internally reflected which then generates an evanescent wave. The evanescent wave will excite fluorescent molecules within 100 nm of the interface as its intensity exponentially decays as the distance from the surface increases. With illumination localized near the surface, background intensity from non-adsorbing fluorescent biomacromolecules is eliminated allowing for highly precise measurements of single binding events. This measurement

tool has been used to study a variety of systems including protein-protein, nanoparticle-cell, virus-cell, and cell-substrate interactions and dynamics at interfaces.[36, 37, 38, 39, 40]

Use of spectroscopic techniques like SPR and TIRFM are very appropriate for the study of binding of biomacromolecules at interfaces and can be useful in determination of many parameters relevant to biological systems and design of biomaterials. However, alternative methods are required to measure potentials of mean force between interfaces mediated by individual and ensembles of biomacromolecular complexes.

1.2.2 Scanning Probe Techniques

Scanning probe techniques such as AFM and OT rely upon the pertubation of a probe near an interface by externally applying force either with mechanical or optical methods to measure probe-interface interactions. AFM are able to probe interactions at surfaces with immobilized biomolecules or live cells by scanning a mechanical cantilever over the sample and the amount of deflection of the cantilever can be related to the force exerted on the surface.[41, 42, 43] This technique has been used for topographical imaging of supported lipid bilayers and live cell surfaces.[44, 45, 46, 47] In addition, the cantilever can be functionalized with biomacromolecules, biocolloids, or live cells and its interaction with a receptor-functionalized substrate allowing for direct measurement of net forces and binding lifetimes mediated by weak, specific biomacromolecular interactions with single molecule resolution.[48, 49, 50, 51, 52, 53, 54, 55, 56, 57]

OT an optics-based force measurement technique used to measure specific biomacromolecular interactions.[58, 59] In OT, a laser beam can be used to trap objects by inducing a dipole in the object that leads to an electrical gradient force that will drive an object to the point of focus of the laser beam. This technique has been used to trap and

manipulate colloidal particles, live cells, and biomacromolecules for measurements of pairwise interactions mediated by biomacromolecules and also has shown promise as a means to assemble biomaterials.[54, 60, 61, 62, 63] Forces mediated by biomacromolecular binding can be determined by applying the force required to move particles away from an interface until bonds are ruptured. Another strategy used is to weakly trap an object with a blinking OT that will hold a particle near an interface and still allow for Brownian fluctuations in distance from that interface to determine effective interaction potentials.

Scanning probe techniques allow for direct, quantitative measurement of biomacromolecular binding at interfaces with single molecule resolution. However all of these techniques require external forces to be applied which can pertube more weakly binding systems from equilibrium. Aside from blinking OT, weak, *kT*-scale interactions cannot be resolved due to the limited sensitivity of these methods.

1.2.3 Diffusing Probe Techniques

Diffusing probe techniques such as diffusing colloidal probe microscopy (DCPM) and total internal reflection microscopy (TIRM) can be used to measure colloidal interactions mediated by weak, specific biomacromolecules. DCPM was used most extensively in this work to study specific protein-carbohydrate interactions and particle-cell surface interactions. In DCPM, the 2D diffusion of colloidal particles and phase behavior of concentrated dispersions can be related to particle-surface and interparticle interactions, respectively. By tracking colloidal particles near interfaces in real-time, changes in diffusivity can be related to non-specific interactions and specific biomacromolecular surface interactions. Changes in association and dissociation between colloidal particles in 2D concentrated dispersions can also be used to measure net

colloidal interactions mediated by specific biomacromoleculare interactions. By allowing particles to freely diffuse without applying any external forces, the interactions of particles with an interface can be probed with *kT*-scale sensitivity. Many biomacromolecular systems such as DNA, protein-protein, and peptide interactions have been studied using this technique.[62, 64, 65, 66, 67, 68] It has also been demonstrated for patterned substrates how a surface can be characterized using DCPM[69] and these same principles have been applied extensively in *Chapter 8* of this work to study interactions of colloidal particles with the surface of cells.

In TIRM, colloidal particles diffusing near a surface can be tracked in 3D using evanescent wave tracking. By generating an evanescent wave near the surface, the intensity of evanescent wave scattering from a colloidal particle can be directly related to its height above the surface. By monitoring the particles fluctuation in height over time, a histogram of sampled heights can be constructed and particle-surface interaction potential can be determined. Using this technique, non-specific biomacromolecular, specific protein-carbohydrate and lipid bilayer interactions have been used to measure particle-surface interactions and binding lifetimes.[70, 71, 72] While this technique allows for sensitive measurement of height from a surface, it was not appropriate for either determination of particle-particle interactions where height information is not of crucial importance and in particle-cell interactions where scattering from cells in the evanescent wave would add noise to measured particle scattering intensity (i.e. particle-surface separation).

1.2.4. Modeling Techniques

Equilibrium models of colloidal and interfacial interactions mediated by specific

biomacromolecular binding have been developed for a number of biomacromolecular and biological systems.[73] These models allow for more in-depth characterization of force measurements in these systems where biomolecular parameters such as binding valency, binding affinity, or cooperativity can be directly input and monitored. Analytical and Monte Carlo (MC) simulation techniques have been used to study colloid-colloid, colloid-surface, cell-surface interactions mediated by specific biomacromolecular interactions.[74, 75, 76, 77, 78] Analytical model are most appropriate for systems with simple approximations for the interactions of colloids and biomacromolecules in the system. More complex systems such as those studied in this dissertation with multi-component mixtures of colloids and biomacromolecules are more easily modeled with MC simulation techniques where realistic interaction potentials can be input for each component in the systems and equilibrium quantities such as dissociation constants, binding isotherms, effective particle-particle and particle-surface interactions can be determined.

1.3 Summary and Dissertation Outline

This dissertation is organized as follows: *Chapter 2* describes the theoretical aspects of (i) colloidal and surface interactions, (ii) colloidal diffusion, (iii) colloidal aggregation, (iv) specific biomacromolecular interactions, and (v) Monte Carlo simulations. This section is intended to present the fundamental basis of the experimental and computational techniques used throughout this dissertation. *Chapter 3* presents the experimental and computational methods used in this dissertation. *Chapters 4-8* contain results related to this work. These chapters are or will be individually published. *Chapter 4* describes measurements of colloidal aggregation mediated by protein-carbohydrate

interactions. The results include measurements of specific protein surface adsorption to colloidal surfaces and aggregation kinetics in concentrated colloidal dispersions. *Chapter 5* describes equilibrium models of colloidal interactions mediated by specific biomacromolecular interactions. These results show how net effective colloidal potentials mediated by specific biomacromolecular interactions can be determined with biomacromolecular binding affinity as input. *Chapter* 6 describes a newly developed imaging and analysis technique to measure colloidal interactions with the surface of cells. These results include measurements of diffusion, binding lifetimes, and particle-cell surface potential energy profiles. *Chapter* 7 describes equilibrium modeling of particle-cell surface interactions mediated by specific interactions with membrane proteins. These results show net particle-surface interactions and selectivity of particle-surface binding can be manipulated as a function of ligand-receptor binding affinity, membrane protein surface density, and particle receptor density. *Chapter 8* summarizes the conclusions from this dissertation. Finally, *Chapter 9* presents some future work related to this dissertation.

2. THEORY

2.1 Colloidal and Surface Interactions

2.1.1 Net Potential Energy Interactions

For dispersions of colloidal particles interacting with a surface at physiological ionic strength, the overall net interactions of each particle, u_{net}, will be dependent on both the net particle-wall interaction potential, u_{pw}, and the net particle-particle interaction potential, u_{pp}, as given by,

$$u_{net}(h,r) = u_{pw}(h) + u_{pp}(r) \tag{2.1}$$

where h is the particle-wall surface separation and r is the particle-particle surface separation. The net particle-wall interaction potential is given by,

$$u_{pw}(h) = u^{pf}_{G}(h) + u_{V}^{pw}(h) + u_{S}^{pw}(h) + u_{B}^{pw}(h) \tag{2.2}$$

where the subscripts refer to gravitational (G), van der Waals (V), steric (S), and specific biomacromolecular interactions (B) and the superscripts refer to particle-field (pf) and particle-wall interactions (pw). The net particle-particle interaction potential is given by,

$$u_{pp}(r) = \sum_{i \neq j} u_{V}^{pp}(r_{i,j}) + u_{S}^{pp}(r_{i,j}) + u_{B}^{pp}(r_{i,j}) \tag{2.3}$$

where the subscripts refer to van der Waals (V), steric (S), and specific biomacromolecular interactions (B) and the superscripts refer to particle-particle interactions (pp).

2.1.2 Gravitational Interactions

The gravitational potential energy of each particle is dependent upon its height above the wall, h, and its buoyant mass, m, given by,

$$u_{G}^{pf}(h) = mgh = \frac{4}{3}\pi a^3(\rho_p - \rho_f)gh \tag{2.4}$$

where g is the acceleration due to gravity, a is the particle radius, ρ_p is the particle density, and ρ_f is the fluid density.

2.1.3 van der Waals Interactions

van der Waals attraction between two flat plates can be predicted by Lifshitz theory[79] with retardation and screening effects incorporated using the Derjaugin approximation to account for geometric effects[80] between a sphere and wall and two spheres as,

$$\begin{aligned} u_V^{pw}(h) &= (a/6)\int_h^\infty -A(l)/l^2\, dl \\ u_V^{pp}(r) &= (a/6)\int_r^\infty -A(l)/l^2\, dl \end{aligned} \tag{2.5}$$

where $A(l)$ is the Hamaker function given by,[81]

$$A(l) = -\frac{3}{2}kT\sum_{n=0}^{\infty}{}'\int_{r_n}^{\infty} x\left\{[1-\Delta_{13}\Delta_{23}e^{-x}]+\ln[1-\bar{\Delta}_{13}\bar{\Delta}_{23}e^{-x}]\right\}dx \tag{2.6}$$

The Δ terms include the frequency dielectric properties of the particle (1), wall/particle (2), and medium (3), and the remainder of the terms are discussed in detail in the literature.[81, 82] The prime ($'$) next to the summation indicates that the first term (n=0) is multiplied by ½(1+2κl)exp(-2κl) to account for screening of the zero-frequency contribution.

For simplicity, an inverse power law approximation can be used to model particle-wall and particle-particle van der Waals interactions[80] as,

$$\begin{aligned} u_v^{pw}(h) &= -aA_{pw}h^p \\ u_v^{pp}(r) &= -aA_{pp}r^p \end{aligned} \tag{2.7}$$

where A is an effective Hamaker constant appropriate over a short range (h < 15 nm) and p is a non-integer exponential. The constants, A and p, can be adjusted depending upon the dielectric properties and geometry (e.g., sphere-sphere, sphere-wall) of the interacting components.

2.1.4 Nonspecific Macromolecular Interactions

Nonspecific macromolecular interactions due to the compression of adsorbed and/or grafted brush layers on surfaces were modeled by Milner et. al.[83, 84, 85] and are given by,[86]

$$u_s^{pw}(h) = \left(\frac{5}{9}\right)\frac{u_0}{k_B T}\left[\frac{1}{h/h_0} + \left(\frac{h}{h_0}\right)^2 - \frac{\left(h/h_0\right)^5}{5}\right]$$
$$u_s^{pp}(r) = \left(\frac{5}{9}\right)\frac{u_0}{k_B T}\left[\frac{1}{r/r_0} + \left(\frac{r}{r_0}\right)^2 - \frac{\left(r/r_0\right)^5}{5}\right] \quad (2.8)$$

where, u_0 is the free energy per unit area of the uncompressed brush layer given by,[86]

$$u_0 = \frac{9}{10}\left(\frac{\pi^2}{12}\right)^{\frac{1}{3}} N\sigma^{\frac{5}{3}}\omega^{\frac{2}{3}}\nu^{\frac{1}{3}}k_B T \quad (2.9)$$

and h_0 and r_0 are the uncompressed layer thickness given by,[86]

$$h_0 = r_0 = \left(\frac{12}{\pi^2}\right)^{\frac{1}{3}} N\sigma^{\frac{1}{3}}\omega^{\frac{1}{3}}\nu^{\frac{-1}{3}} \quad (2.10)$$

In Eqs. (2.9) and (2.10), N is the number of Kuhn segments in the chain, σ is surface coverage density, ω is an excluded volume parameter, and ν is a function of the chain

radius. The Derjaguin approximation can then be used to calculate the overall steric particle-wall and particle-particle interactions, $u_S^{pw}(h)$ and $u_S^{pp}(r)$, respectively, as,[86]

$$u_S^{pw}(h) = 2\pi a\left[\int_h^\infty \left(u_s^{pw}(h) - u_s^{pw}(h_0)\right)dh\right]$$
$$u_S^{pp}(r) = 2\pi a\left[\int_r^\infty \left(u_s^{pp}(r) - u_s^{pp}(r_0)\right)dr\right] \quad (2.11)$$

where changes in the interaction due to geometry are accounted for. The resulting repulsive steric interactions can be more simply modeled with a short range exponential given by,

$$u_S^{pw}(h) = \Gamma\exp(-\kappa h)$$
$$u_S^{pp}(r) = \Gamma\exp(-\kappa r) \quad (2.12)$$

where Γ and κ are determined by the structure of the macromolecular layers at the interface.

2.1.5 Specific Biomacromolecular Bridging Interactions

For polysaccharide-functionalized colloidal particles in the presence of adsorbing proteins mediated by specific protein-carbohydrate interactions, attractive colloidal interactions can be induced between particles via simultaneous binding between neighboring particles. Net attractive particle-surface interactions can also be induced by specific protein-carbohydrate interactions between polysaccharide-functionalized colloids and surface-immobilzed protein receptors (i.e., expressed on cell membranes). To model particle-particle or particle-surface interactions mediated by ensembles of weak, reversible protein-polysaccharide bridges, an isotropic harmonic well attractive potential can be added with the form,

$$u_B^{pw}(h) = u_{\min}(\frac{h-h_{\min}}{h_{\min}})^2$$
$$u_B^{pp}(r) = u_{\min}(\frac{r-r_{\min}}{r_{\min}})^2 \quad (2.13)$$

where $u_{\min}$ is the depth of the harmonic well and $h_{\min}$ and $r_{\min}$ are the positions of the harmonic potential well minimum. The resulting net particle-particle or particle-surface interaction potential, including van der Waals, steric, and specific biomacromolecular bridging interactions, can be modeled with a Morse harmonic potential given as,[87]

$$u_{pw}(h) = u_G^{pf}(h) + u_{\min}[1-\exp(-k(h-h_{\min})]^2 - u_{\min}$$
$$u_{pp}(r) = u_{\min}[1-\exp(-k(r-r_{\min})]^2 - u_{\min} \quad (2.14)$$

where k is the decay length that controls the range of the harmonic well.

2.2 Colloidal Diffusion

2.2.1 Particle-Wall Hydrodynamics

A colloidal particle diffusing near a surface will experience hydrodynamic interactions that will hinder the lateral motion of the particle from its predicted Stokes-Einstein diffusivity, where $D_o = kT/(6\pi\mu a)$, which depends on the viscosity of the medium, μ. These effects can be accounted for with a hydrodynamic correction factor[88] as,

$$D_{\|}(h) = D_o f_{\|}(h) \quad (2.15)$$

where $f_{\|}$ is a rational fit to the exact solution given as, [89]

$$f_{\|}(h) = \frac{1220\omega(h)^2 + 5654\omega(h) + 100}{12420\omega(h)^2 + 12233\omega(h) + 431} \quad (2.16)$$

where $\omega(h) = h/(a+\delta_b)$ and δ_b is the polymer brush layer thickness. The distribution of heights sampled by the particle, $p(h)$, can be related to the net particle-wall interaction potential with Boltzmann's equation as,[90, 91]

$$p(h) = \exp(\frac{-u_{pw}(h)}{kT}) \tag{2.17}$$

and predictions of the average lateral diffusion coefficient, $\langle D_{||} \rangle$, can be made using the distribution of heights sampled given by,[92]

$$\left\langle D_{\|} \right\rangle = \frac{\int D_{\|}(h)\, p(h)\, dh}{\int p(h)\, dh} \tag{2.18}$$

2.2.2 Particle-Particle Hydrodynamics

In dispersions of colloidal particles, particle-particle hydrodynamic interactions will hinder their diffusion and the diffusion coefficient can be predicted for particles in concentrated solutions with the correction factor, f_{pp}, given by,[93]

$$D_{\|,pp}(r) = f_{pp}(r) D_o \tag{2.19}$$

where $f_{pp}(r)$ is a rational fit to exact solutions, given as[94]

$$f_{pp}(r) = \frac{54\gamma(r)^3 + 71\gamma(r)^2 + 8\gamma(r)}{54\gamma(r)^3 + 154(r)^2 + 60\gamma(r) + 4} \tag{2.20}$$

and $\gamma(r) = r/(a+\delta_b)$.

2.3 Colloidal Aggregation

2.3.1 Aggregation Kinetics

The kinetics of aggregating colloidal suspensions can be characterized by the change in concentration of singlets, doublets, and higher order aggregates over time. A

simple mass balance can be used to describe the rate of change in singlet concentration as,[95]

$$\frac{d\phi_1}{dt} = -2k_{11}\phi_1^2 - \sum_{i=2}^{N} k_{1i}\phi_1\phi_i \tag{2.21}$$

where ϕ_1 is the concentration of aggregates consisting of i particles at time t and k_{1i} is the rate constant for aggregation of single particles with aggregates of size i. For an initially stable dispersion, formation of doublets from single particles will largely determine the rate of singlet disappearance at the early stages of aggregation and this allows the singlet disappearance rate to be further reduced to,

$$\frac{d\phi_1}{dt} = -2k_{11}\phi_1^2 \tag{2.22}$$

2.3.2 Diffusion-Limited Aggregation

Diffusion-limited aggregation in colloidal suspensions occurs when colloidal particles irreversibly adhere at contact, and the rate of aggregation is directly proportional to the colloidal diffusion rate of the colloids. In 1916, Smoluchowski calculated the aggregation rate constant of colloidal particles diffusing in 3D as,[96]

$$k_{11,Smol} = 4\pi D_o \tag{2.23}$$

A Smoluchowski aggregation rate constant was calculated for particles diffusing in 2D by Hardt as,[97]

$$k_{11,Hardt} = \frac{2\pi D_o}{\ln[\frac{(\pi\phi_{1,o})^{-1/2}}{r_{agg}}]} \tag{2.24}$$

where $\phi_{1,o}$ is the initial singlet concentration and r_{agg} is the particle encounter radius.

2.3.3 Aggregation into the Secondary Potential Energy Minimum

In reversibly aggregating colloidal suspensions, particle-particle collisions will not always result in the formation of an aggregate. The primary net potential energy minimum has an infinite attractive well depth and is inaccessible in these systems due to the solution and/or surface chemistry (i.e., long-range electrostatic or short-ranged steric interactions). In such colloidal suspensions, aggregation occurs within *or* over separation distances where a secondary attractive well with finite depth dominates the net colloidal energy potential. The probability that a collision will result in the formation of an aggregate is dependent upon the depth of the secondary minimum. The aggregation rate in these systems can be compared to that of diffusion-limited systems using a Fuchs stability ratio, defined as,[98]

$$W = \frac{k_{Smol/Hardt}}{k_{\exp}} \tag{2.25}$$

where $k_{\exp}$ is the aggregation rate constant measured experimentally at early times. The stability ratio can then be related to net particle-particle interactions, defined in Eq. (2.14), with a modified Fuchs integral, as given by, [99]

$$W = \varepsilon^{-1}(2a+\delta_b)D_o \int_{r_{\min}}^{\infty} \frac{\exp(u_{pp}(r)/kT)}{(r+2a+\delta_b)^2 \left\langle D_{\parallel} \right\rangle (r)} dr \tag{2.26}$$

where ε is the probability a particle has the thermal energy required to escape the secondary minimum, defined as,

$$\varepsilon = 1 - \exp(u_{\min}/kT) \tag{2.27}$$

where it is assumed that the particles have a Boltzmann distribution of thermal energies.

2.4 Specific Biomacromolecular Interactions

2.4.1 Free Energy of Specific Biomacromolecular Binding

Receptor-ligand interactions can be modeled as entropic springs with a monovalent harmonic well potential, U_{RL}. This is an estimate of the free energy between two interacting biomacromolecules averaged over all of the angular and conformational dependencies of their complex. U_{RL} is a function of receptor-ligand separation, r, with the form,

$$\begin{aligned} U_{RL}(r) &= \frac{1}{2}k_s r^2 - u_{\min} \qquad \text{if } 0 < r < \delta \\ U_{RL}(r) &= 0 \qquad\qquad\qquad\quad \text{if } r > \delta \end{aligned} \tag{2.28}$$

that has an interaction range, δ, that can be calculated as,

$$\delta = \sqrt{\frac{2u_{\min}}{k_s}} \tag{2.29}$$

which is dependent on the harmonic well depth, $u_{\min}$, and spring constant, k_{s}. With this potential, neither the ligands or receptors have an effective size with $u_{\min}$ at zero receptor-ligand separation.

In order to introduce an effective size to the ligands, they can be modeled as hard spheres with an isotropic (i.e., non-orientation dependent) harmonic well at their surface. For the receptor-ligand nanosphere potential, U_{RLN}, we use the form,

$$\begin{aligned} U_{RLN}(r) &= \infty \qquad\qquad\qquad\quad \text{if } r < a_{lig} \\ U_{RLN}(r) &= \frac{1}{2}k_s (r - a_{lig})^2 - U_{\min} \qquad \text{if } a_{lig} < r < a_{lig} + \delta \\ U_{RLN}(r) &= 0 \qquad\qquad\qquad\quad \text{if } r > a_{lig} + \delta \end{aligned} \tag{2.30}$$

Ligands with this effective size will experience infinite repulsion at ligand-receptor contact that then decays into an attractive harmonic well.

2.4.2 Bulk Dissociation Constant

The dissociation constant, K_d, is a measure of the binding affinity between biomacromolecules in solution, as given by,

$$K_d = \frac{[RL]}{[R][L]} \tag{2.31}$$

where [R] and [L] are the concentrations of free receptors and ligands respectively and [RL] is the concentration of receptor-ligand complexes. An analytical expression for the dissociation constant of a harmonic well potential can be determined using the Bjerrum approach for calculating absolute macromolecular binding free energy developed by Luo and Sharp. [100] For a simple harmonic well potential, as in Eq. (2.28), K_d can be calculated using the expression, [100]

$$K_d = [(2\pi)^{3/2}(\frac{k_s}{kT})^{-3/2} e^{-u_{\min}/kT}]^{-1} \tag{2.32}$$

which exponentially decays with increasing well depth, and in short, correlates the Brownian fluctuations in the position of the biomacromolecules in their bound state to the biomacromolecules in their unbound state.

In order to make dissociation constant predictions for ligands with an effective size, the second virial coefficient, B_2, is calculated for the ligand nanospheres to estimate their effective interaction strength. The second virial coefficient for a ligand nanosphere, $B_{2,\mathrm{RLN}}$, is calculated with the following expression,

$$B_{2,RLN} = 4V + 12\int_{a_{lig}}^{a_{lig}+\delta} r^2(1-e^{U_{RLN}(r)/kT})dr \tag{2.33}$$

The first term is the hard sphere component of $B_{2,\mathrm{RLN}}$ that is simply four times its volume, V. The second term accounts for the harmonic well tail component of $B_{2,\mathrm{RLN}}$ and this is

calculated using an expression which can be applied to any arbitrary potential to determine B_2.[101] An equivalent harmonic well potential is then found by determining a harmonic well with the same B_2 as the ligand nanosphere potential. The second virial coefficient of a harmonic well potential, $B_{2,\mathrm{RL}}$, is calculated as,

$$B_{2,RL} = 12\int_0^{\delta} r^2 (1 - e^{(\frac{-U_{RL}(r)}{kT})}) dr \tag{2.34}$$

using the same expression to determine B_2 for any arbitrary potential. To find an equivalent harmonic well potential, $u_{\min}$ in Eq. (2.28) for U_{RL} is adjusted at constant k_{s} until $B_{2,\mathrm{RL}}$ is equal to $B_{2,\mathrm{RLN}}$ of the ligand nanosphere potential. These two potentials are then considered equivalent and the K_{d} of the harmonic well calculated from Eq. (2.32) is assigned to the ligand nanosphere.

2.4.3 Biospecific Adsorption at Interfaces

Adsorption equilibria of ligands with monovalent interactions and receptors at an interface can be predicted with the Langmuir adsorption model as given by,

$$\theta = \frac{K_d^{-1} C}{1 + K_d^{-1} C} \tag{2.35}$$

which determines the fraction of occupied receptors, θ, as a function of bulk ligand concentration, C. The adsorption coefficient for this system is the inverse of K_{d} (i.e., the association constant, K_{a}).

2.5 Monte Carlo Simulations of Colloidal and Biomacromolecular Systems

2.5.1 Metropolis Monte Carlo Method

In order to develop models of the colloidal interactions in the presence biomacromolecules and biological interfaces, it is important to consider parameters traditionally studied in colloidal systems as well as incorporate realistic, biologically

relevant parameters to determine their impact on experimentally observed ensemble average quantities, such as colloid-colloid or colloid-surface separation. Using a statistical mechanics-based formalism, an ensemble average quantity, $\langle A \rangle$, can be directly computed with the expression,[102]

$$\langle A \rangle = \frac{\int d\mathbf{p}\, d\mathbf{r} A(\mathbf{p},\mathbf{r}) \exp\left[-\mathcal{H}(\mathbf{p},\mathbf{r})/kT\right]}{\int d\mathbf{p}\, d\mathbf{r} \exp\left[-\mathcal{H}(\mathbf{p},\mathbf{r})/kT\right]} \tag{2.36}$$

where **p** and **r** refer to the particle momenta and position, respectively, and $\mathcal{H}$ is the Hamiltonian function of **p** and **r** that gives the total energy of the system. Since kinetic energy contributions can be ignored in the systems in this work, the expression further simplifies to,

$$\langle A \rangle = \frac{\int d\mathbf{r} A(\mathbf{r}) \exp\left[-u_{net}(\mathbf{r})/kT\right]}{\int d\mathbf{r} \exp\left[-u_{net}(\mathbf{r})/kT\right]} \tag{2.37}$$

where u_{net} is the net potential energy of the system only dependent on particle positions**.** Even with this simplification, direct computation of this quantity is complicated typically by system size and for the systems of interest in this work, bi- and tri-component mixtures of atoms (i.e., colloids, proteins, ligands) further complicate their calculation. Using traditional integration methods, the computation time required would prove prohibitive in analyzing these systems.

In order to avoid such computationally expensive calculations, the Monte Carlo method has been developed where the function u_{net} can be evaluated for random configurations of atoms in the system over intervals of interest. However by performing this calculation randomly over this interval, computation time can be spent in configuration space with little impact on the ensemble average quantity. To interrogate

the most statistically relevant configurations, the Metropolis scheme of Monte Carlo Sampling was introduced where the random configurations chosen to include in the integral calculation are weighted by the Boltzmann factor, $\exp\left[-u_{net}(\mathbf{r})/kT\right]$. With this scheme, attempts are made to change to a random particle configuration, **m**, from an initial configuration, **n**, and these attempts are only accepted with the following condition is met:

$$x_r < \exp[-(u_{net}(\mathbf{m}) - u_{net}(\mathbf{n}))/kT] \tag{2.38}$$

where x_r is a randomly generated variable from [0,1]. With this criterion, detailed balance is maintained as systems will not move from their equilibrium state to a state of higher energy.

2.5.2 Cluster Moves

Typically in Monte Carlo simulations, attempts are made to translate each atom in the system independently and the move is accepted or rejected dependent on the resulting free energy change in the system. However, in systems with strongly bound particles (e.g., aggregated or covalently bound particles) or mixtures of binary, non-uniform colloidal spheres (e.g., colloid-protein mixtures), independent MC translational moves are seldom accepted and efficient sampling of random colloidal configurations becomes limited. For these more complex systems, cluster move algorithms have been developed that allow for simultaneous translation and/or rotation of *n* associated atoms, where the same Metropolis criterion from Eq. (2.38) is applied for the newly generated configuration ensuring detailed balance is maintained.[102, 103, 104] The execution of these moves varies dependent on the system being modeled, but details will be given in

Chapter 3 of this dissertation as to how these moves are performed for the colloidal systems modeled in this work.

2.5.3 Free Energy Estimation

It is also desirable to estimate changes in free energy, W, based on an order parameter, Ω, that shows dependency on the configurations sampled in the system. Fortunately, these can also be obtained from Metropolis Monte Carlo by measuring the distribution of Ω sampled in your system, $\rho(\Omega)$, at equilibrium. The change in free energy can then be computed using a Boltzmann distribution analysis, as given by,[22]

$$\frac{W(\Omega)-W(\Omega_o)}{kT} = -\ln(\frac{\rho(\Omega)}{\rho(\Omega_o)}) \tag{2.39}$$

where Ω_o is the order parameter at a reference state. This is a simple, straightforward method to determine changes in free energy near the global minimum but is insufficient in determining changes at values of the order parameter far from this point due to limited sampling.

2.5.4 Umbrella Sampling

In order to sample non-equilibirum states far from the free energy minimum of a given order parameter, a technique known as Umbrella Sampling was developed by Torrie and Valleau.[105] Umbrella Sampling allows the system to sample non-equilibrium states by applying a biasing potential, $u_b(\Omega)$ that restricts configurations to values of Ω and $\mathbf{r}$ away from equilibrium. The free energy of the system with the biasing potential, $W_b(\Omega)$ can also be determined using a Boltzmann distribution analysis as shown in Eq. (2.39) and the unbiased potential, $W(\Omega)$, can be calculated as,

$$\frac{W(\Omega)}{kT} = [W_b(\Omega) - u_b(\Omega)] / kT + C_b \tag{2.40}$$

where C_b is an unknown additive constant that can be later determined from the reference state.

3. METHODS

3.1 Functionalization of Colloids and Surfaces

3.1.1 Physisorption of Macromolecules

All colloidal particles and surfaces used in this work were composed of silicon dioxide (SiO_2). Since protein and cell solutions are at physiological ionic strength (150 mM NaCl), a steric polymer or protein surface layer was necessary to provide interparticle stability and to prevent adsorption of SiO_2 colloids to silica substrates. In order to physically adsorb macromolecules to colloids and surface, they were first modified with a hydrophobic coating to allow for self-assembly of dense polymer and protein layers. Procedures were developed for hydrophobic modification of both silica colloids and surfaces.

Glass microscope slides (Fisher Scientific, Pittsburgh, PA) and cover slips (Corning Life Science, Tewskbury, MA) were hydrophobically modified by spin coating polystyrene onto their surface.[106] The substrates were first cleaned by sonication in acetone for 30 minutes then placed in Nochromix (Godax Laboratories, Cabin John, MD) overnight. Next, they were rinsed 20x times with DI water then sonicated in 0.1 M KOH for 30 minutes. They were again rinsed 20x times with DI water and dried with nitrogen. A thin film of polystyrene is made on the glass substrate using a spin coater (Laurell Technologies Corp., North Wales, PA) by placing a 3% (w/w) solution of polystyrene in toluene onto the glass substrate and spinning until the drop spreads and deposits onto the surface. The amount of polystyrene solution, rotation speed, and duration were optimized for each size of the substrate. The specific parameters used are available in the Materials and Methods sections of *Chapters 4* and *6*.

Batch cells are then created on the substrate to physisorb polymers and proteins to their surface. To create a batch cell, the slides were allowed to dry for 30 minutes before adhering a 1 mm ID Viton O-ring (McMaster Carr, Inc., Robbinsville, NJ) onto the slide with vacuum grease. Twenty-five μL of 1000 PPM (1 mg/mL) solution of F108-Pluronic (PEG-PPO-PEG triblock copolymer, BASF, Wyandotte, MI) or bovine serum albumin (BSA, Sigma, St. Louis, MO) are added to the batch cell and allowed to adsorb for 4 hours. The hydrophobic PPO chains in F108-Pluronic and the hydrophobic domains of BSA allow these macromolecules to form monolayers on the polystyrene-coated substrates. Excess, un-adsorbed F108-pluronic or BSA was removed by rinsing with a pipette 5 times with phosphate buffered saline (PBS, Invitrogen, Carlsbad, CA) before each experiment.

Silica particles were hydrophobically modified with 1-octadecanol with a procedure adapted from literature.[107] A solution of as purchased SiO_2 colloids (Bangs Laboratories, Fishers, IN) was made in deionized water. The particle solution was centrifuged and re-suspended in DI water 5 times followed by centrifugation and re-suspension 5 times in 200 proof ethanol to remove all water from the particle solution. The particle solution was then added to a 0.1 mg/mL solution of 1-octadecanol in 200 proof ethanol in a 50 mL round bottom flask. The solution is then mixed and heated at 50ºC under a nitrogen blanket (reactant mixture is flammable) until the 1-octadecanol is dissolved. Once the ethanol has evaporated, the nitrogen stream is removed and the flask is heated to 200ºC and held at this temperature for 3 hours to fixate the 1-octadecanol to the surface of the particles. Once the reaction has completed, the vessel is cooled to room temperature and the reactant mixture is recovered in chloroform to dissolve any free 1-

octadecanol from solution. The particle solution is then centrifuged and re-dispersed in chloroform 5 times followed by centrifugation and re-dispersion in 200 proof ethanol to remove all chloroform. The particles are then stored at -5ºC in 200 proof ethanol. To adsorb macromolecules to the 1-octadecanol coated silica particles, the particles are dispersed in 1 mg/mL F108-pluronic or BSA solutions for at least 4 hours. Excess F108-pluronic or BSA is removed by centrifugation and re-suspension in DI water 5 times.

3.1.2 Chemisorption of Macromolecules

Colloidal particles were functionalized with polysaccharide layers with protocols adapted from literature[108, 109] to provide steric stability and allow for study of specific protein-carbohydrate interactions. However, the polysaccharides in this work are relatively hydrophilic polymers and will not physisorb to a hydrophobic surface. Silane chemistry was used to introduce functional groups on the surface of silica particles to chemically conjugate polysaccharides to their surface. This same chemistry was also used on silica substrates to introduce polysaccharide layers to provide both steric stability for colloidal particles and adherent substrate appropriate for *in vitro* cell culture to be discussed in the next section.

To functionalize colloidal silica with polysaccharides, either an epoxy or amino-silane linker was used to chemically graft polysaccharides to the surface dependent on the polysaccharide used. Before functionalization, the silica particles were washed using a micro-centrifuge (MiniSpin-plus, Eppendorf, Hamburg, Germany) by centrifugation and re-dispersion in fresh DI water. This washing step was repeated 5 times. The particles were then dispersed in dry ethanol and washed an additional 5 times in dry ethanol. To modify particles with an epoxy silane linker, the particles were dispersed in a 0.1% (v/v)

3-glycidoxypropyltrimethoxysilane (GPTMS, Sigma, St. Louis, MO) solution in dry ethanol for 1 hour. To modify particles with an amino-silane linker, the particles were dispersed in a 2% (w/w) (3-aminopropyl)triethoxysilane (APTES, Sigma, St. Louis, MO) solution in dry ethanol for 24 hours. The silane linker-modified silica colloids were then washed 5 times in dry ethanol and 5 times in DI water. To conjugate dextran (500 kDa, Sigma, St. Louis, MO) onto silica particles, epoxy-silane (GPTMS) modified colloids were dispersed in 30% (w/w) aqueous solution of polysaccharide and gently mixed with a magnetic stir bar for 24 hours. To conjugate hyaluronic acid (HA, 1 MDa, R&D Systems, Minneapolis, MN) to silica particles, amino-silane (APTES) modified colloids were dispersed in a 3 mg/mL HA solution for at least 20 hours. The polysaccharide-modified particles are then centrifuged at 10,000 RPM for 10 minutes and re-dispersed in fresh DI water. They are then washed with DI water an additional 5 times. Pluronic-F108 is then physisorbed onto the polysaccharide-modified particles by dispersing the particles in 1000 ppm (1 mg/mL) aqueous solution of F108-Pluronic overnight. The F108 coating step is to ensure the particles are fully coated with a polymer brush to improve colloidal stability. The particles are then rinsed 5 times in DI water and dispersed in PBS.

3.1.3 Surfaces with Adherent Cells

To study colloidal interactions with the surface of cells, live cells were cultured onto cover slips for imaging with synthetic polymer, protein, and polysaccharide-decorated colloids. It was important to design the surface to both provide stability for the colloidal particles and allow for cells to adhere and spread onto the surface. To accomplish this, cover slips were coated with HA--which is found in the extracellular matrix--to facilitate cell adhesion through specific protein-carbohydrate interactions,

which allows for adjustment of polymer brush thickness by varying HA molecular weight. The amino silane linker, APTES, was again used to functionalize silica cover slips with HA and once functionalized, these surfaces were seeded with cells.

Glass cover slips (18 mm x 18 mm) were first cleaned as explained previously with sonication in acetone for 30 minutes, overnight soak in Nochromix, and a 30-minute KOH treatment. Once cleaned and dry, the cover slips were then placed in 2% (w/w) APTES solution in ethanol for 24 hours for amino-silane functionalization. To rinse excess APTES away from the surface, slides are first sonicated in ethanol for 30 minutes, followed by sonication in water for 30 minutes, and then dried with nitrogen. Once dry, the APTES-coated coverslips were placed into dishes on top of 1 mm ID viton O-rings. A 3 mg/mL HA (100 kDa, Lifecore Biomedical, Chaska, MN) solution was made in DI water filtered with a Anotop 0.02 μm syringe filter (Whatman. Pittsburgh, PA) to ensure sterility. 500 μL of the sterilized HA solution was placed on each APTES-coated cover slip and kept covered in a dish coated with moist towels to chemisorb for at least 20 hours.

Once the HA chemisorption step was completed, the HA-coated cover slips were placed under UV irradiation for 30 minutes to again ensure sterility and placed into a 6-well plate (Corning Life Science, Tewskbury, MA) in PBS. MDA-MB-231 epithelial breast cancer cells (MDA231, National Cancer Institute Physical Sciences-Oncology Center (NCI-PSOC), National Institues of Health, Bethesda, MD) were maintained in Dulbecco's Modified Eagle Medium (DMEM, Invitrogen, Grand Island, NY) containing 10% (v/v) fetal bovine serum (FBS, Atlanta Biologicals, Flowery Branch, GA). MDA231 cells were seeded onto HA-coated coverslips at a 1:4 ratio (~50,000 cells/cm^2) in

complete media (10% FBS in DMEM). The cells are then allowed to adhere and spread onto the HA-coated coverslips overnight before each experiment.

3.2 Microscopy Techniques

3.2.1 Bright Field Microscopy

Bright field microscopy (BFM) is one of the simplest and most widely used microscopy techniques for imaging colloidal particles and biological samples. In this technique, transmitted light is used to illuminate the sample and the objects in the sample will absorb this light creating contrast with the background. For colloidal silica, the particles will appear brighter than the background with the highest intensity at their center allowing them to be identified with image analysis algorithms. This imaging technique was used most extensively in *Chapter 4*. For those experiments, an inverted optical microscope (Axioplan 2, Carl Zeiss, Obercheken, Germany) with a 63x objective (LD-Plan Neofluar, NA = 0.75, Carl Zeiss) was used to capture images in real time with a 12-bit CCD camera (ORCA-ER, Hamamatsu, Hamamatsu City, Japan). However, one common issue for biological samples is the lack of contrast with the background image and in the next section, the use of dark field microscopy will be discussed to overcome this limitation.

3.2.2 Dark Field Microscopy

Dark field microscopy (DFM) is a technique used where scattering from the sample is collected resulting in a dark background where no objects are present. As is illustrated in Figure 3.1, a dark field condenser blocks direct illumination from a transmitted light source and only allows light with wide incident angles to illuminate the sample which is scattered by objects in the field of view . This allows for high contrast

imaging of colloidal particles, particularly metallic particles due to local surface plasmon enhanced scattering, and also in biological samples where the cytoskeleton and other internal components scatter under dark field illumination. This technique is limited to samples that scatter brightly under dark field illumination which can be an issue for non-metallic particles such as polystyrene dependent on their size. DFM was performed using an inverted optical microscope (Axioplan 2, Carl Zeiss, Obercheken, Germany) with a dark field condenser (dry, 0.8/0.95 NA, Carl Zeiss) and a 40x objective (LD-Plan Neofluar, NA = 0.75, Carl Zeiss).

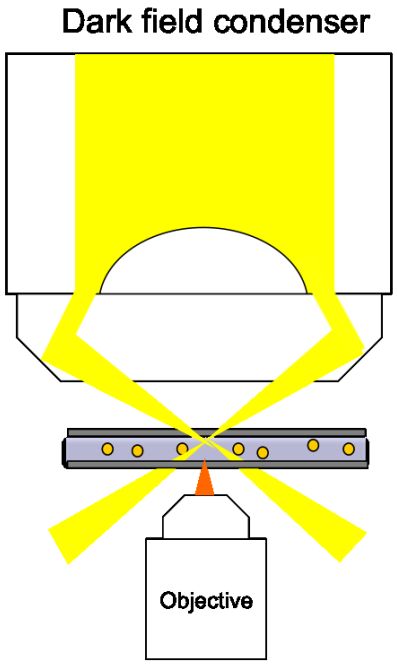

Fig 3.1. Schematic of Dark Field Microscopy. Adapted from literature.[110]

3.2.2 Laser Scanning Confocal Microscopy

Laser scanning confocal microscopy (LSCM) is a technique used for high resolution 2D and 3D imaging of samples with either fluorescence or reflectance. A laser

source illuminates the sample and any out-of- plane objects can be blocked from the field of view by adjusting the size of a pinhole that allows the return of reflected or emitted light. This enhances the resolution possible compared to conventional microscopy techniques while sacrificing the total measurable intensity that can de detected. This limitation can be overcome with the use of photodetectors with increased sensitivity. This imaging technique was used in *Chapter 4* to image both colloids and biomacromolecules with a combination of reflectance and fluorescence imaging, respectively. LSCM imaging was performed using an inverted confocal microscope (Axio Observer.Z1, Carl Zeiss) with a mounted scanning laser (LSM 5 Pascal Scanner, Carl Zeiss) and an oil-immersion 63x objective (Apochromat, NA = 1.45, Carl Zeiss). A 102 μm x 102 μm area was scanned in reflection and fluorescence mode with a 488 nm 500 mW Ar laser as an excitation source.

3.3 Image Analysis

3.3.1 Tracking Colloidal Particles

In this work, colloidal particles were identified and tracked using bright and dark field microscopy. Image analysis routines written in both FORTRAN[111] and MATLAB[112] have been developed to identify centers and construct trajectories of colloidal particles from experimental images. In either BFM or DFM, particles could be distinguished from the background based on their increased intensity and the particle center can be found with pixel-level resolution as the maximum intensity due to their spherical shape. Sub-pixel accuracy can be achieved by refining the particle centroid with an intensity-based weighting function that considers pixels within a given radius of the maximum intensity centroid (x_m, y_m) given by,[112]

$$\begin{pmatrix} \delta_x \\ \delta_y \end{pmatrix} = \frac{1}{m_o} \sum_{i^2+j^2 \le w^2} \begin{pmatrix} i \\ j \end{pmatrix} A(x_m + i, y_m + j) \tag{3.1}$$

where $m_o = \sum_{i^2+j^2 \le w^2} A(x_m + i, y_m + j)$ is the integrated intensity of the sphere's image and the refined particle coordinates are determined as $(x_r, y_r) = (x_m + \delta_x, y_m + \delta_y)$. Particle trajectories are constructed by linking particle centers based on their displacement from frame to frame. In order to correctly link particle centers, the particle diffusion coefficient, D, and the frame rate of images captured, f_r, can be used to estimate a characteristic diffusion length scale, $r_D = \sqrt{\frac{Df_r}{\pi}}$, and particle trajectories are chosen such that their displacement is less than or equal to r_D.

When simultaneously tracking colloidal particles and cells in dark field microscopy experiments, there is the added difficulty of discriminating between real particle centers from colloidal dark field scattering and erroneous particle centers found from dark field scattering from intracellular components (i.e. cytoskeleton, organelles, vesicles). Since the intensity of scattering from silica particles and intracellular components is relatively similar, differentiating between particle and cell scattering based on intensity alone is not possible. To differentiate between colloids and cells, we use the added condition that particles that are tracked and included for analysis must have a trajectory that begins outside of defined cell boundaries. In Fig. 3.2, the results of this added criteria are shown where Fig. 3.2A shows the initial centers found based on intensity. In Fig. 3.2B, the centers are shown after analyzing each particle trajectory and deleting trajectories that start within the cell boundaries (marked with white lines). While

this will eliminate real particle centers that start within the boundaries, this ensures that all trajectories included for analysis are colloids and not scattering points in the cell.

3.3.2 Tracking Live Cells

Using DFM, colloidal particles and live cells were imaged simultaneously to study particle-cell interactions. To discriminate between colloidal particles and cells, MATLAB routines were developed to identify the positions of cell boundaries over time. Using functions from the MATLAB Image Processing Toolbox™, the following steps

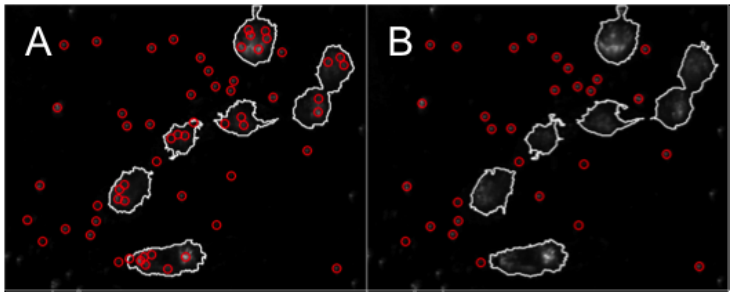

Fig 3.2. (A) Particle centers (red circles) found based on brightest intensities. (B) True particle centers with trajectories starting outside of the cell boundaries (white lines).

were taken to identify and track cells in each image which are illustrated in Figure 3.3. First, the entire is image is thresholded to obtain a black and white image, shown in Figure 3.3A, that will show both cells and colloidal particles. Silica particles cannot be eliminated based on intensity alone as their scattering under dark field illumination is on the order of that from live cells. Cells and particles were distinguished using a size criteria as cells were typically 10-20 times larger than the silica particles studied in this work. Objects from the thresholded image with areas greater than 500 μm^2 were labeled as cells and boundary points were determined for each cell in the frame drawn in white

Figure 3.3B. The coordinates of these boundaries were then used to determine the position of colloidal particles with respect to the surface of the cell in real time.

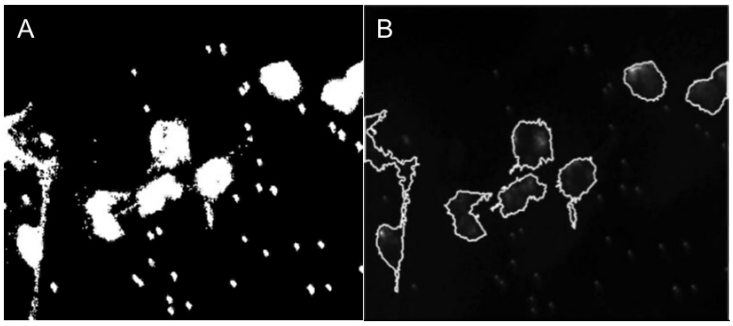

Fig 3.3. (A) Thresholded image from dark field microscopy of silica particles and live cells. (B) Cell boundaries (drawn in white) determined using minimum area cutoff.

3.3.3 Colloidal Particle to Cell Surface Distance

In order to measure equilibrium particle-cell interactions, particle-cell surface radial distribution functions were constructed which could be interpreted with a Boltzmann probability analysis. With cell surface boundary coordinates and particle

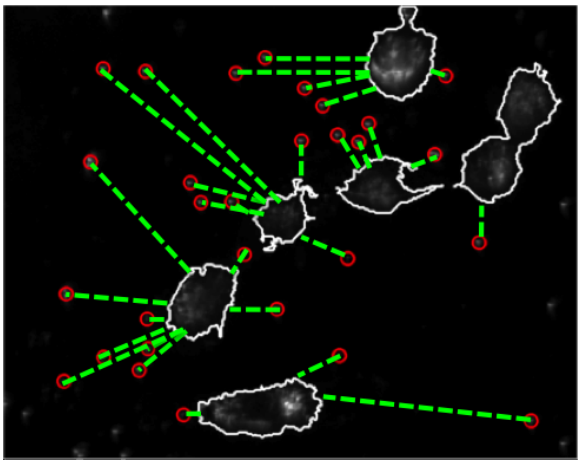

Fig 3.4. Measuring particle center (red circles) to cell boundary (white lines) distance, *r*. Measured *r* are shown as dashed green lines.

centers determined, the distance between the particle center and each boundary coordinates, r, is measured and the nearest boundary point, shown in Fig. 3.4, is recorded as the particle distance from the cell. Fig 3.5A shows an example histogram of particle-cell distance constructed from the r measured. In Fig 3.5B, the particle-cell potential of mean force, $W(r)$, is shown which is calculated from that histogram with a Boltzmann probability analysis as given by,

$$W(r) = -\ln(p(r)/p(r_m)) \tag{3.2}$$

where r_{ref} is a chosen reference r, where $W(r_{ref}) = 0\ kT$. The interpretation of the obtained potentials will be discussed in *Chapter 6.*

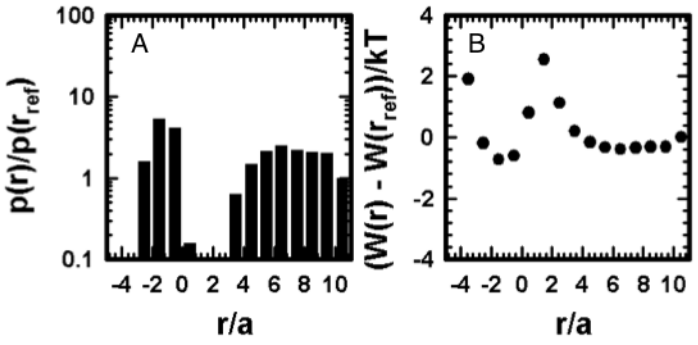

Fig 3.5. (A) Histogram of particle-cell surface distance $p(r)$. (B) Particle-cell surface potential of mean force, $W(r)$, determined from $p(r)$ in (A).

3.4 Umbrella Sampling in Monte Carlo Simulations

3.4.1 Order Parameter Based Biasing Potential

As was explained in *Chapter 2*, Monte Carlo Umbrella Sampling techniques can be used to determine equilibrium and non-equilibrium free energy landscapes by

applying a biasing potential for an order parameter of interest, Ω. The form of this biasing potential should be chosen such that the order parameter is restricted to a specific interval of values. For simplicity, a hard wall biasing potential, $u_b(\Omega)$, was used with the form,

$$\begin{aligned} u_b(\Omega) &= 0 \quad \text{if } \Omega_1 \le \Omega \le \Omega_n \\ u_b(\Omega) &= \infty \quad \text{otherwise} \end{aligned} \tag{3.3}$$

where $u_b(\Omega)$ goes to infinity at values of Ω outside of the interval $[\Omega_1, \Omega_n]$. This ensures any moves outside of this interval will be rejected.

3.4.2 Determining Free Energy Landscapes

Recall from *Chapter 2* for determination of the unbiased free energy landscape, $W(\Omega)$, given by,

$$\frac{W(\Omega)}{kT} = [W_b(\Omega) - u_b(\Omega)] / kT + C_b \tag{3.4}$$

the only unknown parameter is the additive constant C_b which must be determined to extract $W(\Omega)$ from the measured biased free energy landscape $W_b(\Omega)$. This is depicted in Fig. 3.3 where Ω-dependent biased simulations over the three intervals, $[\Omega_1, \Omega_2]$, $[\Omega_3, \Omega_4]$, and $[\Omega_5, \Omega_6]$, would be used to determine the unbiased free energy from the interval $[\Omega_1, \Omega_6]$. The additive constant C_b can be determined by compared over the overlapping

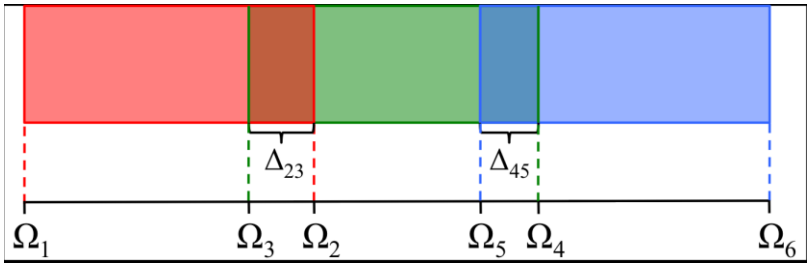

Fig 3.6. Schematic of Umbrella Sampling scheme. Each sampled region is color coded to denote sampling bins at intervals $[\Omega_1,\Omega_2]$ (red), $[\Omega_3,\Omega_4]$ (green), and $[\Omega_5,\Omega_6]$ (blue).

umbrella regions, Δ_{23} and Δ_{45} marked in Fig. 3.3, to find its value in each measured $W_b(\Omega)$. For example in the biased free energy landscape $W_b(\Omega)$ over the interval $[\Omega_1,\Omega_2]$, $W_{b,12}(\Omega)$, the additive constant $C_{b,12}$ is given as,

$$C_{b,12} = C_{b,34} + \frac{\sum_{i=\Omega_3}^{\Delta_{23}} W_{b,12}(i) - W_{b,34}(i)}{\Delta_{23}} \tag{3.5}$$

This again leaves $C_{b3,4}$ as an unknown quantity which can then be determined with comparison to $W_{b,56}(\Omega)$ in the umbrella region $\Delta_{45,}$ and the added designation of Ω_6 as the reference state where $W(\Omega_6) = 0\ kT$. From equation (3.4), the additive constant $C_{b,56}=W_b(\Omega_6)$ and Equation (3.5) can be similarly posed for $C_{b,34}$ as

$$C_{b,34} = C_{b,56} + \frac{\sum_{i=\Omega_5}^{\Delta_{45}} W_{b,34}(i) - W_{b,56}(i)}{\Delta_{45}} \tag{3.6}$$

3.5 *Monte Carlo Move Algorithms*

3.5.1 3D Rotational Receptor Moves

In order to maintain uniform spacing between the receptors and the surface while making 3D receptor rotational moves, the rotations made must be uniform in Euclidean space. The following algorithm was developed by Arvo to make random, uniform rotational moves:[113]

1. Rotate randomly about the z axis by applying the rotation matrix, R:

$$R = \begin{vmatrix} \cos(2\pi\delta_1) & \sin(2\pi\delta_1) & 0 \\ -\sin(2\pi\delta_1) & \cos(2\pi\delta_1) & 0 \\ 0 & 0 & 1 \end{vmatrix} \tag{3.7}$$

2. Rotate randomly from the position (0, 0, $a + h_{rec}$) to a random position by using the Householder matrix, H:

$$H = I - 2vv^T \tag{3.8}$$

where v is the matrix,

$$v = \begin{vmatrix} \cos(2\pi\delta_2)\sqrt{\delta_3} \\ \sin(2\pi\delta_2)\sqrt{\delta_3} \\ \sqrt{1-\delta_3} \end{vmatrix} \tag{3.9}$$

3. The final rotation can be defined with matrix, M as:

$$M = -HR \tag{3.10}$$

where δ_1 is a random variable that ranges from 0 to 1 and the random variables δ_2 and δ_3 also range from 0 to a maximum rotational step size, s_{rot}. A maximum value of 1 x 10^{-3} for s_{rot} was found empirically to not disturb the equilibrium receptor coverage and allowed for efficient configurational sampling.

3.5.2 Colloid-Ligand Cluster Moves

In order to allow our colloids to freely diffuse with dense coverages of ligands on their surface, cluster moves were used to translate all interacting colloids and ligands when attempting colloidal MC moves. The following algorithm was used to decide whether to accept or reject the cluster moves:

1. Determine number of ligands, n, bound to a receptor on the colloid ($r < a_{lig} + \delta$)

2. Move n ligands on colloid with same translation and rotation as attempted by the colloid and receptors in that step.

3. Calculate total change in energy due to the cluster move, ΔE, for colloid and the n ligands bound.

$$\Delta E = \Delta E_{part} + \sum^{n} \Delta E_{lig} \tag{3.11}$$

where ΔE_{part} is the change in energy of the nanoparticle and ΔE_{lig} is the change an energy of a ligand.

4. If ΔE is less than or equal to zero or $e^{(-\Delta E)}$ is greater than a random integer, the cluster move is accepted.

By applying the metropolis criterion to these cluster moves, the potential for biasing in these moves was avoided. MC move efficiency of the colloid and ligands was still maintained for particles with dense coverages of ligands on their surface with a minimum of ~78% acceptance rate.

4. REVERSIBLE COLLOIDAL AGGREGATION MEDIATED BY PROTEIN-CARBOHYDRATE INTERACTIONS

4.1 Introduction

Protein-carbohydrate interactions are essential to many processes in biology with clinical significance such as cell-cell signaling, recognition, self-renewal and migration. Specifically, adhesion of cells to neighboring cells and extracellular matrix (ECM) can be induced through weak, specific protein-carbohydrates interactions. As adhesive agents, glycosolated (carbohydrate-modified) proteins and lipids can be presented as cell surface-immobilized membrane components and in a number of cases, soluble saccharide-binding proteins known as lectins and carbohydrates can be produced as soluble factors that can induce or inhibit adhesion. For example, β-galactoside binding lectins, termed galectins, are secreted by lymphocytes into the ECM and can link together cells through binding of the carbohydrate domains of glycoproteins expressed on their surface. [114, 115, 116] Hyaluronic acid (HA) is a polysaccharide found in the ECM that is recognized by the membrane protein CD44 to mediate cell-ECM adhesion and upregulated production of soluble HA has been linked to metastatic behavior in cancer cells.[10, 117] Bacterial pathogens produce galactose binding lectins, LecA and LecB, to stimulate lectin-polysaccharide mediated cohesion in biofilm matrices in order to initiate formation and maintain stability of biofilms.[118, 119] Many of these proteins exist as dimers and tetramers capable of multi-valent carbohydrate binding and in order to induce adhesion at biological interfaces, many of these weak protein-carbohydrate binding events must occur simultaneously. Multi-valency on both the biomacromolecular and interfacial scale makes possible a wide range of adhesion strengths from weak and reversible to strong and irreversible.

Binding of lectins to surface-immobilized polysaccharides,[120] glycans,[121] and glycolipids[122] have been measured with surface spectroscopy methods to determine the effects of surface binding equilibria and valency on adsorption isotherms. To quantify adhesion mediated by protein-carbohydrate interactions, mechanical and optical force measurement techniques have been employed. Atomic force microscopy (AFM) has been used to directly measure protein-carbohydrate binding at the single molecule level as well as on a multi-valent interfacial level. Lectin-polysaccharide,[123] lectin-glycoprotein,[124] and lectin-coated colloid-cell interactions[125] have been probed with AFM to measure rupture forces and binding lifetimes. Total internal reflection microscopy (TIRM) has been used to directly measure particle-wall interactions, binding lifetimes, and binding isotherms between lectin-decorated colloids with substrates functionalized with polysaccharides.[126] Mannose[123] and glucose[126] were also introduced to determine their impact on lectin-polysaccharide mediated adhesion where these monosaccharides could act to inhibit lectin-polysaccharide binding. However in each of these measurements, the surface density of lectins and carbohydrate ligands remains unchanged as the molecules are chemically grafted or physisorbed to the surface. As we have pointed out, many biological systems will have adsorption of lectins and carbohydrates dependent on other biomolecular cues that can strengthen or weaken adhesion. In this case, competitive lectin-monosaccharide binding will not only affect overall lectin-polysaccharide mediated adhesion, but also the relative surface coverage of lectins or polysaccharides.

The stability in colloidal suspensions can also be related to the interfacial interactions between colloids. Optical microscopy measurements have been used to monitor particle-particle association in 2D concentrated colloidal dispersions mediated by

specific binding in a range of biomacromolecular systems including lectins,[68] DNA,[64] and membrane proteins.[127] The association kinetics and equilibrium structure in these colloidal systems can be attributed to the effective colloidal interactions induced by specific biomacromolecular binding at their interfaces. Although these interactions cannot be directly measured as in AFM and TIRM measurements, the association of colloidal particles in these suspensions will also be highly sensitive to the net colloidal interactions and compared to direct single probe (AFM) and single particle (TIRM) measurements, a greater amount of statistics can be easily obtained with many particle-particle collisions occurring. This is ideal for measurement of adhesion induced by weak, specific protein-carbohydrate interactions where weak, reversible binding events can occur.

In this work, quasi-2D concentrated dispersions will be used to measure surface adsorption and aggregation kinetics mediated by specific protein-carbohydrate interactions. As illustrated in Figure 4.1, specific binding between the lectin Concanavalin A (ConA) and dextran immobilized on the colloidal surfaces will lead to adsorption of ConA onto the colloidal surfaces and once adsorbed, ensembles of weak ConA-dextran bonds can form between colloidal particles. Glucose can act as an inhibitor of specific ConA-dextran interactions and will lead to changes in both the amount of surface adsorption and strength of ConA-dextran binding. This gives us the unique ability to interrogate how both the ConA surface coverage and strength of binding affect the resulting net particle-particle interactions by changing the concentration of ConA and also with the addition of glucose. Using laser scanning confocal microscopy (LSCM), the adsorption of ConA to dextran-modified colloidal particles can be visualized and with

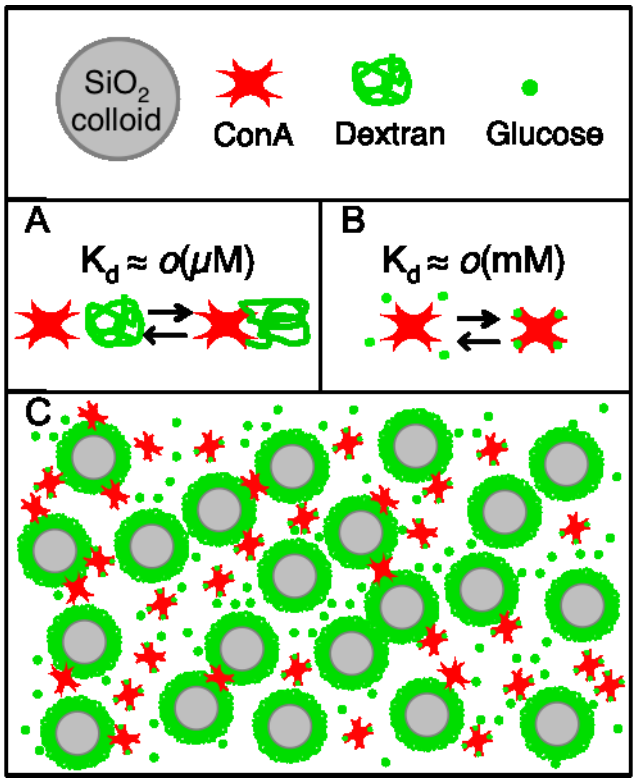

Figure 4.1. Schematics of (A) reversible ConA-dextran binding, (B) reversible ConA-glucose binding and (C) reversible aggregation in a quasi-2D dispersion of dextran coated colloids mediated by competitive ConA-dextran and ConA-glucose binding.

video microscopy (VM), the rate of aggregation was quantified as a function of ConA and glucose concentration. By visualizing the adsorption of ConA to the particle surface with LSCM, the effects of changing ConA and glucose concentration on ConA surface adsorption are clearly demonstrated and with this, connections between the surface coverage of ConA and observed aggregation rate from VM can be established.

Aggregation kinetics in this system will be greatly impacted by changes in net particle interactions mediated by the protein-carbohydrate binding and using a stability ratio analysis, we will relate the observed colloidal stability to the net particle-particle interactions. Ultimately, the findings from this work allow us to understand how to manipulate protein surface adsorption and bridging mediated by weak, specific protein-carbohydrate interactions to reversibly tune net colloidal interactions.

4.2 Theory

4.2.1 Interaction Potentials

For a quasi-2D concentrated dispersion of colloidal particles diffusing over a surface, the overall net interactions of each particle, u_{net}, will be dependent on both the net particle-wall interaction potential, u_{pw}, and the net particle-particle interaction potential, u_{pp}, given by,

$$u_{net}(h,r) = u_{pw}(h) + u_{pp}(r) \tag{4.1}$$

where h is the particle-wall surface separation and r is the particle-particle surface separation. Specifically for a polysaccharide-coated particle diffusing over a polymer-coated substrate at physiological ionic strength in the presence of adsorbing and non-adsorbing proteins, the net particle-wall interaction potential is given by,

$$u_{pw}(h) = u_G^{pf}(h) + u_V^{pw}(h) + u_S^{pw}(h) \tag{4.2}$$

where the subscripts refer to gravitational (G), van der Waals (V), and steric (S) interactions and the superscripts refer to particle-field (pf) and particle-wall interactions (pw). Electrostatic interactions are negligible at physiological ionic strengths where the Debye length is ~1 nm and depletion attraction induced by non-adsorbing proteins can be ignored with volume fractions less than 0.001 in all cases. The gravitational potential energy of each particle is dependent upon its height above the wall, h, and its buoyant mass, m, given by,

$$u_G^{pf}(h) = mgh = \frac{4}{3}\pi a^3(\rho_p - \rho_f)gh \tag{4.3}$$

where g is the acceleration due to gravity, a is the particle radius, ρ_p is the particle density, and ρ_p is the fluid density. van der Waals attraction between two flat plates can

be predicted by Lifshitz theory[79] with retardation and screening effects incorporated using the Derjaugin approximation to account for geometric effects[80] (e.g. sphere-wall, sphere-sphere). For simplicity, an inverse power law approximation can be used to model van der Waals interactions between a particle and a wall, given by,

$$u_V^{pw}(h) = -aA_{pw}h^p \tag{4.4}$$

where A_{pw} is an effective Hamaker constant appropriate over a short range (h < 15 nm) and p is a noninteger power. The fitting constants A_{pw} and p can be adjusted depending upon the dielectric properties of the materials. Repulsive steric interactions will occur at the interface between the particle and the wall due to compression of the macromolecules at their surfaces and this can be modeled with a short range exponential given by,

$$u_S^{pw}(h) = \Gamma \exp(-\kappa h) \tag{4.5}$$

where Γ and κ are determined by the structure of the macromolecular layers at the interface.

For polysaccharide-coated particles at physiological ionic strength in the presence of adsorbing and non-adsorbing proteins, the net particle-particle interaction potential is given by,

$$u_{pp}(r) = \sum_{i \neq j} u_V^{pp}(r_{i,j}) + u_S^{pp}(r_{i,j}) + u_B^{pp}(r_{i,j}) \tag{4.6}$$

where the subscripts refer to van der Waals (V), steric (S), and specific biomacromolecular interactions (B) and the superscripts refer to particle-particle interactions (pp). van der Waals interactions between two particles can also be modeled with an inverse power law approximation given by,

$$u_V^{pp}(r) = -2aA_{pp}r^p \tag{4.7}$$

where A_{pp} is an effective Hamaker constant scaled to $0.5A_{pw}$ to account for the Derjaugin geometric correction and steric interactions between two particles can be modeled with a short-ranged exponential given by,

$$u_S^{pp}(r) = \Gamma \exp(-\kappa r) \tag{4.8}$$

ConA will reversibly adsorb to the surface of the colloidal particles due to specific interactions with the dextran on the colloidal surfaces. ConA can simultaneously bind to up to 4 glucose subunits on the dextran chains and this also allows for bridging between colloidal particles via ConA-dextran binding events. To model particle-particle interactions mediated by ensembles of ConA bridges forming reversibly between particles, an isotropic harmonic well attractive potential can be added with the form,

$$u_B^{pp}(r) = U_{\min}\left(\frac{r - r_{\min}}{r_{\min}}\right)^2 \tag{4.9}$$

where $U_{\min}$ is the depth of the harmonic well and $r_{\min}$ is the position of the harmonic potential well minimum. The resulting overall particle-particle interaction potential can be well described by a Morse harmonic potential[87] given by,

$$u_{pp}(r) = U_{\min}[1 - \exp(-k(r - r_{\min})]^2 - U_{\min} \tag{4.10}$$

where k is the decay length that controls the range of the harmonic well.

4.2.2 Hydrodynamic Interactions

A colloidal particle near a planar substrate will experience hydrodynamic interactions that will hinder the lateral motion of the particle from its predicted Stokes-Einstein diffusivity, where $D_o = kT/(6\pi\mu a)$, and these effects can be accounted for with a hydrodynamic correction factor[88] as,

$$D_{\parallel}(h) = D_o f_{\parallel}(h) \tag{4.11}$$

where $f_{||}$ is a rational fit to the exact solution[89] as,

$$f_{\parallel}(h) = \frac{1220\omega(h)^2 + 5654\omega(h) + 100}{12420\omega(h)^2 + 12233\omega(h) + 431} \tag{4.12}$$

where $\omega(h) = h/(a+\delta_{dex})$ and δ_{dex} is the dextran layer thickness. The distribution of heights sampled by the particle, $p(h)$, can be related to the net particle-wall interaction potential with Boltzmann's equation as,[90, 91]

$$p(h) = \exp(\frac{-u_{pw}(h)}{kT}) \tag{4.13}$$

and predictions of the average lateral diffusion coefficient, $\langle D_{||} \rangle$, can be made using the distribution of heights sampled given by,[92]

$$\left\langle D_{\parallel} \right\rangle = \frac{\int D_{\parallel}(h) p(h)\, dh}{\int p(h)\, dh} \tag{4.14}$$

In quasi-2D concentrated dispersions, particle-particle hydrodynamic interactions will further hinder the diffusion of the particles and the lateral diffusion coefficient can be predicted for particles in concentrated solutions with the correction factor, f_{pp}, as, [93]

$$D_{\parallel,pp}(r) = f_{pp}(r) < D_{\parallel} > \tag{4.15}$$

where $f_{pp}(r)$ is a rational fit to exact solutions as,[94]

$$f_{pp}(r) = \frac{54\gamma(r)^3 + 71\gamma(r)^2 + 8\gamma(r)}{54\gamma(r)^3 + 154(r)^2 + 60\gamma(r) + 4} \tag{4.16}$$

where $\gamma(r)$ = r/(a+δ_{dex}).

Aggregation Kinetics

To experimentally determine the rate of aggregation, the rate of singlet particle disappearance can be measured over time. A simple mass balance can be used to describe the singlet disappearance rate as,[95]

$$\frac{d\phi_1}{dt} = -2k_{11}\phi_1^2 - \sum_{i=2}^{N} k_{1i}\phi_1\phi_i \tag{4.17}$$

where ϕ_1 is the areal number density of aggregates consisting of i particles and k_{1i} is the rate constant for aggregation of single particles with aggregates of size i. For an initially stable dispersion, formation of doublets from single particles will largely determine the rate of singlet disappearance at the early stages of aggregation and this allows the singlet disappearance rate to be further reduced to,

$$\frac{d\phi_1}{dt} = -2k_{11}\phi_1^2 \tag{4.18}$$

We can then integrate Eq. (4.18) with respect to time with an initial singlet concentration of $\phi_{1,o}$ at $t = 0$ which yields,

$$\frac{\phi_{1,o}}{\phi_1} = 1 - 4k_{11}\phi_{1,o}t \tag{4.19}$$

Eq. (4.19) shows that the ratio of the initial singlet concentration to the singlet concentration at time t should increase linearly with time and have a slope that is dependent upon the singlet aggregation rate constant, k_{11}. A Smoluchowski singlet aggregation rate constant can be calculated for particles diffusing in 2D as,[97]

$$k_{11,Smol} = \frac{2\pi \left\langle D_{\|} \right\rangle}{\ln\left[\dfrac{(\pi\phi_{1,o})^{-1/2}}{r_{agg}}\right]} \tag{4.20}$$

where r_{agg} is the particle encounter radius where r_{agg} = a $+\delta_{dex}$ + a_{ConA} and a_{ConA} is the radius of gyration of ConA. To compare the rate for diffusion-limited aggregation to that found in experiment, the stability ratio can be calculated as,

$$W = \frac{k_{11,Smol}}{k_{11,\exp}} \tag{4.21}$$

where k_{exp} is the aggregation rate constant measured experimentally at early times. We can define the time frame of early kinetics using a collision rate time constant that we have defined as,

$$\tau = \frac{r_{\phi}^{\ 2}}{\left\langle D_{\|} \right\rangle} \tag{4.22}$$

where r_ϕ is the average radial distance between particles given by,

$$r_{\phi} = \phi_{1,o}^{-1/2} - (2a + 2\delta_{dex}) \tag{4.23}$$

The stability ratio can then be related to net particle-particle interactions. Using the pairwise colloidal interaction potential defined in Eq. (4.10), stability ratios can be predicted for aggregation into a secondary minimum with a modified Fuchs integral given by,[99]

$$W = \varepsilon^{-1}(2a + \delta_{dex})\left\langle D_{\|} \right\rangle \int_{r_{\min}}^{\infty} \frac{\exp(u_{pp}(r)/kT)}{(r + 2a + \delta_{dex})^2 D_{\|,pp}(r)} dr \tag{4.24}$$

where ε is the probability a particle has the thermal energy required to escape the secondary minimum defined as,

$$\varepsilon = 1 - \exp(U_{\min}/kT) \tag{4.25}$$

where it is assumed that the particles have a Boltzmann distribution of thermal energies.

4.3 Materials and Methods

4.3.1 PEG-Coated Microscope Slide

Glass microscope slides (Fisher Scientific, Pittsburgh, PA) were sonicated in acetone for 30 minutes then placed in Nochromix (Godax Laboratories, Cabin John, MD) overnight. The slides were then rinsed 20x times with DI water then sonicated in 0.1 M KOH for 30 minutes. They were again rinsed 20x times with DI water and dried with nitrogen. Polystyrene-coated glass microscope slides were made using a spin coater (Laurell Technologies Corp., North Wales, PA) by placing a ~1 mL drop of a 3% (w/w) solution of polystyrene in toluene onto the glass microscope slides and spinning at 1,000 RPM for 40 s. A batch cell is made on the polystryrene-coated microscope slide by adhering a 1 mm ID Viton O-ring (McMaster Carr, Inc., Robbinsville, NJ) onto the slide with vacuum grease. F108-Pluronic (PEG-PPO-PEG triblock copolymer, BASF, Wyandotte, MI) was physisorbed to the polystyrene-modified glass microscope slides by adding 25 μL of 1000 ppm (1 mg/mL) solution of F108-Pluronic in DI water to the O-ring and it is allowed to adsorb for at least 4 hours. Before each experiment, the cell is rinsed 5x times with phosphate buffered saline (PBS, Invitrogen, Carlsbad, CA) to remove excess, unadsorbed F108.

4.3.2 Dextran-Modified Colloidal Silica

Nominal 2.34-μm silica microspheres (Bangs Laboratories, Fishers, IN) were functionalized with dextran by chemisorption to the surface of the particle through an epoxy silane linkage.[109, 126] Before functionalization, the silica particles were washed using a micro-centrifuge (MiniSpin-plus, Eppendorf, Hamburg, Germany) by centrifugation at 55,000 RPM for 90 s followed by re-dispersion in fresh DI water. This washing step was repeated 5 times. The particles were then dispersed in dry ethanol and

washed an additional 5 times in dry ethanol. The particles were then dispersed in a 0.1% (v/v) 3-glycidoxypropyltrimethoxysilane (GPTMS, Sigma, St. Louis, MO) in dry ethanol for 1 hour. The GPTMS-modified silica colloids were then washed 5 times in dry ethanol and 5 times in DI water. They were then dispersed in 30% (w/w) aqueous solution of 500 kDa dextran and gently mixed with a magnetic stir bar for 24 hours. The dextran-modified particles are then centrifuged at 10,000 RPM for 10 minutes and re-dispersed in fresh DI water. They are then washed with DI water an additional 5 times. Pluronic-F108 is then physisorbed onto the dextran-modified particles by dispersing the particles in 1000 ppm (1 mg/mL) aqueous solution of F108-Pluronic overnight. The F108 coating step is to ensure the particles are fully coated with a polymer brush to improve colloidal stability. The particles are then rinsed 5 times in DI water and then dispersed in PBS.

4.3.3 Video Microscopy

Twenty-five μL of dextran-coated silica particle solution is added into a PEG-coated batch cell and particles are allowed to sediment for 10 minutes to create a concentrated quasi-2D dispersion as shown in a schematic in Figure 1C. A stock solution of 10 μM ConA (Sigma, St. Louis, MO) in PBS was filtered with a 0.2 μm filter (SFCA, Fisher Scientific, Pittsburgh, PA) and used to create all concentrations of ConA and glucose solutions. Before each experiment, the solution in the O-ring was switched with solutions of ConA and glucose in PBS. The cell is then covered with a glass coverslip. Experiments were performed using an inverted optical microscope (Axioplan 2, Carl Zeiss, Obercheken, Germany) with a 63x objective (LD-Plan Neofluar, NA = 0.75, Carl Zeiss). Before each experiment, the solution in the O-ring was switched with solutions of ConA and glucose in PBS. The cell is then sealed with a glass microscope coverslip.

Once the cell is sealed, images are collected with a 12-bit CCD camera (ORCA-ER, Hamamatsu, Hamamatsu City, Japan) operated in binning mode 4 (length per pixel, l_{pp} = 385 nm/pixel, Image area, A_i = 336 x 256 pixels = 129 x 98.56 μm^2) at a 0.5 s frame rate for a total of 3600 frames (1 hr duration). The particle coordinates in each frame are determined using image analysis algorithms coded in FORTRAN. The number of associated particles can then be tracked by measuring the distance between particle centers, $R_{ij,}$, in each frame. If R_{ij} was less than a cutoff radius, $R_{cut} = 2a + l_p$, particles *i* and *j* are considered associated.

4.3.4 Laser Scanning Confocal Microscopy

All experiments were performed in cells consisting of a 1 mm ID Viton O-ring sealed with vacuum grease to a bare glass cover slip (Corning Life Science, Tewskbury, MA). Twenty-five μL of dextran-coated silica particle in PBS is added to the O-ring and particles are allowed to sediment for 10 minutes. Since the glass coverslip is bare, the particles will irreversibly adhere to the surface due to van der Waals interactions and allowing for subsequent imaging in both reflection mode, to image particles, and fluorescence mode, to image ConA, that could be later overlayed. A stock solution of 10 μM fluorescein isothiocyanate-conjugated ConA (FITC-ConA, Sigma, St. Louis, MO) in PBS was filtered with a 0.2 μm filter and used to create all concentrations of ConA and glucose solutions. Once the particles are immobilized, the solution in the O-ring is switched with solutions of FITC-ConA and glucose in PBS. Images were collected using an inverted confocal microscope (Axio Observer.Z1, Carl Zeiss) with a mounted scanning laser (LSM 5 Pascal Scanner, Carl Zeiss) and an oil-immersion 63x objective

(Apochromat, NA = 1.45, Carl Zeiss). A 102 μm x 102 μm area was scanned in reflection and fluorescence mode with a 488 nm 500 mW Ar laser as an excitation source.

4.4 Results and Discussion

4.4.1 Specific Adsorption of ConA to Dextran-Modified Colloids

In prior work,[126] we first demonstrated how strong attraction was induced via ConA-dextran tethering between a particle and a surface. Although ConA has only a weak affinity for dextran, multiple ConA-dextran bridges between the particle and the wall lead to very strong, irreversible net particle-wall interactions. These particle-wall interactions could be further tuned using a monosaccharide like glucose to weaken ConA-dextran interactions which in turn weakened the net particle-wall interactions. Using these same principles, we will now show how particle-particle interactions can be manipulated by using multi-valent ConA-dextran interactions to induce attraction between dextran-functionalized colloids.

In Figure 4.2, we begin by first visually demonstrating the effects of varying ConA concentrations on the amount of adsorbed ConA to the surface of dextran-functionalized particles with LSCM imaging and how that relates to particle-particle association with snapshots from VM experiments. Adsorption to a surface leads to concentrations at the interface that are higher than that of the bulk concentration. This can be qualitatively illustrated with fluorescent images of ConA-FITC where fluorescent intensities greater than the bulk fluorescent intensity will clearly indicate where ConA adsorption has occurred. Combining fluorescent imaging of ConA-FITC with reflectance imaging to show where particles are located then allows us to show when ConA has specifically adsorbed to the surface of the dextran-modified particles. Snapshots from

VM experiments of quasi-2D concentrated dispersions of dextran-modified particles after 1 hr in solutions of ConA illustrate how altering ConA-dextran mediated particle-particle interactions leads to changes in the stability of the dispersions.

Noticeable variations in the amount of ConA specifically adsorbed to the particles

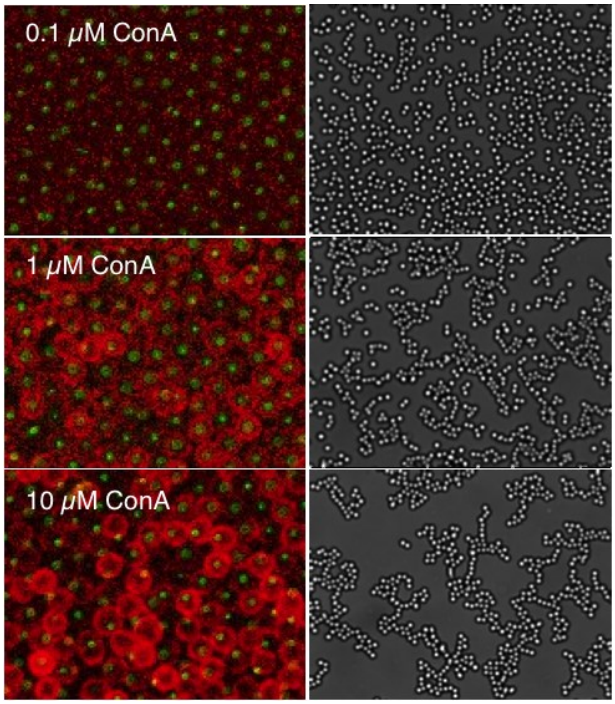

Figure 4.2. 2 μm dextran-modified silica colloids in the presence of ConA. The left column shows static images of dextran modified colloids (shown in green) taken from LSCM in varied concentrations of ConA-FITC (shown in red) and glucose. The right column shows the final snapshot taken at t = 1 hr from VM experiments at the corresponding concentrations of ConA.

are observed for ConA concentrations ([C]) ranging from 0.1 μM – 10 μM range and this is shown in the left column of Figure 4.2. When [C] = 0.1 μM, no ConA adsorption can be seen on the surface of the dextran-modified particles. When [C] = 1 μM, we begin to see ConA accumulate on the surface of the particles and an even greater amount ConA adsorbs to the surface of the particles at [C] = 10 μM. These variations in adsorption are

not unexpected in these concentration ranges as the equilibrium surface coverage will be dependent on the ConA-dextran dissociation constant, K_C. A simple Langmuir isotherm model can be used to relate the equilibrium surface coverage to K_C as given by,

$$\theta = \frac{K_C^{-1}[C]}{1 + K_C^{-1}[C]} \tag{4.26}$$

where K_C^{-1} (i.e. ConA-dextran association constant) is the adsorption coefficient.

The high equilibrium surface coverages observed with [C] = 1 and 10 μM are reasonable based on reported K_C from 0.1-1 μM.[128, 129] The apparent vanishing of ConA surface adsorption at a bulk ConA concentration of 0.1 μM would support an estimated K_C closer to 1 μM. However, a simplified Langmuir isotherm model, more appropriate for monovalent surface adsorption, does not account for cooperativity or multi-valency of ConA-dextran interactions which could also play an important role in the expected surface coverage.

In the right column of Figure 4.2, the final snapshot at t = 1 hr in VM experiments is shown at the same ConA concentration range from 0.1 - 10 μM. At [C] = 0.1 μM, the quasi-2D dispersion of dextran-coated particles largely remains in a stable, fluid state where only a few small clusters of associated particles have formed. When the concentration is increased to 1 μM, a majority of the particles have associated into larger clusters. At [C] = 10 μM, all particles have associated into large fractal-like aggregates. The presence of these large clusters at [C] = 1 and 10 μM indicates a net attraction between the colloidal particles which can be related to the ConA adsorption that was observed in the left column of Figure 4.2. Since ConA is a tetramer capable of binding up to 4 glucose subunits of the dextran chains, ConA can specifically adsorb to two particles once the particles come into contact to create a bridge. Multiple, simultaneous

occurrences of weak ConA-dextran bridging events can then lead to strong, net particle-particle interactions.

Net particle-particle interaction potentials induced by specific ConA-Dextran binding will be examined further in later sections, but inferences to the differences in particle-particle interactions at varied [C] can be made from the final state of the dispersion and the structure of the aggregates that have formed. The weakest particle association is clearly observed at [C] = 0.1 μM where only a few clusters of particles have formed. It is clear at both [C] = 1 μM and 10 μM, many large clusters have formed due to strong net attraction between the colloids. However, the aggregates at [C] = 1 μM are noticeably more compact than those seen at [C] = 10 μM which have a more stringy and fractal-like structure. Fractal aggregate formation is characteristic of aggregation in the reaction-limited regime in systems with strong, irreversible particle-particle interactions.

4.4.2 Effects of Competitive ConA-Glucose Binding

In Figure 4.3, LSCM imaging of ConA on dextran-coated colloids and snapshots from VM experiments are shown at a fixed ConA concentration and varied glucose concentrations to illustrate the effect of introducing a monosaccharide inhibitor of ConA-dextran interactions. We can again visualize the particle surface adsorption of ConA with fluorescence-reflectance image overlays to assess the effect of competive ConA-glucose binding on the specific adsorption of ConA to dextran-coated colloids. The stability of dispersions of dextran coated colloids in the presence of ConA and glucose can be shown visually in the final snapshots taken from VM experiments.

In the left column of Figure 4.3, LSCM images are shown at a fixed 10 μM ConA concentration and varied glucose concentrations ([G]). When [C] = 10 μM in the absence of glucose, we observed the greatest amount of ConA adsorption to the particles as shown in the left column of Figure 4.2. At [C] = 10 μM and [G] = 1 mM, we still see a large amount of ConA adsorbed to the surface as was previously seen in the absence of glucose. When [G] is increased to 10 mM, there is a significant decrease in the amount of ConA adsorbed to the surface of the dextran-coated particles. Finally at [G] = 100 mM, virtually no ConA adsorbs to the surface of the particles. By introducing glucose at these conditions, we anticipated that ConA particle surface adsorption would be greatly impacted by glucose occupying and potentially displacing dextran from ConA binding.

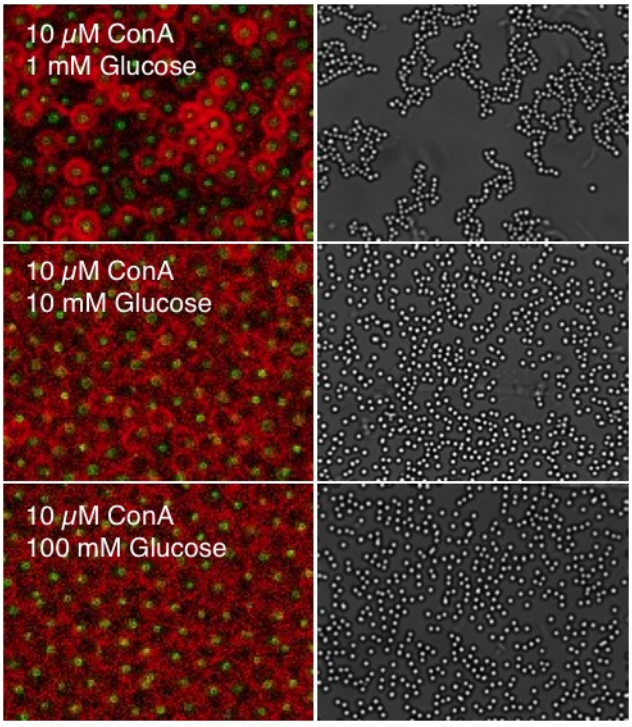

Figure 4.3. 2 μm dextran-coated silica colloids in the presence of ConA and glucose. The right column shows static images of dextran-coated colloids (shown in green) taken from LSCM in varied concentrations of ConA-FITC (shown in red) and glucose. The left column shows the final snapshot taken at t = 1 hr from VM experiments at the corresponding concentrations of ConA and glucose.

We can rationalize the observed changes in surface adsorption as competitive inhibition of ConA-dextran interactions with glucose. By adding glucose as a competitive monosaccharide, the interactions between ConA and dextran will be effectively weakened and as a result, changes to K_C to an effective dissociation constant, $K_{C,eff}$, which can be calculated as,

$$K_{C,eff} = K_C(1+\frac{[G]}{K_G}) \tag{4.27}$$

where K_G is the ConA-glucose dissociation constant. As [G] increases to values on the order of K_G, $K_{C,eff}$ will begin to increase and this will lead to decreases in the equilibrium surface coverage as predicted in Eq. (4.27). With reported K_G ranging from 1-25 mM,[33, 130, 131] the trends observed in the surface adsorption of ConA as a function of glucose concentration are reasonable within this range of concentrations.

The right column of Figure 4.3 shows the final snapshots from VM experiments at a 10 μM ConA concentration and glucose varied over the same range from 1-100 mM. In the absence of glucose, all particles were associated into large fractal aggregates at [C] = 10 μM as shown in the right column of Figure 2. At [G] = 1 mM, large fractal aggregates were also observed after 1 hr. At [G] = 10 mM, only a small fraction of particles associate into clusters and at [G] = 100 mM, the dispersion remains in a stable, fluid state. We can again relate these trends to changes in net particle-particle interactions mediated by ConA-dextran binding. Introducing glucose will not only reduces the amount of ConA adsorb to the surface, but it will also hinder ConA-dextran bridge formation as a result of the effective weakening of ConA-dextran interactions. The combination of lower ConA surface coverages and weaker ConA-dextran bridges due to competitive ConA-glucose binding explains the resulting weakening of net particle-

particle attraction.

4.4.3 Aggregation Kinetics of Dextran Coated Colloids in ConA and Glucose

In Figure 4.4, we quantify the aggregation kinetics of dextran-modified particles in the presence of ConA and glucose by tracking the areal number density of unassociated particles, ϕ_1, over time. By using a criteria based on the particle-particle separation, we are able to identify when colloidal particles are in contact. However even in stable quasi-2D concentrated dispersions, a number of particles that are not necessarily associated into doublets or larger clusters can be in contact due to the high particle collision frequency. To account for this, we can use a singlet ratio, $\theta_1 = \phi_1/\phi_{1,o}$, where $\phi_{1,o}$ is the initial areal number density of singlets. Compared to a stable, concentrated dispersion, the number of apparent singlet particles will be greatly reduced as clusters of particles form due to aggregation. By using the singlet ratio, the progression from an initially stable dispersion to an unstable, aggregated dispersion can be more easily monitored.

In Figure 4.4A, aggregation kinetics are presented for quasi-2D concentrated dispersions of dextran-coated particles with [C] ranging from 0.01 μM to 10 μM. At [C] = 0.01 μM (yellow diamonds), no aggregation is observed as the singlet ratio fluctuates at values from 0.9 to 1. At [C] = 0.1 μM (green squares), particles slowly aggregate and after 1 hour, approximately half of the initial singlets have associated into aggregates. At [C] = 1 μM (red triangles down), the particles have more rapidly associated into aggregates until reaching a plateau singlet ratio around 0.1 after 2200 s (~37 min). At [C] = 10 μM (black circles), the aggregation rate is further increased reaching the same

plateau value after 700 s (~12 min). It is clear that rate of aggregation is strongly dependent upon [C].

As was explained visually with Figure 4.2, increasing [C] leads to increases in the amount of ConA adsorbed to the particles and this will also increase the frequency of ConA-dextran bridging events between particles. The kinetics of colloidal aggregation will be highly dependent upon interparticle interaction potentials. This is reflected in the observed aggregation kinetics as increasing [C] leads to more rapid singlet disappearance. As the number ConA-dextran bridges increases, stronger net particle-particle attraction will be induced which will increase the rate of particle association.

In Figure 4.4B, aggregation kinetics are shown at fixed [C] = 10 μM and [G] = 0, 0.1, 1, 2, 5, 10, 25, 100 mM to examine how competitive ConA-glucose binding alters aggregation mediated by ConA-dextran binding. In the absence of glucose (black circles), rapid flocculation was observed and this can be compared to the aggregation rate as [G] increases. At 0.1 mM (red triangles down) and 1 mM (green squares), rapid aggregation is still observed with the singlet ratio again reaching a plateau value around ~0.1 after 700 s. At 2 mM (yellow diamonds), the rate of aggregation is slightly hindered and a plateau singlet ratio of ~0.25 is reached. At 5 mM (blue triangles up), the aggregation rate is greatly decreased and a plateau value of 0.1 is eventually reached after 2800 s (~46 min). At [G] = 10 mM (pink hexagons), 25 mM (cyan circles) and 100 mM (gray triangles down), the dispersions remain stable for the duration of the experiment with the singlet ratio fluctuating at values between 0.9 and 1.

As pointed out in the visual interpretation of competitive ConA-glucose binding in Figure 4.3, both adsorption of ConA to the particle and ConA's ability to form

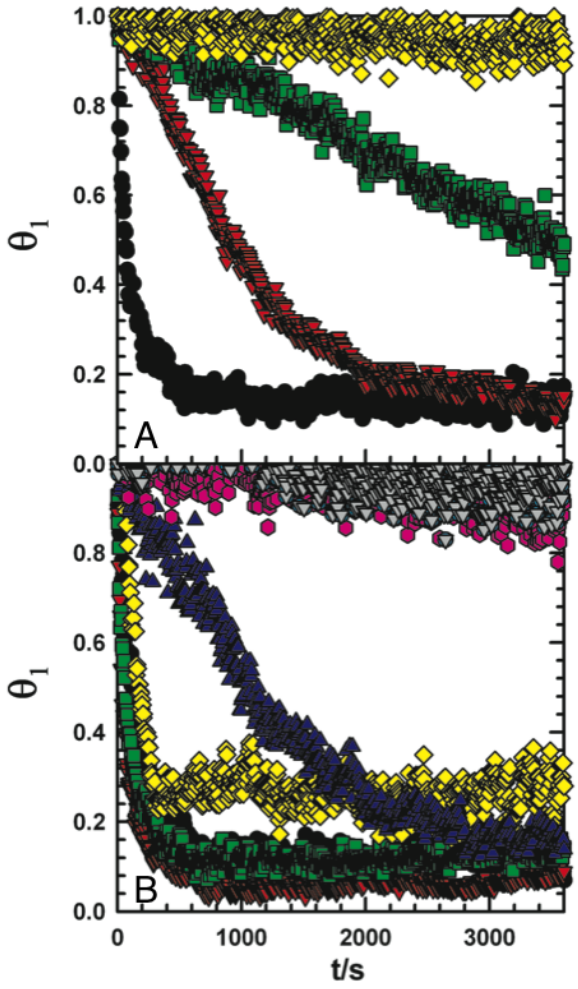

Figure 4.4. Singlet ratio versus time for (A) dextran coated colloids in [C] = 10 μM (black circles), 1 μM (red triangles), 0.1 μM (green squares), 0.01 μM (yellow diamonds) and (B) for dextran coated colloids with [C] = 10 μM and [G] = 0 mM (black circles), 0.1 mM (red triangles down), 1 mM (green squares) 2 mM (yellow diamonds), 5 mM (blue triangles up), 10 mM (pink hexagons), 25 mM (cyan circles), and 100 mM (gray triangles down).

attractive bridges via specific ConA-dextran interactions will be hindered in the presence of glucose. When [G] < 1 mM, no net effect was observed on the aggregation rate. We begin to see weakening ConA-dextran mediated particle interactions at [G] = 2 and 5 mM

with slower aggregation rates however the extent of aggregation is similar to that of the [G] = 0 mM case. Once [G] reaches 10 mM, net particle-particle attraction is significantly reduced and particles no longer associate into aggregates. From these results, it is clearly shown how competitive ConA-glucose interactions can be used to manipulate the net particle-particle interactions by limiting ConA adsorption and effectively weakening specific ConA-dextran interactions.

In Figure 4.5, the inverse singlet ratio is shown as a function of time using the aggregation kinetics at early times for each of the cases shown in Fig. 4.4. In a flocculating suspension, doublets will begin forming from the association of singlet particles at the onset of aggregation. To measure the rate of doublet formation, the inverse of the rate of singlet disappearance can be examined at the early stages of aggregation. As shown in Eq. (4.19), the inverse singlet ratio, $\theta_1^{-1} = \phi_{1,o}/\phi_1$, will increase linearly with time at short times as doublets form and can be used to determine the singlet-singlet reaction rate constant, k_{11}. The rate of single particle association will also be dependent on $\phi_{1,o}$ as the number of collisions between particles increases with increasing particle concentration. A collision rate time constant, τ, can be used to account for these effects and is defined in Eq. (4.20). We can use τ to normalize the time scale of early kinetics in experiments with different $\phi_{1,o}$.

In Figure 4.5A, the inverse singlet ratio is shown as a function time at varied ConA concentration. The lines shown are linear fits to each case to determine the singlet-singlet reaction rate constant reported in Table 1. With [C] = 1 μM and lower, there is no increase in the inverse singlet ratio indicating no doublet formation at short times. When [C] = 10 μM (black circles), θ_1^{-1} increases linearly at short times as was expected and this

is an indication of doublet formation. The rate of singlet-singlet association is clearly influenced [C] as this alters ConA-dextran mediated particle-particle interactions.

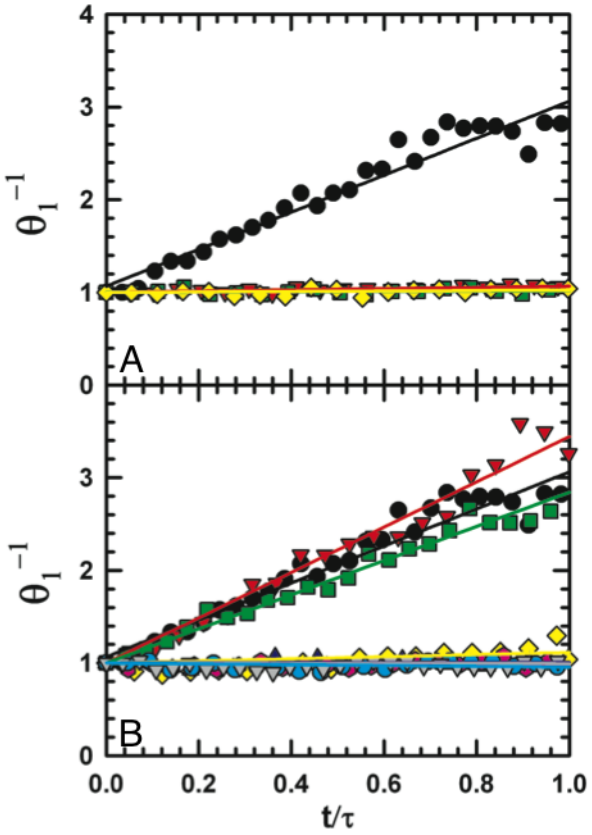

Figure 4.5. Inverse singlet ratio versus time for (A) dextran coated colloids in [C] = 10 μM (black circles), 1 μM (red triangles), 0.1 μM (green squares), 0.01 μM (yellow diamonds) and (B) for dextran coated colloids with [C] = 10 μM and [G] = 0 mM (black circles), 0.1 mM (red triangles down), 1 mM (green squares) 2 mM (yellow diamonds), 5 mM (blue triangles up), 10 mM (pink hexagons), 25 mM (cyan circles), and 100 mM (gray triangles down).

In Figure 4.5B, the inverse singlet ratio is shown as a function time at fixed 10 μM ConA concentration and varied glucose concentration where we can again see the inhibitory effects of competitive ConA-glucose interactions. At [G] < 1 mM, the linear increase in θ_1^{-1} is observed at approximately the same rate seen in the absence of glucose. At [G] > 2 mM, we observe inhibition of doublet formation at short times with little

increase in θ_1^{-1}. In the next section, the rate of doublet formation will be related to pairwise colloidal interactions using a stability ratio analysis.

Table 4.1 Values of $\phi_{1,o}$, τ, measured $k_{11,exp}$ and predicted $k_{11,Smol}$ for diffusion-limited aggregation for each ConA and glucose concentration.

[C] (μM)	[G] (mM)	$\phi_{1,o}$ (μm^{-2})	τ (s)	$k_{11,exp}$ ($\mu m^2/s$)	$k_{11,Smol}$ ($\mu m^2/s$)
0.01	0	0.048	96.8	5.39×10^{-3}	0.845
0.1	0	0.039	140	4.07×10^{-3}	0.744
1	0	0.047	98.8	0.014	0.827
10	0	0.043	116	0.42	0.782
10	0.1	0.051	82.7	0.50	0.874
10	1	0.043	118	0.37	0.782
10	2	0.052	77.2	0.028	0.894
10	5	0.066	43.4	1.76×10^{-3}	1.07
10	10	0.04	131	1.21×10^{-3}	0.757
10	25	0.047	98.8	1.45×10^{-3}	0.827
10	100	0.039	140	7.56×10^{-4}	0.744

4.4.4 Stability Ratio and Net Particle-Particle Interactions

In Figure 4.6, the stability ratio measured from k_{11} is shown and based on the measured stability ratio, predictions of theoretical Morse potential well depth are shown. The stability ratio is used to compare aggregation kinetics at early times in experiment to the expected rate for diffusion-limited aggregation. In order to relate early aggregation kinetics to particle-particle interactions, the stability ratio for theoretical particle-particle interactions potentials can be calculated using Eq. (4.24). In many electrostatically stabilized colloidal systems, an energy barrier may exist that colloidal particles must surmount before irreversibly aggregating at the primary minimum. However, the colloidal particles in this system have macromolecular coatings that provide steric stability and present an essentially infinite barrier to aggregation into the primary minimum. With the primary minimum inaccessible, reversible aggregation due to a

secondary minimum can occur where the range and depth of the secondary minimum will affect the rate of colloidal aggregation. Morse harmonic well potentials are used to model the secondary minimum in this system where the depth of the well is varied as a function of ConA and glucose concentration.

In Figure 4.6A, the stability ratio is shown as a function of ConA concentration. As the ConA concentration increases, the stability ratio decreases from a value near 200 at [C] = 0.1 μM, typical for stable suspensions, to a value near 1 at [C] = 10 μM where the aggregation rate approaches that of the diffusion-limited rate. We can see from this trend that as [C] increases, the system aggregates more rapidly as the ConA-dextran mediated particle-particle attraction increases. By increasing [C], a greater amount of ConA adsorbs to the particles and as a result of this, increases in ConA-dextran bridging events would be expected.

In Figure 4.6B, the stability ratio is shown as function of glucose concentration at a fixed [C] = 10 μM. A stability ratio remains near 1 at glucose concentration below 1 mM. At these low glucose concentrations, ConA-dextran mediated appear undisrupted as the aggreration remains diffusion-limited. At [G] = 2 mM, the stability ratio increases to around 30 and at [G] > 5 mM, the suspension completely re-stabilizes with stability ratios approaching 1000. This threshold value of [G] = 5 mM could be seen as the point where ConA binding sites are saturated due to ConA-glucose interactions. With ConA-dextran interactions inhibited, particle-particle association via ConA-dextran binding will also be limited and the dispersions remain stable.

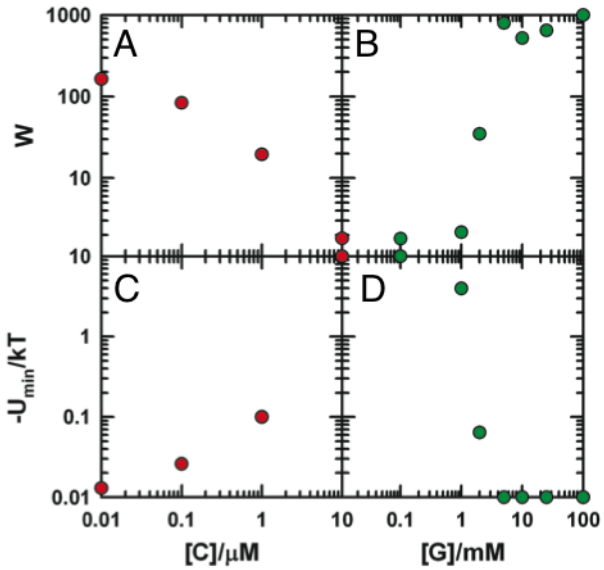

Figure 4.6. Measured stability ratio, *W*, as a function of (A) ConA and (B) glucose concentration shown on a log-log scale. Predicted Morse potential well depth, U_{min}, as a function of (C) ConA and (D) glucose concentration shown on a log-log scale.

In Figure 4.6C, we relate the transitions in colloidal stability as a function of [C] to pairwise particle interactions using a Fuchs integral stability ratio analysis. Using the harmonic well depth, $U_{\min}$, as an adjustable parameter, theoretical Morse potentials are predicted based on the stability ratios measured in experiment. It is expected in this system that a secondary minimum will exist due to ConA bridging between dextran layers. As the frequency and number of these reversible ConA-dextran bridges increases, the depth of the effective particle-particle harmonic well should also increase. At [C] < 1 μM, vary shallow well depths from 0.01 - 0.1 *kT* are predicted where very weak, reversible particle-particle association would be expected. At [C] = 10 μM, the depth well increases dramatically to 10 *kT* where particles would irreversibly adhere at contact. This

result shows how particle-particle interactions can be tuned over a wide range of strengths using weak ConA-dextran interactions.

In Figure 4.6D, we apply the Fuchs stability ratio analysis to predict Morse potential well depths as a function of glucose concentration. At [G] = 1 and 0.1 mM, attractive well depths of ~4 and 10 *kT*, respectively, are predicted indicating very strong particle-particle attraction remains at these low glucose concentrations. The attraction is dramatically reduced at [G] = 2 mM with a well depth of 0.1 kT that then reduces in further to 0.01 *kT* at [G] > 5 mM. Competitive ConA-glucose interactions have a clear effect on the ConA-dextran mediated particle-particle interactions. As more ConA binding sites are occupied by glucose, ConA will more weakly adsorb to the dextran layers which will decrease the strength and overall number of ConA-dextran bridges. With ensembles of these weak, ConA-dextran bridges necessary to induce strong attraction between the particles, a very sharp transition from strong, irreversible particle interactions to weak, reversible particle interactions would be expected due to disruption of ConA-dextran interactions with glucose as an inhibitor.

4.5 Conclusions

Colloidal stability and aggregation kinetics were measured in quasi-2D concentrated dispersions of dextran-modified colloidal particles in the presence of varied ConA and glucose concentrations. Specific adsorption of ConA to dextran-modified colloids was observed using combined confocal fluorescence and reflectance imaging and aggregation kinetics in these dispersions were quantified using optical video microscopy. Instability was induced in the dispersions as ConA concentration increased. Increasing the ConA concentration lead to greater equilibrium coverage of ConA on the surface of

the particles allowing for stronger ConA-dextran mediated particle-particle binding events. Stability could be re-established using glucose as a competitive inhibitor in dispersions that rapidly aggregated at a 10 μM ConA concentration. The presence of glucose lead to lower equilibrium ConA-particle surface coverages and weaker ConA-dextran mediated particle-particle interactions. Using a stability ratio analysis, predictions of net particle-particle interactions were made using the initial rate of aggregation. Future work will aim to make comparisons of the predicted particle-particle interactions to quantitative modeling efforts to further interpret the effects of weak, specific protein-carbohydrate interactions on the observed colloidal interactions.

5. MODELING COLLOIDAL INTERACTIONS MEDIATED BY WEAK, SPECIFIC BIOMACROMOLECULAR BINDING

5.1 Introduction

Specific, reversible interactions between nucleic acids, peptides, proteins, and carbohydrates are critical to many important biological functions. The movement of cells is coordinated through weak protein-protein and protein-carbohydrate interactions for dynamic control of morphology, viscoelasticity, and surface adhesion.[7] Transcription regulator proteins must interact weakly with DNA to facilitate an efficient search through billions of base pairs for target sequences.[132] The onset and progression of many disease states are dependent on processes mediated by weak, specific biomacromolecular interactions such as anomalous self-assembly of proteins in amyloid fibrillogenesis[133] and weakened membrane protein adhesion in cancer metastasis.[134] Weak, specific biomacromolecular interactions have also been exploited in biosensors[135] and drug delivery vehicles[136] where they can act as highly sensitive detectors and triggers to provide a tunable response to target biomolecules. By understanding these interactions at both the biomacromolecular and interfacial scale, their roles in fundamental biology can be further elucidated and with more rigorous models, their use as tools in diagnostic and therapeutic applications can be further improved.

Experimental techniques such as fluorescence resonance energy transfer[137] and surface plasmon resonance[138] have been used to determine the binding equilibria of biomacromolecules interacting in bulk solution and at an interface, respectively. Bulk and interfacial dissociation constants can be determined with these techniques, but relating them to effective colloidal and surface interactions mediated by their complexes requires alternative methods. Atomic force microscopy (AFM) has been used to sensitively

measure integrin-mediated interactions with fibronectin[139] and E/N-cadherin binding[140] at the surface of cells. Optical force measurement techniques such as total internal reflection microscopy (TIRM) and optical tweezers have been used to measure weak, kT scale interactions between colloids and surfaces mediated by protein-carbohydrate interactions,[70] temperature-sensitive DNA complexation,[63] and actomyosin binding.[54] Colloidal attraction induced by weak, specific biomacromolecular interactions can range from equilibrium interactions to guide colloidal self-assembly using DNA[63] to non-equilibrium irreversible aggregation induced by membrane proteins[66] and peptides.[67]

Predicting effective colloid and surface interactions, either analytically or in simulation, is challenging in these types of systems. Many factors such as surface receptor coverage, receptor-ligand interaction strength and range will have a great impact on the observed attraction strength between the interfaces. Modeling through analytical and simulation techniques have been employed to quantify effective interactions in a number of systems such as DNA mediated colloidal assembly systems[63, 75] and ligand-receptor mediated effective colloid-cell surface interactions for targeted drug delivery,[141, 142] and membrane protein mediated cell adhesion.[143, 144] However, many of these models are specific to the material system of interest and cannot be broadly applied to equilibrium and non-equilibrium effective colloidal and surface interactions mediated by reversible biomacromolecular interactions.

In this work, we develop a computational model of biomacromolecular binding at interfaces and effective colloidal and surface interactions mediated through these receptor-ligand surface interactions. Fig. 5.1 outlines the systematic approach taken to develop this model from the biomacromolecular scale up to the colloidal and interfacial

scale. In order to develop a quantitative model of colloidal and surface interactions driven by biomacromolecules, it is important to establish a solid framework of how specific, reversible biomacromolecules interact in the bulk solution phase, shown in Fig. 5.1A, and at flat and colloidal interfaces, shown in Fig. 5.1B and 5.1*C*, respectively. The receptor-ligand interactions are modeled in this work with a quasiharmonic interaction potential allowing for direct input of each constituent dissociation constant. Bulk equilibrium association and interfacial equilibrium adsorption on colloids and surfaces were determined over a range of interaction strengths and ligand sizes. With biomacromolecular interactions characterized at interfaces, ligand-receptor mediated effective potentials of mean force between colloids as shown in Fig. 5.1D could then be determined using Monte Carlo simulation combined with Umbrella Sampling[105] (MC-US).

Using this model, direct connections can be made to biomacromolecular binding at interfaces to measured equilibrium and non-equilibrium colloidal and surface interactions. Experimental measurements teamed with modeling efforts will allow for a more in-depth and complete description of the role that biomacromolecular interactions at interfaces play in these systems. By developing a model with well-defined, biologically relevant parameters, experimentally determined quantities from AFM (i.e., surface adhesion), TIRM (i.e. colloid-surface interactions), optical tweezers (i.e. colloidal pair potentials), and optical microscopy (i.e., colloidal phase behavior) can be further interpreted to observe the effects of valency, binding affinity, binding lifetimes, and surface receptor density.

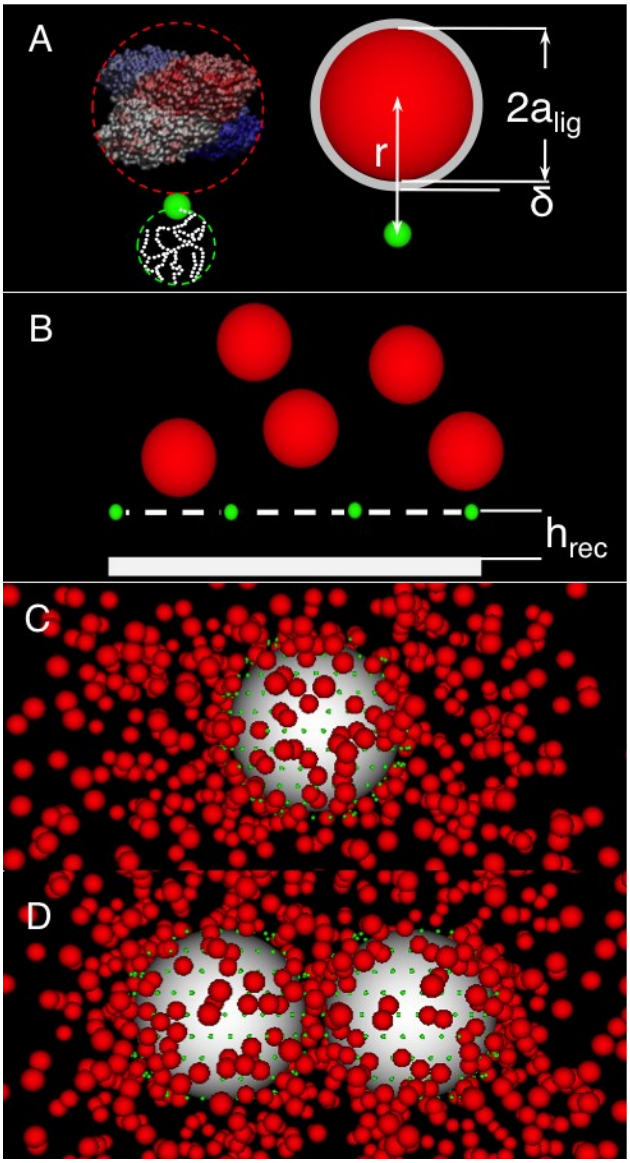

Figure 5.1. Schematics of (*A*) receptor-ligand bulk molecular equilibrium association, (*B*) receptor-ligand surface adsorption, (*C*) receptor-ligand particle surface adsorption, and (*D*) receptor-ligand mediated particle-particle interactions.

5.2 Theory

5.2.1 Theoretical Model

In this work, effective interactions of receptor-functionalized colloids in the presence of freely diffusing ligands will be investigated. A lectin-polysaccharide system

was chosen to demonstrate the utility of this model for real biomacromolecular systems. The lectin Concanavilin A (ConA), shown in Fig. 5.1A, can be approximated as a hard sphere with a well-defined specific interaction with receptors. A 'sticky' hard sphere representation has been used to model protein interactions in crystallization of concentrated solutions[145, 146] and at interfaces during adsorption.[147, 148] The polysaccharide dextran, also shown in Fig. 5.1A, will have a simplified representation. Rather than including a rigorous description of freely-jointed carbohydrate chains, the polysaccharide layers will be represented as interactive sites that have no effective size.

The interactive carbohydrate sites will be immobilized directly above a surface to characterize equilibrium association of ligands at a flat interface as shown in Fig. 5.1B and at a colloidal surface as shown in Fig 5.1C. The simplified polysaccharide representation was decided upon by considering the interactions of the lectins at the interface. The specific adsorption of the lectins to the polysaccharide layers will be dependent on its interactions with carbohydrate subunits at the surface of the polysaccharide layers and lectin bridges formed between the polysaccharide layers will mediate the resulting colloidal interactions. Steric contributions from the polysaccharide layers to the effective colloidal interactions are not crucial in this study of the specific interactions as penetration of the lectins into a polysaccharide layer is unlikely. To study effective colloidal interactions mediated by lectin-carbohydrate interactions, effective potentials of mean force will be determined between 2 carbohydrate receptor-decorated colloidal particles with lectins equilibrated at their surface as shown in Fig. 5.1D.

Although these representations were chosen considering a specific material system, we will show how this approach could be broadly applied to a range of

biomacromolecular systems by presenting a general model for a three-component system consisting of colloids, ligands, and their complimentary receptors. A summary of the interactions of each component in the system is given in Table 5.1. Colloids and ligands are treated as hard spheres with radius a and a_{lig}, respectively. Hard wall interactions exist for colloids interacting with other colloids and ligands in the system. Ligands experience a hard wall interaction with the colloids and surfaces, but have no net interaction with other ligands. The receptors are treated as points in space with no effective size. Receptors will only experience interactions with ligands in this system, and in the next section, these interactions will be defined.

5.2.2 Receptor-Ligand Interaction Potentials

Receptor-ligand interactions are modeled as entropic springs with a monovalent harmonic well potential, U_{RL}. This is an estimate of the free energy between two interacting biomacromolecules averaged over all of the angular and conformational dependencies of their complex. It has been successfully used in molecular dynamics studies of single-well receptor-ligand interactions.[149, 150] U_{RL} is a function of receptor-ligand separation, r, with the form,

$$\begin{aligned} U_{RL}(r) &= \frac{1}{2}k_s r^2 - u_{\min} \qquad \text{if } 0 < r < \delta \\ U_{RL}(r) &= 0 \qquad\qquad\qquad\quad \text{if } r > \delta \end{aligned} \tag{5.1}$$

that has an interaction range, δ, that can be calculated as,

$$\delta = \sqrt{\frac{2u_{\min}}{k_s}} \tag{5.2}$$

which is dependent on the harmonic well depth, u_{min}, and spring constant, k_s. With this potential, neither the ligands nor receptors have an effective size with u_{min} at zero

receptor-ligand separation. The effective size of the biomacromolecules is important to consider in these systems and we will demonstrate how this can be added to their overall interactions.

The ligands of interest in this work (i.e. ConA) will be represented as hard spheres that interact specifically with receptors in the bulk or at an interface. In order to introduce an effective size to the ligands, they can be modeled as hard nanospheres with harmonic well tails. For the receptor-ligand nanosphere potential, U_{RLN}, we use the form,

$$\begin{aligned} U_{RLN}(r) &= \infty && \text{if } r < a_{lig} \\ U_{RLN}(r) &= \frac{1}{2}k_s(r - a_{lig})^2 - u_{\min} && \text{if } a_{lig} < r < a_{lig} + \delta \\ U_{RLN}(r) &= 0 && \text{if } r > a_{lig} + \delta \end{aligned} \tag{5.3}$$

These ligands with an effective size will experience infinite repulsion at ligand-receptor contact that then decays into a harmonic well. It is important to note that these hard spheres with a harmonic well tail will not produce the same binding equilibria of the harmonic well potentials alone. Increasing the effective size at constant k_{s} and $u_{\min}$ also increases the effective ligand-receptor attraction. The goal in this work is to model the specific interactions of biomacromolecules in these systems with well-defined association equilibria and in the next section, we will show how biomacromolecular dissociation constants are calculated.

5.2.3 Predicting Receptor-Ligand Association Equilibria

An analytical expression for the dissociation constant, K_{d}, of a harmonic well potential can be determined using the Bjerrum approach to calculating absolute macromolecular binding free energy developed by Luo and Sharp. For a simple harmonic well potential as in Eq. (5.3), the K_{d} can be calculated with the expression,[100]

$$K_d = \left[(2\pi)^{\frac{3}{2}} \left(\frac{k_s}{kT}\right)^{\frac{-3}{2}} e^{\left(\frac{-u_{\min}}{kT}\right)} \right]^{-1} \tag{5.4}$$

which in short, correlates the Brownian fluctuations in position of the biomacromolecules in their bound state to the biomacromolecules in their unbound state and exponentially decays with increasing well depth. Dissociation constants can be predicted for a wide range of harmonic well potentials. This expression also shows that an infinite set of harmonic well potentials can be created with identical dissociation constants as it is not only dependent on the well depth, but also the range of the interaction. This expression is limited to predictions for harmonic well potentials and an alternative method is required for ligands with an effective size.

Table 5.1 Pairwise interaction potential, U_{ij}, as function of separation, r, for each component in the system.

i \ **j**	**Surface/Colloid**	**Receptor**	**Ligand**
Surface/ Colloid	$U_{ij}(r) = \infty \text{ if } r < 2a$ $U_{ij}(r) = 0 \text{ if } r > 2a$	$U_{ij} = 0$	$U_{ij}(r) = \infty \text{ if } r < (a + a_{lig})$ $U_{ij}(r) = 0 \text{ if } r > (a + a_{lig})$
Receptor	$U_{ij} = 0$	$U_{ij} = 0$	Eq. (5.3)
Ligand	$U_{ij}(r) = \infty \text{ if } r < (a + a_{lig})$ $U_{ij}(r) = 0 \text{ if } r > (a + a_{lig})$	Eq. (5.3)	$U_{ij} = 0$

In order to make dissociation constant predictions for ligands with an effective size, the second virial coefficient, B_2, is calculated for the ligand nanospheres to estimate their effective interaction strength. The second virial coefficient for the ligand nanosphere, $B_{2,\text{RLN}}$, is calculated with the following expression,

$$B_{2,RLN} = 4V + 12 \int_{a_{lig}}^{a_{lig}+\delta} r^2 (1 - e^{(\frac{-U_{RLN}(r)}{kT})}) dr \tag{5.5}$$

The first term is the hard sphere component of $B_{2,\mathrm{RLN}}$ that is simply four times its volume, V. The second term accounts for the harmonic well tail component of $B_{2,\mathrm{RLN}}$ and this is calculated using an expression which can be applied to any arbitrary potential to determine B_2. [101] An equivalent harmonic well potential is then found by determining a harmonic well with the same B_2 as the ligand nanosphere potential. The second virial coefficient of a harmonic well potential, $B_{2,\mathrm{RL}}$, is calculated as,

$$B_{2,RL} = 12 \int_{0}^{\delta} r^2 (1 - e^{(\frac{-U_{RL}(r)}{kT})}) dr \tag{5.6}$$

using the same expression to determine B_2 for any arbitrary potential. To find an equivalent harmonic well potential, u_{min} in Eq. (5.4) for U_{RL} is adjusted at constant k_{s} until $B_{2,\mathrm{RL}}$ is equal to $B_{2,\mathrm{RLN}}$ of the ligand nanosphere potential. These two potentials are then considered equivalent and the K_{d} of the harmonic well calculated from Eq (5.4) is assigned to the ligand nanosphere.

With these dissociation constants determined, adsorption equilibria at an interface can also be predicted. Since the receptor-ligand interactions in our model are monovalent, the Langmuir adsorption model can be used to predict adsorption equilibria at an interface with the expression,

$$\theta = \frac{K_d^{-1} C}{1 + K_d^{-1} C} \tag{5.7}$$

which determines the fraction of occupied receptors, θ, as a function of bulk ligand concentration, C. The adsorption coefficient for this system is the inverse of K_{d} (i.e., the association constant, K_{a}). Using the combined Bjerrum-B_2 approach to predict K_{d}, the

equilibrium interactions of receptors and ligands of varied size can also be predicted at interfaces.

5.3 Methods

5.3.1 Simulations of Bulk and Interfacial Equilibrium Interactions

MC simulations of bulk equilibrium association (MC-EA) were used to determine the dissociation constant of a receptor and a ligand with harmonic well interactions. All fixed parameters used in each simulation set are presented in Table 5.2. In all simulations, a fixed spring constant, k_s was used and δ of each harmonic well was calculated with Eq. (5.2). as a function of U_{min}. For each case, periodic boundary conditions were used to maintain a constant bulk ligand and receptor concentration of $0.1K_d$ determined with Eq. (5.4) The receptors and ligands are considered to be in their bound state if $r < (a_{lig} + \delta)$. The dissociation constant was calculated from the concentration of unbound receptors, $[R]$, unbound ligands, $[L]$, and receptor-ligand complexes, ($[RL]$) as

$$K_d = \frac{\sum_{i=1}^{n} [RL]_i}{\sum_{i=1}^{n} [R]_i \sum_{i=1}^{n} [L]_i} \tag{5.8}$$

which averages over the n configurations generated.

MC simulations of biomacromolecular surface adsorption (MC-SA) were used to determine the Langmuir isotherms of freely diffusing ligands interacting with surface immobilized receptors. Receptor sites with a uniform spacing of L_R were immobilized at height h_{rec} above a surface with area S_A. A bulk ligand concentration is maintained in a

Table 5.2 Fixed parameters used in MC bulk equilibrium association simulations (MC-EA), MC surface adsorption simulations (MC-SA), MC colloidal surface adsorption

simulations (MC-CSA), and MC umbrella sampling (MC-US) simulations. The variables correspond to the following quantities starting from the first row: maximum step size in ligand radii for MC-EA and MC-SA and in particle radii for MC-CSA and MC-US; maximum rotation distance in particle radii; spring constant; bulk ligand concentration; number of ligands; number of receptors; particle radius; planar surface area for MC-SA and colloidal surface area for MC-CSA and MC-US; aspect ratio of box; lateral receptor spacing; volume of cell; and height of box. Dashes indicate the parameter was varied throughout or not applicable in that particular simulation set.

	MC-EA	**MC-SA**	**MC-CSA**	**MC-US**
n	2×10^6	2×10^6	2×10^6	2×10^6
s (radii)	0.01	0.01	0.01	0.01
s_{rot} (radii)	-	-	0.0001	0.0001
k_s (pN/nm)	7	7	7	7
C (μM)	$0.01K_d$ from Eq. (5.4)	10	10	-
N_{lig}	1	100	568	867
N_{rec}	1	16	-	-
a (nm)	-	-	100	100
h_{rec} (nm)	-	$a_{lig} + \delta$ from Eq. (5.2)	$a_{lig} + \delta$ from Eq. (5.2)	$a_{lig} + \delta$ from Eq. (5.2)
S_A (μm^2)	-	0.075	0.126	0.252
AR	1	1	1	1
L_R (nm)	-	68	30	30
V_{cell} (μm^3)	-	0.017	0.094	-
H (nm)	-	221	455	-

box with periodic boundary conditions in the x and y directions and a fixed height, H. As in the bulk molecular adsorption MC simulations, the concentrations of each component and their complexes are tracked and the fraction of occupied receptors are calculated with

the equation,

$$\theta = \frac{\sum_{i=1}^{n} [RL]_i}{\sum_{i=1}^{n} [R]_i} \tag{5.9}$$

averaged over n configurations.

MC simulations of biomacromolecular colloidal surface adsorption (MC-CSA) were used to determine Langmuir isotherms of freely diffusing ligands at a receptor-functionalized colloidal surface. In these simulations, a colloid with radius a is placed in a box with periodic boundaries in all directions to maintain a bulk ligand concentration of C. Receptors are uniformly placed on the surface of the colloid with L_R of $1.5a_{lig}$ and surface-receptor spacing of h_{rec} above the colloidal surface. The number of receptors on the colloidal particles, N_{rec}, varied from 225-236 depending upon a_{lig} and δ in each case. In these simulations, colloids make 2D translational moves in the x- and y-direction and ligands are allowed to make 3D translational moves. In order to prevent dynamic arrest of a ligand-coated colloid, translational colloid-ligand cluster moves are made for all ligands bound to receptors. The colloids also perform 3D rotational receptor moves to sample alternative receptor configurations. The procedures for performing 3D rotational receptor moves and colloid-ligand cluster moves are explained in detail in *Chapter 3*. The fraction of occupied receptors was calculated with Eq. (5.9).

5.3.2 Umbrella Sampling Simulations

MC-US simulations were used to determine the potentials of mean force between 2 receptor-functionalized colloids in the presence of ligand nanospheres. Umbrella sampling has been used to construct free energy landscapes in biomolecular systems[151]

and colloidal systems[152, 153] and there are a number of references that discuss this technique in detail.[105, 154] In these simulations, translational moves by the colloids are restricted to one dimension in the *x*-direction and the ligands are allowed to translate in 3D. 3D rotational receptor moves and colloid-ligand cluster moves (described in *Chapter 3*) are also employed to ensure the colloids are diffusing freely and able to sample many configurations.

To perform MC-US simulations, a hard wall biasing potential is introduced to restrict parameters to regions of interest. The hard-wall biasing potential used in this work was applied to the surface-to-surface separation between the colloids, L, with all MC moves outside of the specified bounds for L rejected. Using the hard wall biasing potential, particles can be placed in energetically unfavorable portions of the potential of mean force that allows us to avoid sampling issues. Twelve simulations with L constrained to bins of 5 nm widths were performed for each case. The bins each simulation probes are sequentially chosen to cover a range of L from 10-48 nm with adjacent bins overlapping in 2 nm regions. These overlapping regions allow us to connect adjacent bins for the construction of potentials of mean force, W as a function of L. All potentials take a reference free energy as what is found at L = 48 nm in each case. At a separation of L = 48 nm, the ligand nanospheres are unable to form bridges between colloids in all cases. In addition to W, the average number of bridges, $\langle N_{\text{bridge}} \rangle$ and histograms of bridge energy, U_{bridge}, and bridge orientation with respect to the colloids, ϕ, were determined.

5.4 Results and Discussion

5.4.1 Bulk Equilibrium Association of Biomacromolecules

In order to characterize interactions between freely diffusing biomacromolecules, MC-EA simulations were carried out to determine the K_d for ligand nanospheres and receptors diffusing in bulk solution as a function of u_{min} and $a_{lig.}$ To carry out these simulations, one ligand and one receptor are placed in a box and binding events between the ligand and receptor can be monitored which we illustrate in Fig. 5.2A-C with a linear color scale for the ligand nanosphere that goes from white when $U_{RL} = 0$ (i.e., when the ligand is ubound) to red when $U_{RL} = -u_{min}$ (i.e., when the ligand is tightly bound). By studying these ligand-receptor pairs, we can monitor binding events over a statistically significant amount of configurations as shown in Fig. 5.2D with minimal computational expense. We can then obtain the cumulative average concentration of each species in the system as shown in Fig. 5.2E. With these concentrations, K_d can be calculated using Eq. (5.8) and Fig. 5.2F shows how the value of K_d converges once a sufficient sampling of binding events have been collected.

This technique was used to study K_d as a function of u_{min} and a_{lig}. The results are shown in Fig. 5.2G where wide ranges of K_d over 8 orders of magnitude were investigated. The lines in Fig. 5.2G represent our theoretical predictions based on Eq. (5.4) for harmonic wells combined with comparisons of B_2 calculated with Eq. (5.5) and Eq. (5.6). A bulk ligand and receptor concentration of $0.1K_d$ calculated from Eq. (5.4) was used in each case to ensure that many binding and unbinding events could be observed which led to more accurate determinations of K_d. Agreement is seen between

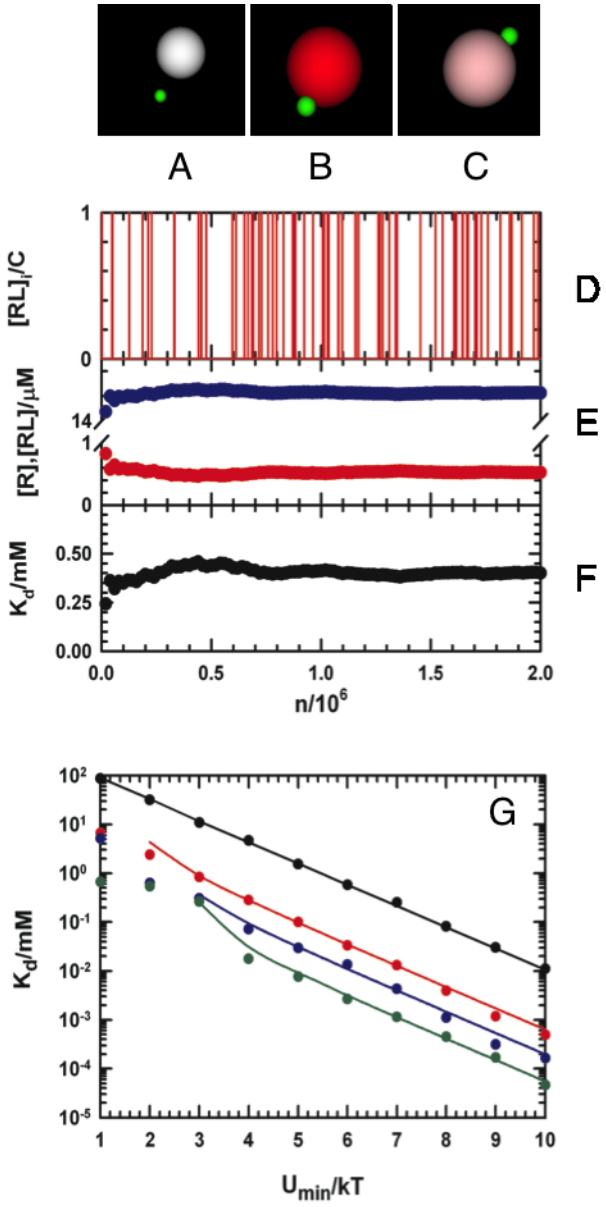

Figure 5.2. (*A-C*) Snapshots of a ligand and receptor interacting in MC-EB simulations where ligands have a linear color scale from white when $U_{RL} = 0$ to red when $U_{RL} = umin$. (*D*) $[RL]_i$, (*E*) [R] and [RL], and (*F*) K_d are shown as a function of *n*. (*G*) K_d for a_{lig} = 0 nm (black), 2.5 nm (red), 5 nm (blue), and 10 nm (green) is shown as function of *umin* where solid lines represent theoretical predictions of K_d and solid circles were obtained from MC-EA simulations.

the K_d observed in simulation and theoretical predictions made using Eq. (5.4). We also observe a systematic decrease in K_d as the effective size of the ligand nanosphere increases at fixed u_{min}. This decrease in K_d arises from an effective increase in ligand-receptor attraction due to the increase in ligand nanosphere surface area. The second virial coefficient allows us to determine how much this effective ligand-receptor attraction changes as a function of u_{min} and a_{lig} by equating ligand nanospheres to ligand-harmonic well potentials with equal B_2.

5.4.2 Specific Adsorption of Ligands at Interfaces

With receptor-ligand interactions characterized in the bulk phase, next we were interested in studying these same interactions at an interface. We began first by determining surface adsorption equilibria of ligand nanospheres at a receptor-functionalized flat surface in MC simulations as is shown in Fig. 5.3A and 5.3B. Surface adsorption equilibria were then determined on a receptor-functionalized colloid which is illustrated in Fig. 5.3C and 5.3D. The same ligand energy coloring scheme presented in Fig 5.2A-C is used to more clearly show surface bound ligands and ligands diffusing in the bulk. Using a strategy similar to that used in the bulk phase, we can determine the equilibrium surface coverage, θ, with the average concentrations of unbound receptors, [R], and occupied receptors, [RL].

Figure 5.3E shows theoretical and simulation results of Langmuir isotherms for ligand nanospheres as a function of u_{min} and a_{lig} on flat surfaces and colloids. The theoretical Langmuir fitting is done with Eq. (5.7) where K_d^{-1} is calculated using the Bjerrum-B_2 approach. There is excellent agreement between the theoretical predictions for surface coverage K_d^{-1} as the adsorption coefficient and what was found in our

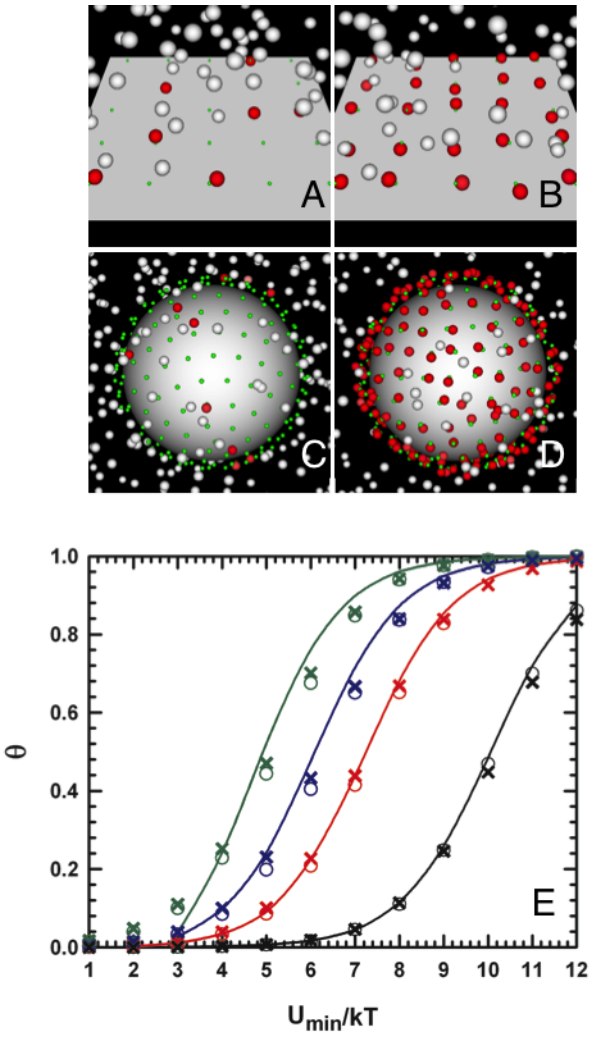

Figure 5.3. Snapshots of MC-SA simulations at C = 10 μM and (*A*) u_{min}= 3 *kT* and (*B*) 9 *kT* where ligands have a linear color scale from white when U_{RL} = 0 to red when U_{RL} = u_{min}. Snapshots of MC-CSA simulations at C = 10 μM, (*A*) u_{min}= 3 *kT* and (*B*) u_{min}= 9 *kT* where ligands have a linear color scale from white when U_{RL} = 0 to red when U_{RL} = u_{min}. (*E*) Langmuir isotherms from u_{min}= 1 - 12 *kT* with C = 10 μM and a_{lig} = 0 nm (black), 2.5 nm (red), 5 nm (blue), and 10 nm (green). Solid lines represent theoretical predictions of θ. Open circles were obtained from MC-SA simulations and x's obtained from MC-CSA simulations.

simulations for the flat interface shown as open circles in Fig. 5.3E. These results also show the effect of increasing ligand size as the surface coverage increases due the increase in surface area of the ligand nanosphere. It is important to highlight the effect of receptor placement at the flat interface. In order to prevent steric hindrance between the ligand nanospheres and the surface, the receptors are placed at h_{rec} of (a_{lig} + δ) nm above

the surface as is depicted in Fig. 5.1B and these effects were observed in preliminary results when the receptors were placed at distances less than ($a_{lig} + \delta$).

This model for our receptor-functionalized interface was then extended to a diffusing colloid. Figure 5.3E also shows results as x's for the surface coverage as a function of u_{min} and a_{lig} on a colloid with radius a functionalized with receptors on it's surface. We also see great agreement with the theoretical predictions for the surface adsorption equilibria on a diffusing colloid. With the determination of colloidal potentials of mean force based on the receptor-ligand interactions in sight, it was important at this stage to determine an appropriate algorithm in these MC simulations that allows for translation and rotation of the colloid with dense coverages of ligand nanospheres without interfering with appropriate surface equilibria at different conditions.

With the typical Metropolis MC simulation scheme, MC move efficiency becomes a major concern in modeling of multi-component systems like binary colloidal mixtures [155] or colloid-polymer systems [156] and for these cases, a number of cluster move schemes have been developed.[103] This strategy was employed for our binary colloid-ligand nanosphere system. All ligands associated to a colloid's receptors can be quickly identified and a MC cluster move based on the change in energy for the colloid and all associated ligand nanospheres can be made. By accounting for the change in energy for all molecules involved in the cluster move, we avoid disruption of the surface equilibria at the interface by attempting these cluster moves. More details on this algorithm and the efficiency of these moves are presented in *Chapter 3*. With this algorithm, we were prepared to study colloidal interactions mediated by ligands adsorbed to their surface and in the next section, we will show how we quantify these effective colloidal interactions

for a model protein-carbohydrate system.

5.4.3 Potentials of Mean Force Mediated by Receptor-Ligand Interactions

With these ligand-receptor interactions characterized at colloidal interfaces, the interactions between colloids with ligands equilibrated at their receptor-functionalized surfaces could then be investigated. To illustrate how this model could be used for specific material systems, we chose a parameter space directly applicable to weak, specific interactions between the lectin, ConA and the polysachharide, dextran. This system has been the focus of many experimental studies of ConA-dextran mediated colloidal interactions.[70, 157, 158, 159, 160] The dissociation constant for ConA and dextran has been reported from 0.1-1 μM.[161, 162] ConA are represented as a ligand nanospheres with a_{lig} = 5 nm and u_{min} = 9 kT (corresponding to K_d = 0.536 μM) to interact specifically with dextran receptors (i.e. glucose subunits) on the colloidal surfaces.

To probe the effects of freely diffusing ConA on dextran-decorated colloids, we first studied the effects of ConA concentration, [C], on effective colloidal interactions. Representative snapshots at L = 15 nm and varied [C] are shown in Fig. 5.4A-D with a slight change in ligand energy coloring scheme that now will range from white when U_{RL} = 0 to red when $U_{RL} = 2u_{min}$ to clearly show freely diffusing (white), surface adsorbed (light red), and bridging ligand nanospheres (red). By changing concentration, the density of ConA adsorbed on the dextran-decorated surface can vary from very high to low coverage. In this range of [C], the fraction of occupied receptors varies from 0.02 at [C] = 0.01 μM, shown in Fig. 5.4A, up to 0.86 at [C] = 10 μM, shown in Fig. 5.4D. Changing concentrations of ConA bound to the colloidal surfaces will also lead to changes in the number of ConA bridges formed (i.e., red nanospheres in Fig. 5.4A-D) that will mediate

the effective colloidal attraction.

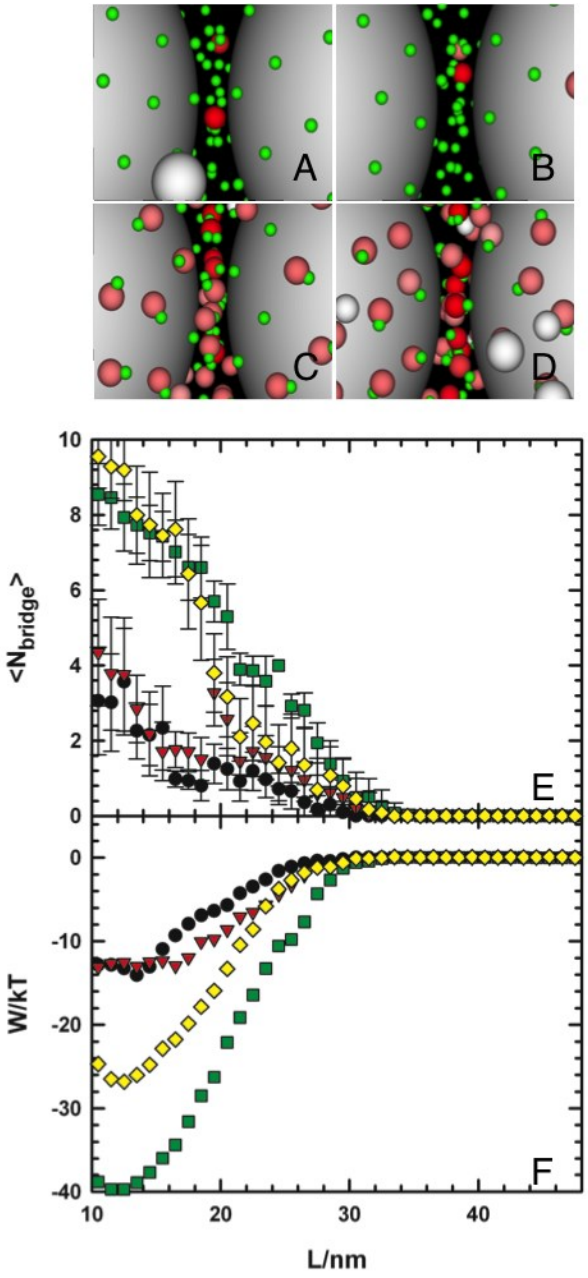

Figure 5.4. Snapshots of MC-US simulations at u_{min}= 9 *kT* and (*A*) [*C*]= 0.01 μM ,(*B*) 0.1 μM, (*C*) 1 μM, and (*D*) 10 μM where ligands have a linear color scale from white when U_{RL} = 0 to red when U_{RL} = 2u_{min}. (*E*) ⟨N_{bridge}⟩and (*F*) *W* versus *L* for u_{min}= 9 *kT* and [*C*]= 0.01 μM (circles), 0.1 μM (triangles down), 1 μM (squares), and 10 μM (diamonds).

In Fig. 5.4E and 5.4F, potentials of mean force, *W,* and the average number of bridges, $\langle N_{bridge} \rangle$, as a function of separation, *L*, are shown at $u_{min} = 9\ kT$ and varied [*C*]. Although the number of bridges formed is continually fluctuating, $\langle N_{bridge} \rangle$ is an informative quantity in this system where effective colloidal attraction is induced by biomacromolecular bridges between the colloidal interfaces. At [*C*] = 10 μM (diamonds), ensembles of up to 10 ConA bridges form between the colloidal interfaces and induce a strong effective colloidal attraction. When the concentration is lowered to [*C*] = 1 μM (squares), the effective colloidal attraction increases even further. The bridging profiles at [*C*] = 10 μM and 1 μM look very similar until *L* is between 20 and 30 nm where the number of bridges increases at [*C*] = 1 μM. This can be explained by the difference in the amount of adsorbed ConA to each colloidal surface where a lower surface coverage leaves more receptors available for bridge formation. When the concentration is further lowered to 0.1 μM (triangles down) and 0.01 μM (circles), the fraction of occupied dextran receptors drops dramatically which leads to a decrease in both the number of bridges formed and effective colloidal attraction.

It has also been shown experimentally that the addition of monosaccharide inhibitors like glucose or mannose can weaken the net ConA-dextran mediated attraction between colloids.[70, 159, 160] In this model, the inhibitory effect due to competitive binding of monosaccharides was introduced as a change in the affinity of ConA for the dextran receptors on the colloids. By decreasing u_{min} (i.e., increasing the K_d), we can introduce this weakening of the ConA-dextran interactions due to ConA sites being occupied by monosaccharides. . Representative snapshots at *L* = 15 nm and varied u_{min} are shown in

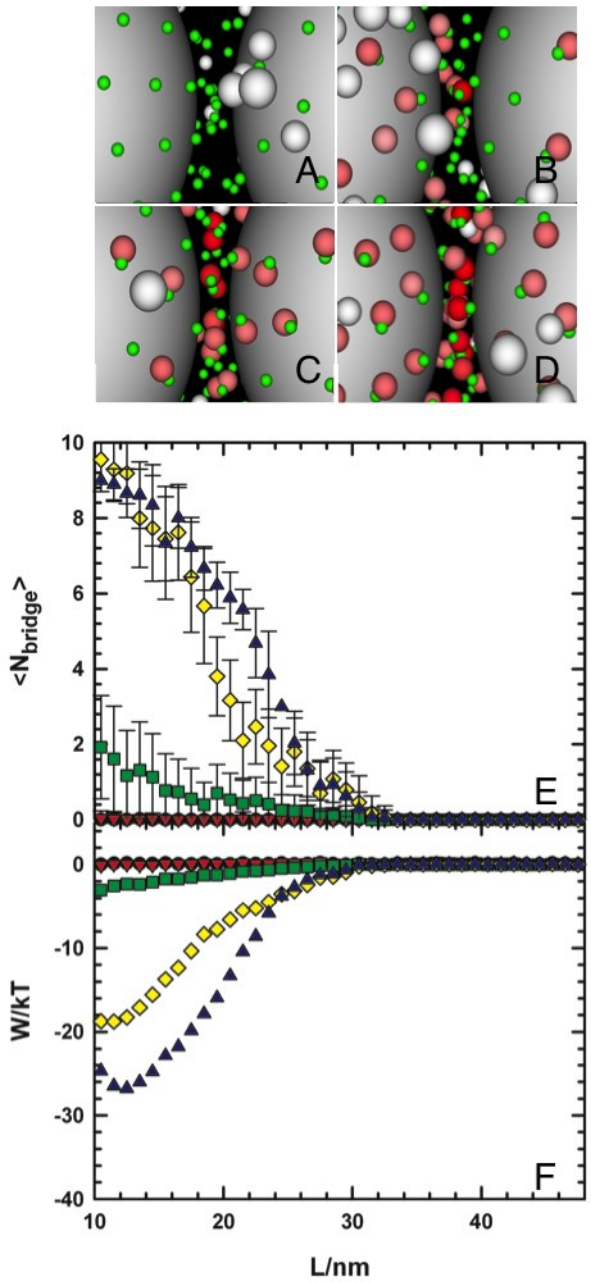

Figure 5.5. Snapshots of MC-US simulations at L = 15 nm, [C]= 10 μM , and (A) u_{min}= 3 kT , (B) u_{min}= 5 kT, (C) u_{min}= 7 kT and (D) u_{min}= 9 kT where ligands have a linear color scale from white when U_{RL} = 0 to red when U_{RL} = 2u_{min}. (E) $\langle N_{bridge} \rangle$ and (F) W versus L for [C] = 10 μM and u_{min}= 1 kT (circles), u_{min}= 3 kT (triangles down), u_{min}= 5 kT (squares), u_{min}= 7 kT (diamonds), and u_{min} = 9 kT.

Fig. 5.5A-D which illustrate how changing u_{min} at a fixed [C] leads to changes in surface coverage of ConA and this will also lead to changes in the number and relative strength of each bridge formed which will, in turn, change the effective colloidal

interactions.

In Fig. 5.5E and 5.5F, W and $\langle N_{bridge} \rangle$as a function of L are shown at [C]= 10 μM and varied u_{min}. When u_{min} is lowered from 9 kT (triangles up) to 7 kT (diamonds), W is weakened and $\langle N_{bridge} \rangle$ slightly falls, but the resulting effective attraction would still result in strong, irreversible attraction between the colloids. When the specific interaction between ConA and dextran is further weakend to 5 kT (squares), there is a large decrease in the number of bridges formed which results in a further weakening of W into a weaker, reversible regime. This sharp transition from strong, irreversible effective attraction to weak, reversible effective attraction has been seen in experimental studies of this system [70] and also in computational studies of similar biomacromolecular systems.[163] If u_{min} is weakened further to 1 kT (circles) and 3 kT (triangles down), only occasionally do bridges form and no net colloidal attraction is induced.

5.4.4 Energy and Orientation of Ligand Bridges

The effective potentials that we have determined for a model lectin-carbohydrate system clearly show how colloidal potentials can be mediated through their interactions. With receptors immobilized on the colloidal surfaces, freely diffusing ligands can adsorb to their surface and create attractive bridges. Figures 5.4 and 5.5 show that effective colloidal potentials can be changed as function of C, to change the equilibrium ligand surface coverage, θ, and ligand-receptor potential well depth, u_{min}, to vary the strength of each bridge formed between the colloidal particles. The strength of effective colloidal attraction generated by these bridges will not only be dependent on the number of bridges and their energies, but also the orientation of the bridges with respect to the colloidal

surfaces will play a role in the effective colloidal interactions. In Fig. 5.6A-D, the progression of the number of bridges and bridge orientation as a function of L is shown visually for a representative ConA-dextran case at $u_{min} = 9\ kT$ and $[C]= 10\ \mu M$. When L = 10 nm as is shown in Fig. 5.6A, the highest number of bridges are able to form due to the proximity of the receptor layers. However, the majority of the bridges formed at this separation are not oriented normal to the colloidal surfaces and will not be able to exert a great amount of attractive force in that direction. When the colloids are further separated at L = 20 nm as is shown in Fig. 5.6B, the number bridges formed decreases, but we begin to see bridges with orientations closer to normal to each surface. When L = 30 nm as is shown in Fig. 5.6C, one bridge is present centrally between the particles and it must take a normal orientation in order to interact with a receptor on each particle. If separated even further, the colloids move beyond the range from which ligands can form bridges and this is shown in Fig. 5.6D at L = 40 nm. These clearly illustrate that the number of bridges along with the orientation of each bridge is highly dependent on the separation between the colloids.

To more quantitatively examine these effects, histograms of the bridge energy, U_{bridge}, is shown in Fig. 5.6E as function of L. In Fig. 5.6E, a histogram of U_{bridge} as a function of L, $\rho(L, U_{bridge})$, is shown where it is also normalized by $\rho(L)$ to show the relative frequency of bridge energies at each separation. At shorter separations where $L <$ 20 nm, the receptor layers on opposite colloids are interpenetrating (h_{rec} = 8.25 nm), shown in Fig. 5.6A, which allows for very strong bridges to form with U_{bridge} ranging from $1.8 - 2u_{min}$. As the colloids are further separated to $L >$ 30 nm, the ligands are unable to have short range interactions with a receptor on each of the colloids and this

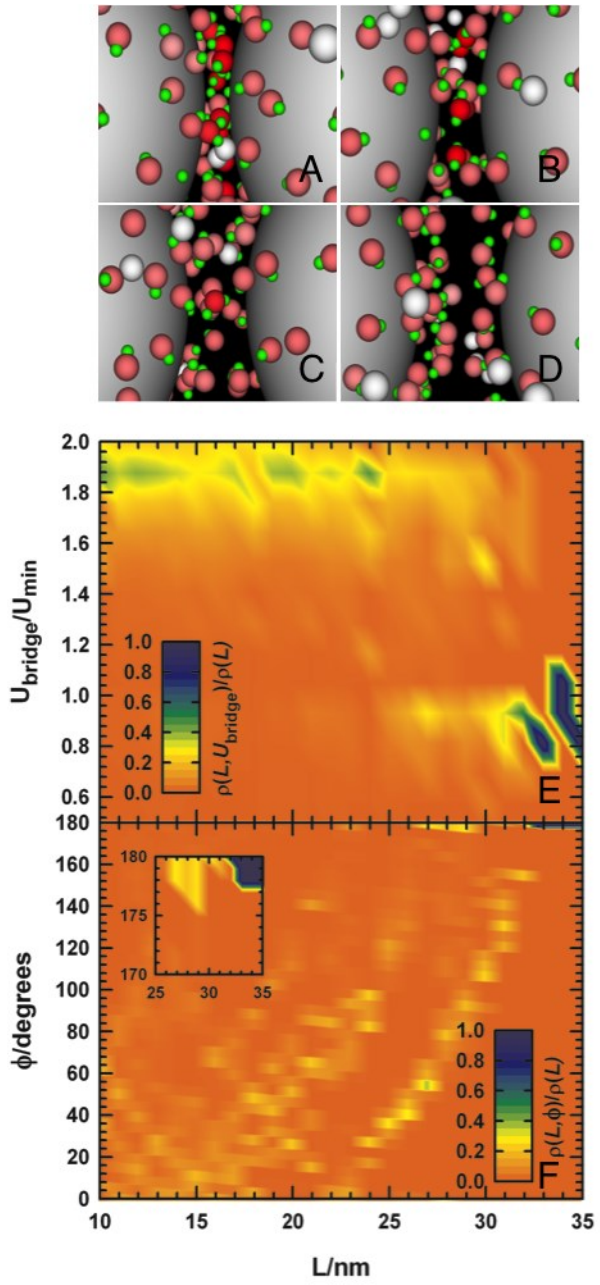

Figure 5.6. Snapshots of MC-US simulations at [*C*] = 10 μM, u_{min}= 9 *kT*, and (*A*) *L* = 10 nm, (*B*) 20 nm, (*C*) 30 nm and (*D*) 40 nm where ligands have a linear color scale from white when U_{RL} = 0 to red when U_{RL} = 2u_{min}. 2D histograms of (*E*) U_{bridge} and (*F*) ϕ as a function of *L* at [*C*]= 10 μM and u_{min} = 9 *kT* with a linear color scale from 0 to 1 of frequency ρ(*L*, U_{bridge}) and ρ(*L*, ϕ), respectively, normalized by total frequency $\rho(L)$.

leads to a weakening of the bridges with U_{bridge} ranging from 1.0 – 1.2u_{min}. If we were to take the sum of the energies of each bridge to calculate the expected attraction between

the colloids, we would obtain effective colloidal attractive well depths of ~160-180 kT rather than the ~19 kT well depth found in the MC-US simulation results for this case shown in Fig. 5.5F. Clearly, these effective colloidal interactions cannot be explained simply as an ensemble average of the bridge energies.

To further examine bridge orientation, histograms of orientation with respect to the colloidal surfaces, ϕ, is shown in Fig. 5.6F as function of L. The bridges can take a range of orientations between the colloidal particles from parallel to the surfaces (i.e., ϕ = 0º) to normal to the surfaces (i.e., ϕ = 180º). Only forces exerted normal to the colloidal surfaces by these bridges will generate effective colloidal attraction and this will be dependent on the orientation of the bridges. When L < 15 nm, the bridges have mostly acute orientations to the surfaces with ϕ ranging from 0-40º and In Fig. 5.6A, the representative snapshot at L = 10 nm shows that the close proximity of receptor layers forces the majority of bridges (red spheres) to take these orientations. As the colloids separate further from L = 20 – 30 nm, bridges begin to sample higher ϕ up to 120º and bridges will be able to exert a greater amount of force normal to each surface as the snapshot at L = 20 nm in Fig. 6 *B* illustrates. It is not until L > 30 nm where we begin to see a high sampling of bridges with orientations normal to the surface (ϕ = 180º) and in Fig. 5.6*C*, a representative snapshot at L = 30 nm shows a bridge form centrally between the colloids with an orientation normal to both surfaces.

The results in Fig. 5.6 demonstrate how the interplay of multiple parameters leads to the observed effective colloidal interactions and we can begin to provide a more intuitive and physical interpretation of the simulation results we have obtained. The effective colloidal attraction will not only be dependent on the number and overall energy

of ligand bridges, but also their orientation to the surfaces. Bridges that form parallel with respect to the particle surfaces will not generate the same amount of attraction as those normal to the surfaces. Depending on their position between the colloids, they could also sterically hinder attraction between the surfaces as can be seen in Fig. 5.6A where they lie in close proximity to both colloidal surfaces. Bridges that are normal to both surfaces will generate the greatest amount of colloidal attraction, but this orientation only becomes likely as L approaches the maximum bridge length where consequently U_{bridge} decreases. It is clear that these quantities do not work independently to change W and using this model, we can investigate how they are interconnected. Future work will aim to develop an analytical model that uses key parameters such as u_{min}, θ, U_{bridge}, and ϕ to determine what net effect each bridge has on the effective colloidal potentials.

5.5 Conclusions

This work provides a model of receptor-ligand mediated colloidal potentials of mean force with a range of input parameters such as K_{d}, ligand size, ligand concentration, and receptor coverage. MC simulations of receptors and ligand nanospheres interacting in the bulk phase and interfaces allowed us to probe the effects of ligand size and interaction well depth. Developing a formalism starting at the biomacromolecular level for determining K_{d} between receptors and ligand nanospheres was crucial in the determination of interactions between colloids mediated by these biomacromolecules. With the dissociation constant and ligand size as inputs, colloidal potentials of mean force could then be determined with MC umbrella sampling and cluster move techniques that allowed for efficient configurational sampling in this three-component system. Using this technique, colloidal interactions were determined for a model lectin-polysaccharide

system to demonstrate how this approach could be applied to real systems. As a result of the presence of the freely diffusing ConA nanospheres, net attraction could be generated between dextran-decorated colloids by ensembles of ConA-dextran bridges. The coverage of ConA, dependent on [C] and K_d, and the relative lifetimes or strength of each ConA-dextran bridge, dependent on $u_{\min}$, clearly mediate the resulting net colloidal attraction. This provides a versatile model that could be applicable to a range of material systems and applications with biological relevance. Future work will look to make direct comparisons of the results from this work to experimentally determined equilibrium colloidal interactions mediated by ConA-dextran binding. These modeling approaches will also be extended to colloid-surface interactions to study biomacromolecular interactions relevant to biosensing and targeted drug delivery applications.

6. DIFFUSING COLLOIDAL PROBES OF CELL SURFACES

6.1 Introduction

In the development of innovative biotechnologies, precise design of biomaterials (i.e targeted nanoparticle drug carriers, biosensors, biocompatible tissue scaffolds) is required to optimize interactions at the surface of cells and tissues for robust response to biomolecular and biophysical cues.[164, 165] While a number of synthetic and biological materials have proven useful in biomedical applications, a fundamental understanding of their interactions with live biological interfaces will aid in more efficient design and implementation in new therapeutic and diagnostic tools. To develop models to describe the interactions in these complex biological systems, highly sensitive, quantitative measurements are needed capable of directly interrogating the surface of cells and tissues.

Spectroscopic techniques such as surface plasmon resonance (SPR) and total internal reflection microscopy (TIRFM) can be used to measure the distribution of biomacromolecules at interfaces between cells and polymer, protein, and carbohydrate functionalized substrates.[35, 166, 167, 168, 169, 170, 171] However, the interactions between these biomaterials and cells can only be inferred from local changes in concentration of membrane-associated biomolecules (i.e. membrane protein clustering, actin stress fibers) and cell morphology (i.e. cell spreading, focal adhesions). Atomic force microscopy (AFM) has been used to directly measure interactions of cells with biofunctionalized colloids and substrates. [41, 44, 51, 55, 125, 140] The deflection of a mechanical cantilever in contact with surface of the cell is used to measure interfacial interactions and can also be used to determine the topography of cells and tissues. However, the sensitivity of this

technique is limited by the spring constant of the cantilever to forces greater than ~1 pN. Direct, quantitative measurements capable of resolving weak, biomacromolecular interactions with single molecule resolution require more sensitive measurement techniques.

Diffusing colloidal probe microscopy (DCPM) is the technique most closely related to the results in this work where measurements of interfacial interactions are determined from the trajectories of freely diffusing colloidal particles bearing adsorbed or grafted macromolecules near macromolecule-coated surfaces. This technique has been used to characterize nonspecific polymer-protein, supported lipid bilayer, specific protein-carbohydrate and specific protein-protein interactions.[71, 72, 127, 172] With no external manipulation, force measurements can be made with *kT*-scale sensitivity in a direct, statistically significant manner. In this work, the analytical and interpretative tools developed in these studies are extended to colloidal interactions with live cell surfaces. A diverse group of synthetic and biological macromolecules, all with relevance to bioengineering, were studied to demonstrate the utility of this method for a wide range of material systems. Direct measurements of nonspecific interactions between live cell surfaces and polyethylene glycol (PEG), bovine serum albumin (BSA), and dextran as well as specific interactions between live cells and hyaluronic acid (HA), a glycosoaminoglycan found in the extracellular matrix, were measured using a suite of image analysis tools to extract dynamic and equilibrium particle-cell surface interactions.

Dark field video microscopy is used for label-free imaging of colloids and live cells. Image analysis techniques capable of automated detection of colloids and cell surfaces allow for real-time, 2D multi-particle and multi-cell tracking. By using micron-

sized colloidal probes above the minimum size required for passive or active uptake into the cell,[18, 173, 174] our study can focus solely on the transport of particles approaching the cell and their interactions with the cell surface. Dynamic and equilibrium analyses of individual and ensembles of colloidal trajectories off the cell (i.e. on background substrate) and on the cell are used to determine mean squared displacement, particle cell-surface association lifetimes, and particle-cell surface interaction potentials. With the particle diffusion and net interactions well understood between synthetic and biological macromolecular layers from prior studies,[71, 72, 106, 172, 175] measurements on the background substrate can be used for comparison to the much more complex, multi-faceted interactions measured for particles on the cell surface.

6.2 Theory

6.2.1 Interaction Potentials

For a macromolecule-coated colloidal particle diffusing over a macromolecule-coated surface or cell surface at physiological ionic strength, the net particle-surface interaction potential is given by,

$$u_{ps}(h) = u_G^{pf}(h) + u_V^{ps}(h) + u_S^{ps}(h) + u_B^{ps}(h) \tag{6.1}$$

where the subscripts refer to gravitational (G), van der Waals (V), steric (S), and specific biomacromolecular (B) interactions and the superscripts refer to particle-field (pf) and particle-surface interactions (ps). The gravitational potential energy of each particle is dependent upon its height above the surface, h, and its buoyant mass, m, as,

$$u_G^{pf}(h) = mgh = \frac{4}{3}\pi a^3(\rho_p - \rho_f)gh \tag{6.2}$$

where g is the acceleration due to gravity, a is the particle radius, ρ_p is the particle density, and ρ_p is the fluid density. van der Waals attraction between two flat plates can be predicted by Lifshitz theory[79] with retardation and screening effects and using the Derjaugin approximation to account for geometric effects.[80] For simplicity, an inverse power law approximation can be used to model van der Waals interactions between a particle and a wall given by,[80, 111]

$$u_V^{ps}(h) = -aA_{ps}h^p \tag{6.3}$$

where A_{ps} is an effective Hamaker constant appropriate over a short range (h < 15 nm) and p is a noninteger power. The fitting constants A_{ps} and p can be adjusted depending upon the dielectric properties of the materials. Repulsive steric interactions will occur at the interface between the particle and surface due to compression of macromolecules at their interfaces and this can be modeled with a short range exponential given by,

$$u_S^{ps}(h) = \Gamma \exp(-\kappa h) \tag{6.4}$$

where Γ and κ are determined by the structure of the macromolecular layers. To model particle-surface interactions mediated by specific biomacromolecular interactions between a particle and a surface (i.e particle surface-immobilized ligands binding to membrane protein receptors), an isotropic harmonic well attractive potential can be added with the form[87],

$$u_B^{ps}(h) = u_{\min}\left(\frac{h - h_{\min}}{h_{\min}}\right)^2 \tag{6.5}$$

where $u_{\min}$ is the depth of the harmonic well and $r_{\min}$ is the position of the harmonic potential well minimum.

6.2.2 Hydrodynamic Interactions

A colloidal particle near a planar substrate will experience hydrodynamic interactions that will hinder the lateral motion of the particle from its predicted Stokes-Einstein diffusivity, D_o, and these effects can be accounted for with a hydrodynamic correction factor[88] as,

$$D_{\|}(h) = D_o f_{\|}(h) \tag{6.6}$$

where $f_{||}$ is a rational fit to the exact solution[89] as,

$$f_{\|}(h) = \frac{1220\omega(h)^2 + 5654\omega(h) + 100}{12420\omega(h)^2 + 12233\omega(h) + 431} \tag{6.7}$$

where $\omega(h) = h/(a+\delta)$ and δ is the macromolecular layer thickness. The distribution of heights sampled by the particle, $p(h)$, can be related to the net particle-surface interaction potential with Boltzmann's equation[90, 91] as,

$$p(h) = \exp(-u_{ps}(h)/kT) \tag{6.8}$$

and predictions of the average lateral diffusion coefficient, $\langle D_{||} \rangle$, can be made using the distribution of heights sampled given by,[92]

$$\left\langle D_{\|} \right\rangle = \frac{\int D_{\|}(h)\, p(h)\, dh}{\int p(h)\, dh} \tag{6.9}$$

6.2.3 Particle-Surface Association Lifetime

A characteristic time scale of colloidal diffusion, τ_a, can be determined as

$$\tau_a = \frac{l_{pp}^{\ 2}}{\left\langle D_{\|} \right\rangle} \tag{6.10}$$

for a given characteristic length scale, l_{pp} = 607 nm, chosen here as the pixel scale in DFVM images. The association lifetime of a colloidal particle to a surface, t_a, is

dependent on this characteristic time scale and the net colloid-surface interaction potential as approximated by,[71, 172]

$$t_a \approx \tau_a \exp(|u_{\min}|/kT) \tag{6.11}$$

and can be rearranged to relate t_a to $u_{\min}$ directly as

$$\ln(t_a/\tau_a) \approx |u_{\min}|/kT \tag{6.12}$$

where $\exp(|u_{\min}|/kT)$ is the probability a particle will escape an attractive energy well with depth $u_{\min}$ assuming a Boltzmann distribution of thermal energies and reduces to τ_a when no net colloid-surface interaction is present. To determine if colloids were associated to the surface, the position of the particle was monitored for time τ_a = 6.14 s (6 consecutive images) and if the coordinates in these images had a standard deviation σ_{xy} < 120 nm, the particle was considered associated to the surface. This tolerance was determined from the theoretical diffusion-limited motion of a particle at contact with a surface calculated from Eq. (6.6).

6.2.4 Particle-Cell Surface Interaction Potentials

Histograms of particle center to cell boundary distance, $p(r)$, can be constructed as described in *Chapter 3*. With these histograms, particle-cell surface potentials of mean force, $W(r)$, can be calculated with Boltzmann's equation as,

$$W(r) - W(r_{ref}) = -\ln\left(\frac{p(r)}{p(r_{ref})}\right) \tag{6.13}$$

where r_{ref} is a reference particle-cell surface separation with $W(r_{ref}) = 0\ kT$. As the particle will only interact with the cell at $r/a < 1$, r_{ref} was chosen at $10a$ where no effective interaction with the cell is expected.

6.3 Materials and Methods

6.3.1 Batch Cell Preparation

Glass cover slips (24 mm x 60 mm, Corning Life Science, Tewskbury, MA) were hydrophobically modified by spin coating polystyrene onto their surface. The substrates were first cleaned by sonication in acetone for 30 minutes then placed in Nochromix (Godax Laboratories, Cabin John, MD) overnight. Next, they were rinsed 20x times with DI water then sonicated in 0.1 M KOH for 30 minutes. They were again rinsed 20x times with DI water and dried with nitrogen. A thin film of polystyrene is made on the glass cover slip using a spin coater (Laurell Technologies Corp., North Wales, PA) by placing ~500 µL of 3% (w/w) solution of polystyrene in toluene onto the cover slip and spinning at 1000 RPM for 40 s. To create a batch cell, the slides were allowed to dry for 30 minutes before adhering a 1 mm ID Viton O-ring (McMaster Carr, Inc., Robbinsville, NJ) onto the slide with vacuum grease. Twenty-five µL of 1000 PPM (1 mg/mL) solution of F108-Pluronic (PEG-PPO-PEG triblock copolymer, BASF, Wyandotte, MI) are added to the batch cell and allowed to adsorb for 4 hours. Excess, un-adsorbed F108-pluronic was removed by rinsing with a pipette 5 times with phosphate buffered saline (PBS, Invitrogen, Carlsbad, CA) before each experiment.

6.3.2 Hyaluronic Acid-Coated Cover Slips With Adherent Cells

A protocol adapted from literature was used to adhere HA to silica surfaces.[176] Glass cover slips (18 mm x 18 mm, Corning Life Science, Tewskbury, MA) were first cleaned with sonication in acetone for 30 minutes and allowed soak overnight in Nochromix. Next, they were rinsed 20 times with DI water followed by sonication in 0.1 M KOH for 30 minutes. They were again rinsed 20 times with DI water and dried with

nitrogen. The cover slips were allowed to dry for an additional 30 minutes before being placed in 2% (w/w) APTES solution in ethanol for 24 hours for amino-silane functionalization. To rinse excess APTES away from the surface, slides are first sonicated in ethanol for 30 minutes, followed by sonication in water for 30 minutes, and then dried with nitrogen. A 3 mg/mL HA (100 kDa, Lifecore Biomedical, Chaska, MN) solution was made in DI water filtered with a Anotop 0.02 μm syringe filter (Whatman. Pittsburgh, PA) to ensure sterility. 500 μL of the HA solution were placed on each APTES-coated cover slip and were kept covered in a dish coated with moist towels to chemisorb for at least 20 hours. Once the HA chemisorption step was completed, the HA-coated cover slips were placed under UV irradiation for 30 minutes to ensure sterility and then placed into a 6-well plate (Corning Life Science, Tewskbury, MA) in PBS. MDA-MB-231 epithelial breast cancer cells (MDA231, National Cancer Institute Physical Sciences-Oncology Center (NCI-PSOC), National Institues of Health, Bethesda, MD) were maintained in DMEM (Invitrogen, Grand Island, NY) containing 10% (v/v) fetal bovine serum (FBS, Atlanta Biologicals, Flowery Branch, GA).[177] MDA231 cells were seeded onto HA-coated coverslips at a 1:4 ratio (~50,000 cells/cm^2) in complete media (10% FBS in DMEM). The cells are then allowed to adhere and spread onto the HA-coated coverslips overnight before each experiment.

6.3.3 Physisorption of F108-Pluronic (PEG) and BSA to Colloidal Silica

Silica particles were modified with a hydrophobic octadecanoic acid layer using a procedure adapted from literature. [107] A 1 mL solution of as purchased SiO_2 colloids (2.34 μm, Bangs Laboratories, Fishers, IN) was made in deoionized water. Using a micro-centrifuge (MiniSpin-plus, Eppendorf, Hamburg, Germany), the particle solution

was centrifuged at 5.5k RPM for 90 s and re-suspended in DI water 5 times followed by centrifugation at 5.5k RPM for 90 s and re-suspension 5x in 200 proof ethanol to remove water from the particle solution. The particle solution was then added to 9 mL of 0.1 mg/mL solution of 1-octadecanol in 200 proof ethanol in a 50 mL round bottom flask. On a stirring hot plate, the solution was mixed and heated at 50ºC under a nitrogen blanket (reactant mixture is flammable) until the 1-octadecanol is dissolved. Once the ethanol has evaporated, the nitrogen stream was removed and the flask is heated to 200ºC and held at this temperature for 3 hours to fixate the 1-octadecanol to the surface of the particles. Once the reaction has completed, the vessel is cooled to 25 ºC and the reactant mixture is recovered with 4 mL of chloroform to dissolve any free 1- octadecanol from solution. The particle solution was then centrifuged at 5.5k RPM for 90 s and re-dispersed in chloroform 5 times followed by centrifugation and re-dispersion in 200 proof ethanol an additional 5 times to remove all chloroform. To adsorb macromolecules to the 1-octadecanol coated silica particles, the particles are dispersed in 1 mg/mL F108-pluronic or BSA solutions for at least 4 hours. Excess F108-pluronic or BSA is removed by centrifugation at 5.5k RPM for 4 min and re-suspension in DI water 5 times.

6.3.4 Chemisorption of Dextran and Hyaluronic Acid to Colloidal Silica

Colloidal silica particles were functionalized with polysaccharides using silane linkers with a procedure adapted from literature.[109, 176] Before functionalization, silica particles were washed by centrifugation at 5.5k RPM for 90 s and re-dispersion in fresh DI water. This washing step was repeated 5 times. The particles were then dispersed in dry ethanol and washed an additional 5 times in dry ethanol. To modify particles with an epoxy silane linker, the particles were then dispersed in a 0.1% (v/v) solution of 3-

glycidoxypropyltrimethoxysilane (GPTMS, Sigma, St. Louis, MO) in dry ethanol for 1 hour. To modify particles with an amino silane linker, the particles were dispersed in a 2% (w/w) (3-aminopropyl)triethoxysilane (APTES, Sigma, St. Louis, MO) in dry ethanol for 24 hours. The silane linker-modified silica colloids were then washed 5 times in dry ethanol and 5 times in DI water. To conjugate dextran (500 kDa, Sigma, St. Louis, MO) onto silica particles, Epoxy-silane (GPTMS) modified colloids were then dispersed in 30% (w/w) aqueous solution of polysaccharide solution and gently mixed with a magnetic stir bar for 24 hours. To conjugate hyaluronic acid (HA, 1 MDa, R&D Systems, Minneapolis, MN) to silica particles, amino-silane (APTES) modified colloids were dispersed in 3 mg/mL HA solutions for at least 20 hours. The polysaccharide-modified particles are then centrifuged at 10,000 RPM for 10 minutes and re-dispersed in fresh DI water. They are then washed with DI water an additional 5 times. Pluronic-F108 is then physisorbed onto the polysacharide-modified particles by dispersing the particles in 1000 ppm (1 mg/mL) aqueous solution of F108-Pluronic overnight. The F108 coating step is to ensure the particles are fully coated with a polymer brush to improve colloidal stability. The particles are then rinsed 5 times in DI water and then dispersed in PBS.

6.3.5 Preparation of Samples for Dark Field Video Microscopy

Protein, polymer, or polysaccharide coated silica particle solutions were diluted at a 1:10 ratio in complete media (10% FBS in DMEM). 100 μL of particle solution in complete media was added into an F108-Pluronic (PEG)-coated batch cell and particles are allowed to sediment for 2-3 minutes. The batch cell was then irradiated under UV for 30 minutes to sterilize the sample. Next, the o-ring on the batch cell was removed and a HA coated coverslip seeded with MDA-231 cells is placed on top of the 100 μL drop of

particle solution. The sample is then sealed along its edges with nail polish. For imaging, the samples are inverted so the particles can then sediment onto the surface with adherent cells and placed on the microscope with an attached temperature controller (BC-110, 20/20 Technology, Wilmington, NC) kept at 37º C for the duration of the experiment. Experiments were performed using an inverted optical microscope (Axioplan 2, Carl Zeiss, Obercheken, Germany) with a dark field condenser (dry, 0.8/0.95 NA, Carl Zeiss) and a 40x objective (LD-Plan Neofluar, NA = 0.75, Carl Zeiss). Images are collected with a 12-bit CCD camera (ORCA-ER, Hamamatsu, Hamamatsu City, Japan) operated in binning mode 4 (length per pixel, l_{pp} = 0.607 μm/pixel, Image area, A_i = 336 pixels x 256 pixels = 203 μm x 155 μm) at a 1 s frame rate for a total of 1800 frames (30 min duration). The particle trajectories off and on the cell surface are determined using image analysis algorithms coded in MATLAB that have been described in *Chapter 3*.

6.4 Results and Discussion

6.4.1 Tracking Colloidal Particles Interacting With Live Cells

The diffusion of colloidal silica particles functionalized with PEG, BSA, dextran, and HA over an HA-coated substrate with adherent MDA231 epithelial breast cancer cells was studied to measure nonspecific and specific biomacromolecular interactions with the surface of the cells. As shown with Eqs. (6.8) and (6.9), the diffusivity of colloidal particles near a surface can be directly related to equilibrium and non-equilibrium particle-surface interactions. The buoyant weight of micron-sized particles will confine their diffusion to separations near the surface and their lateral motion will depend highly on its interactions with the surface. At physiological ionic strengths, steric interactions between macromolecular layers on the particle and surface are required to

levitate the particle above the surface to allow it to diffuse laterally. While the macromolecular coating on the particles varied across cases, the silica substrates used in this work were coated with HA to provide both steric stability for the particles and an adherent surface for cell seeding. Low particle densities, with area fractions from 0.01 - 0.05, were used to limit particle-particle interactions that could effect particle diffusion or particle-cell surface interactions.

Fig. 6.1 shows an example image taken from a DFVM experiment clearly showing particles and cells with high contrast suitable for the analysis techniques discussed in *Chapter 3*. Coordinates are determined for the cell boundary, drawn as white lines in Fig. 6.1, and the particle centers are found, shown as red circles in Fig. 6.1. Particle centers and cell boundaries are found in each image and the trajectories of particles were determined allowing for measurement of particle dynamics both off the cell surface, shown as red lines in Fig. 6.1, and on the cell surface, shown as green lines in Fig. 6.1. The trajectories of the particles will be highly dependent on their interactions with the underlying surface and with our analysis tools, particle dynamics can be measured on the cell surface and the background substrate.

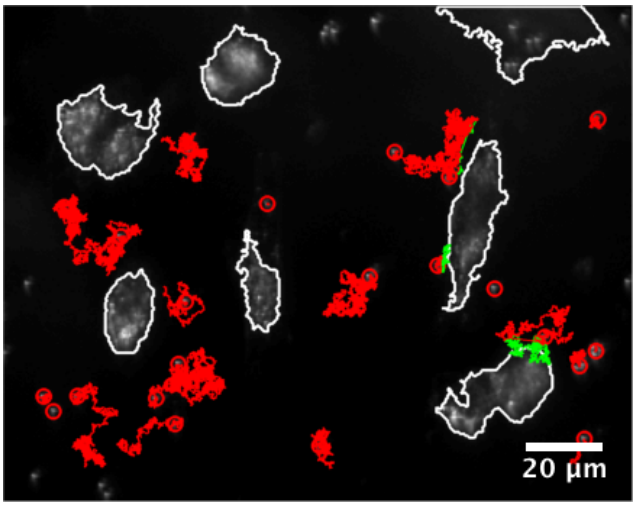

Figure 6.1 Colloidal trajectories of PEG-coated 2 µm silica particles interacting with MDA231 cells from DFVM experiments processed with image analysis in MATLAB. Cell boundaries at $t = 0$ are drawn in white. Particle centers are marked with a red circle and trajectories are drawn as lines with their color depending whether the particles is within the cell boundaries (green lines) and outside the cell boundaries (red lines).

6.4.2 Particle Diffusion Off and On Cell Surfaces

Hydrodynamic particle-surface interactions will hinder the lateral motion of colloidal particles to rates much slower than its predicted Stokes-Einstein diffusivity. Nonspecific and specific macromolecular interactions between the particle and surface will further increase the degree of hindrance to particle diffusion depending on the density and structure of the macromolecular layers on each surface. The trajectories of colloidal particles were measured both on the HA-coated substrate, shown as red lines in Fig. 6.1, and on the cell surface, shown as green lines in Fig. 6.1, to see how the diffusion of particles compared between each surface. The mean squared displacement was determined off the cell surface (on HA-coated substrate) and on the cell surface shown in Fig. 6.2 for each macromolecular coating used. The diffusion rate was fit with theory that accounts for hydrodynamic interactions with the surface and the particle-surface

macromolecular layer thickness was predicted for each case that is summarized in Table 6.1.

Table 6.1 Parameters from theoretical fits determined from Eq. (6.6) to mean squared displacement data shown in Fig. 6.2 of particles off cell surface (HA) and on cell surface (MDA231).

Particle/Surface	$\langle D_{\|\|} \rangle$ ($\mu m^2/s$)	δ (nm)	δ_p (nm)	δ_s (nm)
PEG/HA	0.066	26	11	15
BSA/HA	0.07	23	8	15
Dextran/HA	0.053	30	15	15
HA/HA	0.053	30	15	15
PEG/MDA231	0.075	21	11	10
BSA/MDA231	0.075	21	8	13
Dextran/MDA231	0.057	29	15	14
HA/MDA231	0.012	-	-	-

The mean squared displacement of particles on the HA-coated substrate is shown in Fig. 6.2A for each macromolecular coating. The measured diffusivities for each case are reasonable when hydrodynamic and nonspecific macromolecular interactions are considered for particles diffusing near a surface. The total thickness of the macromolecular layers on the particle and surface, $\delta = \delta_p + \delta_s$, were found with Eqs. (6.6) and (6.7). The thickness of adsorbed PEG monolayers have been measured directly with total internal reflection microscopy[172] and was used to determine each individual layer thickness with values shown in Table 6.1. As the thickness of the layers increases, diffusion is further hindered due to the increase in effective particle size. The rate of diffusion from each case increases as expected based on the thickness of each macromolecular layer. BSA-coated silica, δ_p = 8 nm, diffused most rapidly over the surface as it is expected to have the thinnest layer on its surface and PEG, with δ_p = 11 nm, diffused more slowly. Dextran and HA had slighty thicker macromolecular layers,

with δ_p = 15 nm, and showed the slowest diffusion over the HA-coated substrate. These results show that the particles interact nonspecifically with the background HA-coated surface which gives us confidence when we analyze their trajectories on cell surfaces that (1) the particles are diffusing primarily in 2D near the surface and (2) these coatings provide sufficient steric stability to prevent nonspecific adhesion to surfaces.

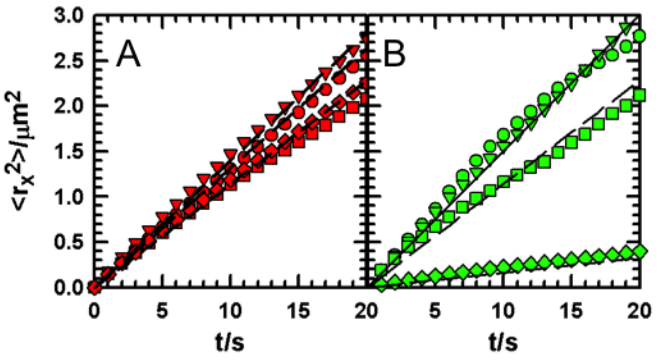

Figure 6.2 Mean squared displacement of PEG (circles), BSA (triangle down), Dextran (squares), and HA (diamonds) coated 2 μm silica when (A) off MDA231 cell surface (red) and (B) on MDA231 cell surface (green). Dashed lines from theoretical fits with Eq. (6.6) to diffusion data.

Measurements and theoretical fits of mean squared displacement of colloidal particles on the MDA231 cell surface are shown in Fig. 6.2B for each case. A variety of membrane-associated proteins and carbohydrates are present on the surface of the cell which lead to nonspecific and specific interactions with the synthetic and biological macromolecules on the particle surface. Net repulsive steric interactions lead to hindered diffusion rates due to hydrodynamic interactions with the cell surface for PEG, BSA, and dextran coated silica particles. In comparison to on the backgroud substate, the lateral diffusion of PEG, BSA, and dextran were similar on the surface of the cell with only slight decreases in fits for δ shown in Table 6.1. The macromolecular layer thickness on

the cell surface, δ_s, varied from 10-14 nm for each of these cases. The layer thickness of cell-surface associated glycoproteins, glycolipids, and carbohydrates, known as the glycocalyx, can vary widely in size from nanometers to several microns dependent on cell and tissue type.[178, 179, 180] Our measurements, on the order of nanometers, are consistent with *in vitro* measurements of glycocalyx thickness.

HA-coated particles were immobilized on the surface of the cell with a large reduction in diffusion rate ($\langle D_{||} \rangle \approx 0.05 D_o$). The MDA231 cell line used in this work has been thoroughly characterized and has shown abnormal overexpression of CD44, a transmembrane protein known to interact specifically with HA in the extracellular matrix.[10, 177] Unlike the net repulsive interactions seen in prior cases, strong, attractive particle-surface interactions are induced by specific CD44-HA interactions which lead to association of particles to the cell surface. While we can infer changes from net repulsive to net attractive particle- cell surface interactions based on measured lateral diffusion rate, the next sections will show how more direct, quantitative measurements of colloidal interactions with the surface of the cell can be made.

6.4.3 Particle-Cell Surface Association Lifetimes

Rather than using ensemble measurements of diffusion such as mean squared displacement, analysis of individual trajectories can provide local information on dynamics of particles interacting with cells that can be related to net particle-cell surface interactions. As shown in Eq. (6.12), the association time of particles to a surface, t_a, has kT-scale sensitivity to the particle-surface attractive well depth, u_{min}. To determine if colloidal particles have associated to the cell surface, the displacement of the particle can be measured over a characteristic time scale, τ_a = 6.14 s, chosen based on the diffusion-

limited motion of the particle. In the limit of no net attraction with the cell surface, t_a reduces to the diffusion-limited time τ_a and will increase exponentially with only small increases in net particle-surface attraction. With this measurement, weak, intermittent association as well as strong, irreversible association to the cell surface can be detected which is important in evaluation of nonspecific and specific macromolecular coatings for biomedical applications. Fig. 6.3 shows measured association lifetime histograms, $p(t_a)$, for PEG, BSA, Dextran, and HA-coated particles on the surface of MDA231 cells. As t_a depends exponentially on u_{min}, histograms were populated from τ_a (6.14 s) to the total time of each experiment (1800 s) over 10 bins with exponential spacing shown in Table 2. A linear color scale of $\ln(t_a/\tau_a) \approx |u_{min}|/kT$ is used for each bar to show the net particle-cell surface attraction determined for each association time.

Table 6.2 Parameters used for association lifetime histograms and logarithmic color scale for $\ln(t_a/\tau_a) \approx |u_{min}|/kT$ shown in Fig. 6.3.

Bin	t_a (s)	$\ln(t_a/\tau_a)$	color
1	6.14	0	violet
2	11.5	0.63	dark blue
3	21.7	1.26	blue
4	40.8	1.89	blue-gray
5	76.7	2.52	green
6	144	3.16	light green
7	271	3.79	yellow
8	509	4.42	orange
9	958	5.05	orange-red
10	1800	5.68	red

A histogram of association lifetimes for PEG-coated particles to MDA231 cells, shown in Fig. 6.3A, showed only minimal sampling of association lifetimes greater than τ_a. Particles largely show short association times indicative of net repulsive interactions

with the surface of the cell. This is consistent with the average ensemble diffusion of PEG-coated particles on MDA231 cells, shown in Fig. 6.2B, where particles were able to freely diffuse on the cell surface. As PEG is commonly used as a stabilizing coating against nonspecific adhesion, no net attraction was expected for particles with dense PEG brushes on their surface. The association lifetimes for BSA-coated particles, shown in Fig. 6.3B, was similar to the PEG-coated particles with the mode association lifetime at τ_a and again was consistent with their ensemble average lateral diffusion. As serum adsorption is known to facilitate adhesion for *in-vitro* cell culture and cellular uptake of nanoparticles, longer association lifetimes could be expected in this case. However, changes in particle-cell interactions have been observed for particles with pre-formed, adsorbed serum layers (as in this work) compared to serum from surrounding medium dynamically forming layers on the particle surface.[181, 182] The composition (i.e. profile of adsorbed serum proteins) and architecture (i.e. dense and irreversible versus soft and exchangeable serum layers) of the corona also greatly impact protein corona-mediated particle-cell interactions.

While largely short association lifetimes were measured for dextran-coated particles shown in Fig. 6.3C, some weak, intermittent association lifetimes were seen in this case. In comparison to PEG, dextran clearly shows longer-lived association to the cell surface and weak, net attraction to the surface of the cell. The ensemble average lateral diffusion measurement for dextran on the cell, shown in Fig. 6.2C, would indicate little change in particle dynamics and clearly is an insensitive measure of weak, reversible particle-surface interactions. For natural and synthetic polymer coatings like dextran and PEG used to prevent adhesion of drug delivery particles to surrounding

tissues and compromise of implanted devices due to biofouling,[183, 184, 185] measurements of particle-cell surface association lifetime can be used as a highly sensitive metric of anti-adhesive properties.

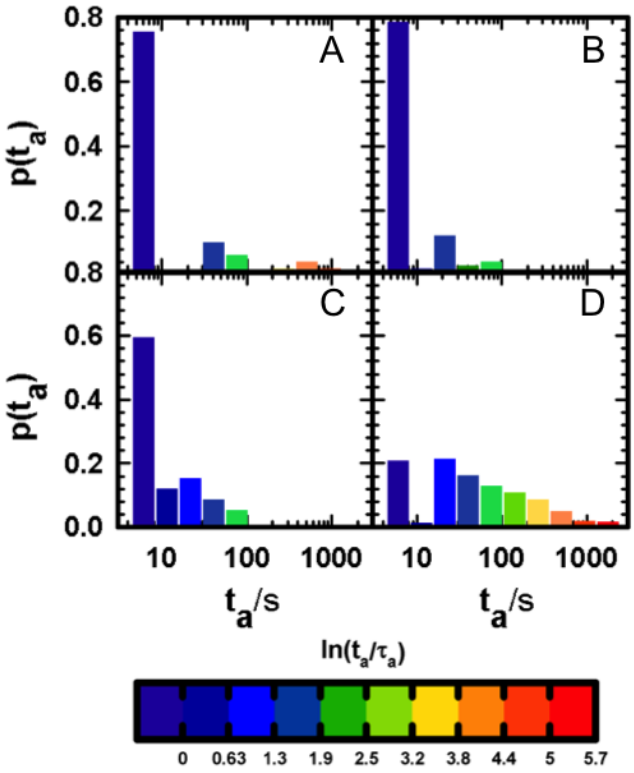

Figure 6.3 Association lifetime histograms, $p(t_a)$, for (A) PEG-coated, (B) BSA-coated, Dextran-coated (C), and HA-coated (D) 2 µm silica particles on the surface of MDA231 cells. Histograms constructed from particle trajectories within cell boundaries (shown as green lines in Fig. 6.1). Each bar has a linear color scale of $\ln(t_a/\tau_a) \approx |u_{min}|/kT$

To probe specific interactions with MDA231 cells, the interactions of HA-coated particles with the cell surface were measured. The association lifetime histogram for HA-coated particles, shown in Fig. 6.3D, contrasted greatly with the short association lifetimes measured in other cases. A striking increase in long association lifetimes is observed for HA-coated particles with the mode at t_a = 21.7 s (~$4\tau_a$). As overexpression

of CD44 is common for MDA-MB-231 and other cancerous cell types, CD44 binding of HA leads to increases in t_a due to strong, net particle-cell surface interactions. While specific CD44-HA interactions are typically weak with K_d ranging from 1 μM - 1 mM,[186] multi-valency on the particle scale will allow for many CD44-HA bonds to form in parallel and induce strong adhesion to the cell surface.

6.4.4 Particle-Cell Surface Interaction Potentials

In addition to dynamic measures of cell-surface interactions, equilibrium particle-cell surface interactions can be assessed with our image analysis tools. As shown in *Chapter 3*, the radial distance between particle centers and nearest cell boundary, r, can be measured and histograms of particle-cell surface separations, $p(r)$, are constructed. Figure 6.4 shows the particle – cell surface separation histograms for each case. Changes in sampled r measured in the particle-cell radial distributions can be related to particle-cell surface interaction potentials with Eq. (6.13). For the quasi-2D interactions of particles with cells in our experiments, this reduction in dimensionality provides a relevant measure of equilibrium interactions with the cell surface. Fig. 6.5 shows the measured particle-cell surface interaction potentials for each particle coating. A reference state is chosen at $r = 10a$ as it is assumed no net interactions between the particle and the cell surface will occur at such far separations.

In the radial distribution of PEG-coated particles shown in Figure 6.4A, a relatively constant distribution of distances are sampled at separations greater than $2a$. At these separations far from the cell, the sampling will simply depend on the area fraction of particles on the surface which is observed with $p(r) \approx 1$. Values of $r < 0$ are given for radial positions sampled within the cell boundaries and sampling at these positions

remains relatively constant for PEG coated particles until separations in the range $r < -2a$. Decreased sampling at $r < -2a$ was a common feature in the distributions across all cases. The distribution of distances sampled for BSA and dextran-coated particles approaching the cell ($r < 2a$), shown in Fig. 6.4B and 6.4C respectively, was much different then PEG with increased sampling at these distances. HA-coated particles also showed an increase in sampling as they approached the cell and even further increased sampling within the cell boundaries ($-2a < r < 0$).

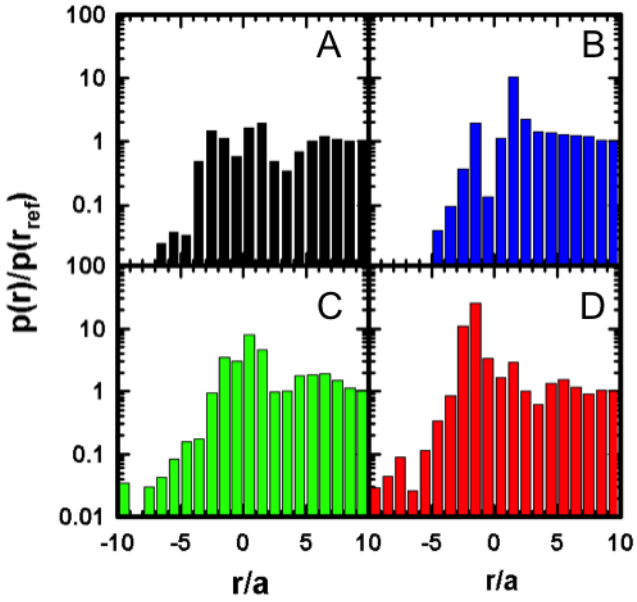

Figure 6.4 Ensemble average particle-cell radial distribution function, $p(r)$, for (A) PEG-coated, (B) BSA-coated, (C) Dextran-coated, and (D) HA-coated 2 μm silica particles interacting with MDA231 cells normalized by $p(r_{ref} = 10a)$.

To interpret thes distributions, particle-cell surface interaction potentials were determined from the measured $p(r)$ shown in Fig. 6.4. From the particle-cell surface interaction potential for PEG-coated particles shown in Fig. 6.5A, no net interactions are observed at separations greater than $2a$ as would be expected at such large distances from

the cell. As the particle approaches the surface ($r < 2a$), the free energy fluctuates around ~0 kT with no appreciable attraction to the cell surface. As it diffused further onto the cell ($r < -2a$), a net repulsive interaction is seen. While no net interactions are expected based on measured association lifetimes for PEG-coated particles shown in Fig. 6.3A, a gravitational barrier to diffusion laterally onto the cell could be present due to cell topography. Although the ensemble average interactions of the particles with the cells cannot directly yield single cell topography, a gradual increase in height would be expected based on the "hill" shape characteristic of cells cultured in 2D.[187]

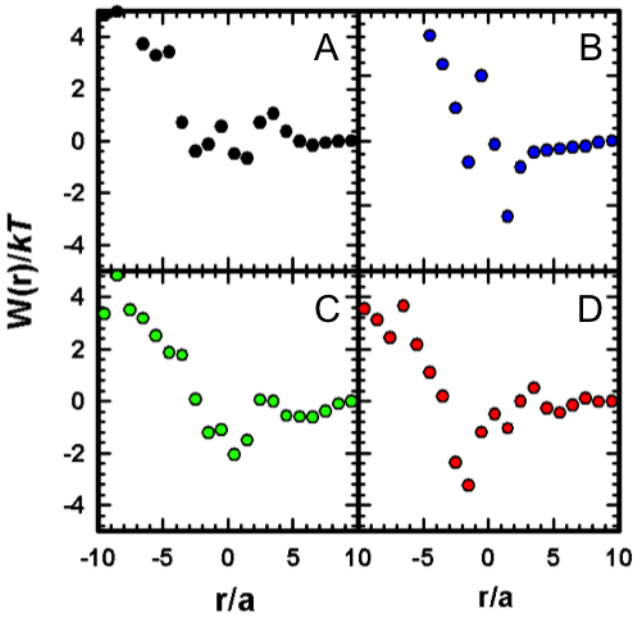

Figure 6.5 Ensemble average particle-cell surface potentials of mean force, $W(r)$, determined from radial distribution functions in Fig. 6.4 for (A) PEG-coated, (B) BSA-coated, (C) Dextran-coated, and (D) HA-coated 2 μm silica particles interacting with MDA231 cells.

Interaction potentials measured for BSA and dextran coated particles with MDA231 cells, shown in Fig. 6.5B and 6.5C respectively, both showed net attraction at particle-cell surface contact (at $r \approx a$) with repulsion to radial positions further on top of

the cell ($r < -2a$). With attractive minimum of ~2 kT for BSA and dextran coated particles, reversible association to the cell surface would be expected and is consitent with measured association dynamics in Fig. 6.4. Net attraction to the cell surface is seen for HA-coated particles at radial positions on the cell (at $-2a < r < a$). The attractive minimum of ~4 kT will lead to much stronger particle cell-surface association and is again consistent with the long association lifetimes of HA-coated particles on the cell surface shown in Fig. 6.3D. While sampling limits quantitative determination of these free energy landscapes, the trends observed help to show the differences in particle – cell surface interactions mediated by synthetic and biological macromolecules present on the particle surface. The steepness of repulsion varies from case to case, but the overall trend is consistent with a gravitational barrier to diffusion on top of the cell. $W(r)$ can be used as a composite measure of biomolecular and biophysical properties of the cell as differences in these potentials arise from the net contributions of biomacromolecular interactions and ensemble average topography of the cells.

6.5 Conclusions

In this work, dark field video microscopy combined with newly developed image analysis techniques was used for real-time, simultaneous tracking of particles and cells. Quantitative analysis of single colloidal trajectories allowed for direct measurements of particle-cell surface association lifetimes that showed remarkable sensitivity to changes in surface chemistry. In addition, equilibrium particle-cell surface interactions were measured from ensemble average radial particle positions with respect to the surface of the cell. This technique provides a highly sensitive assay of particle-cell surface interactions capable of interrogating nonspecific, specific biomolecular interactions as

well as biophysical interactions between particles and cells. These results also show promise as a non-intrusive, high-throughput techniqe for mapping live cell and tissue topography using diffusing colloidal probes. Ultimately, our findings demonstrate a powerful technique for characterization of biomaterial-cell surface interactions crucial to biosensing, drug delivery, diagnostic imaging, and tissue engineering applications.

7. DESIGNING SUPER-SELECTIVE DRUG DELIVERY NANOPARTICLES USING MONTE CARLO SIMULATIONS

7.1 Introduction

Targeted drug therapies have gained much attention for the preferential delivery of medicine to diseased tissues, with benefits including reduced damage to healthy tissues and have significantly lowered dosages required. In nanoparticle-based drug therapies, targeting agents can be introduced to the particle surface to allow for the selective binding to membrane proteins with anomalous or over-abundant expression in diseased cells. If a membrane protein is exclusively expressed on diseased cells, functionalization with high affinity targets (i.e. antibodies) allows for nanoparticles to selectively bind to cells with this protein present.[188, 189] This strategy has been effective for a number of diseases such as arthritis,[190] cancer,[191] and multiple sclerosis.[192] However, if the target protein is present at moderate levels on healthy cells, high-affinity targeting agents lose selectivity due to adherence to both diseased and healthy cells which is typical for many therapeutic targets. In such situations, recent work has shown that binding selectivity can be recovered by engineering nanoparticles with weaker targeting affinity, which require multi-valent binding that can only be induced at cell surfaces with abnormally high expressions of the target membrane proteins. This has been demonstrated with targeting of integrins with the reactive tripeptide sequence of fibronectin, RGD,[193, 194, 195] and targeting of CD44 with hyaluronic acid (HA)[196, 197, 198, 199, 200] for delivery of chemotherapeutics for cancer.

Designing nanoparticles for super-selective targeted delivery with experimental assays alone is challenging and labor intensive due to a variety of possible functionalization strategies. Comprehensive models of nanoparticle-based therapies can

provide guidance in choosing nanoparticle designs to narrow the parameter space for more efficient screening. Recent modeling efforts have aimed to characterize the nanoparticle-cell interactions mediated by ligand-membrane protein targeting with analytical and simulation techniques. Nanoparticle design parameters ranging from ligand binding affinity, ligand density, ligand tether length, tether valency (i.e. bi-, tri-, tetravalent tethers), and substrate rigidity have been investigated for cell surfaces with varying densities of target membrane proteins.[78, 201, 202, 203, 204, 205] Notably, Frenkel et. al.[206] developed an analytical model of super-selective nanoparticle binding which demonstrated how weak, multi-valent binding allowed for selectivity for surfaces with high densities of target biomacromolecules. However, realistic, experimentally-determined binding affinities have not been investigated for these systems as translating measurable parameters (such as dissociation constant, K_d) to inputs for modeling nanoparticle-cell surface interactions is not straightforward. Also, experimentally determined membrane protein densities for healthy and infected cells have yet to be used as inputs into these models. Using parameters representative of the actual diseased and healthy cell populations will allow for more accurate predictions of selectivity for targeted nanoparticle drug vectors.

Binding affinities for many target membrane proteins have been measured experimentally using FRET,[207] NMR,[186, 208] and SPR.[170, 209, 210] However, these ensemble measurements of ligand-protein association do not directly yield single molecule binding energetics. In *Chapter 5*, formalism was developed to predict K_d for an input ligand-receptor interaction potential allowing for more realistic representations of these systems. This same technique will be applied in this study to represent specific target membrane

proteins overexpressed on diseased cell surfaces. Quantitative measurements of membrane protein expression have been made using flow cytometry for weak affinity target membranes on healthy and diseased cells[177, 211, 212, 213] and these values were used as inputs into the model.

In this work, Monte Carlo simulations were used to study nanoparticle-cell interactions mediated by specific interactions between surface-immobilized ligand receptors on the particle and target membrane proteins on the surface of a cell. Parameters most relevant towards the design of targeted drug delivery vectors were explored to determine their effects on the net particle-cell surface interactions. For example the dissociation constant, K_d, determines how strongly the ligand and protein will interact which changes the net interaction between the particle and cell. Since weaker binding affinities are most relevant toward super-selective targeting therapies, K_d in the mM to μM range were explored. In order to investigate realistic membrane protein densities for healthy and diseased cells, a range of membrane protein densities was chosen based on flow cytometry measurements of CD44 expression where 233 ± 52 molecules/μm^2 were found on colon carcinoma cells compared to 66 ± 6 molecules/μm^2 on healthy platelets.[214] In modeling these highly complex biological systems, exploring parameters that closely match those in real systems will better demonstrate what is required to design nanoparticles with high selectivity.

7.2 Theory

7.2.1 Ligand-Membrane Protein Interaction Potentials

Membrane proteins in this work are represented as hard spheres that interact specifically with receptors on the particle surface represented as points in space. In order

to introduce an effective size to the membrane proteins, they can be modeled as hard nanospheres with an isotropic (i.e., no orientation dependence) attractive well on their surface. For the ligand-membrane protein nanosphere potential, U_{LPN}, we use the form,

$$\begin{aligned} U_{LPN}(r) &= \infty && \text{if } r < a_P \\ U_{LPN}(r) &= \frac{1}{2}k_s(r-a_P)^2 - u_{\min} && \text{if } a_P \le r \le a_P + \delta \\ U_{LPN}(r) &= 0 && \text{if } r > a_P + \delta \end{aligned} \tag{7.1}$$

where r is the ligand to membrane protein separation, a_{p} is the radius of the protein, $u_{\min}$ is the ligand-protein attractive well depth, and δ is the range of the attractive well. The goal in this work is to model the specific interactions of ligands and membrane proteins with realistic dissociation constants and in the next section, we will show how this can be determined.

7.2.2 Determining K_{d} for Ligand- Membrane Protein Interaction Potentials

An analytical expression for the dissociation constant, K_{d}, of a harmonic well potential can be determined using the Bjerrum approach of Luo and Sharp to calculating absolute macromolecular binding free energy. For a simple harmonic well potential with the form,

$$\begin{aligned} U_{LP}(r) &= \frac{1}{2}k_s r^2 - u_{\min} && \text{if } 0 < r < \delta \\ U_{LP}(r) &= 0 && \text{if } r > \delta \end{aligned} \tag{7.2}$$

the K_{d} can be calculated with the expression,[100]

$$K_d = \left[(2\pi)^{\frac{3}{2}} \left(\frac{k_s}{kT}\right)^{\frac{-3}{2}} e^{\left(\frac{-U_{\min}}{kT}\right)} \right]^{-1} \tag{7.3}$$

This is limited to predictions for these simple harmonic well potentials without an effective size. An alternative formalism was developed in *Chapter 5* to determine K_{d} for

membrane protein nanospheres. We begin by calculating the second virial coefficient, B_2, for the protein nanospheres to estimate their effective interaction strength. The second virial coefficient for the protein nanosphere, $B_{2,\mathrm{LPN}}$, is calculated with the following expression,

$$B_{2,LPN} = 4V + 12\int_{a_P}^{a_P+\delta} r^2\left(1-e^{\left(\frac{-U_{LPN}(r)}{kT}\right)}\right)dr \tag{7.4}$$

The first term is the hard sphere component of $B_{2,\mathrm{LPN}}$ that is simply four times its volume, V. The second term accounts for the harmonic well tail component of $B_{2,\mathrm{LPN}}$ and this is calculated using an expression which can be applied to any arbitrary potential to determine B_2[101]. Next, a simple harmonic well with the same effective ineraction strength (i.e same B_2) must be founde. The second virial coefficient of a harmonic well potential, $B_{2,\mathrm{LP}}$, is calculated as,

$$B_{2,LP} = 12\int_{0}^{\delta} r^2\left(1-e^{\left(\frac{-U_{LP}(r)}{kT}\right)}\right)dr \tag{7.5}$$

using the same expression to determine B_2 for any arbitrary potential. To find an equivalent harmonic well potential, $u_{\min}$ in Eq. (2.28) (7.2) for U_{LP} is adjusted at constant k_{s} until $B_{2,\mathrm{LP}}$ is equal to $B_{2,\mathrm{LPN}}$ of the membrane protein nanosphere. The K_{d} of the harmonic well calculated from Eq. (7.3) is then assigned to the membrane protein nanosphere potential. This approach was found to accurately predict K_d for MC simulations of protein nanospheres interacting with ligands in *Chapter 5*.

7.3 Methods

As is illustrated in Figure 7.1, a colloidal particle (a = 100 nm) decorated with ligand receptors distributed with equal spacing, s_{rec}, on its surface was allowed to

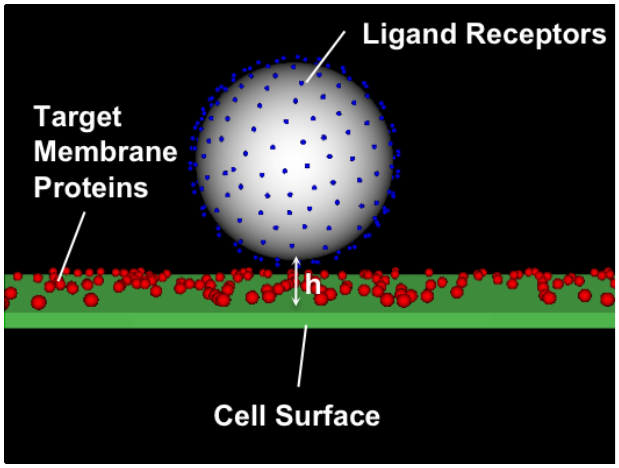

Figure 7.1 Schematic of receptor-ligand mediated nanoparticle-cell interactions.

translate and rotate in 3D above a membrane protein receptor functionalized substrate. Generation of receptor configurations and execution of particle receptor rotations is detailed in *Chapter* 3. Target membrane proteins were represented as hard spheres with radius a_p = 10 nm that diffuse in 2D above the cell surface with surface area A_{cell} = 1 μm^2 and interact specifically with particle receptors as described previously. Particle ligand receptors are placed (a_p + δ) nm normal to the particle surface to prevent steric hindering of ligand-membrane protein binding. To interrogate varied particle receptor densities, s_{rec} on each particle was changed leading to various number densities of receptors on particles at different K_d. The receptor spacing used in each case and number density ranges are shown in Table 7.1. The particles are allowed to equilibrate above the surface for 5 x 10^5 MC steps and particle-cell surface separation, h, is then monitored for 2 x 10^7 steps. Histograms of h sampled, $p(h)$ are constructed and potentials of mean force, $W(h)$ are determined with a Boltzmann probability analysis as,[71, 111]

$$\frac{W(h)-W(h_0)}{kT} = -\ln\left(\frac{p(h)}{p(h_0)}\right) \tag{7.6}$$

where $W(h_0 = 100\text{ nm}) = 0\ kT$ was chosen as the reference state in each case. The number

of ligand-membrane protein bonds, N_b, was monitored in each step and histograms were constructed for each sampled binding valency. The fraction of bound particle configurations, where $N_b \geq 1$, was also monitored over the course of each simulation.

Table 7.1 Parameters used in MC Simulations for receptor spacing, s_{rec}, and range of receptor number densities, $N_{rec,}$ and average number density of receptors, $\langle N_{rec} \rangle$

s_{rec}/nm	N_{rec} range	$\langle N_{rec} \rangle$
30	100-104	102
20	225-235	230
10	900-940	923

7.4 Results and Discussion

7.4.1 Particle-Cell Surface Separations at Varied K_d

In Figure 2, the height of the particle above the cell surface, h, is shown as a function of MC step at a fixed membrane protein density representative of a cancerous cell ($\rho_{cell} = 256/\mu m^2$) and receptor spacing ($s_{rec} = 20$ nm) while varying K_d for the target protein. The dissociation constant was changed in each case by varying U_{min} in Eq. (7.1) from 1 – 10 kT in order to explore binding affinities in the μM to mM range suited for super-selective targeting. A linear color scale is included which shows the number of ligand-membrane protein bonds, N_b, present at each height to illustrate how these specific interactions affect heights sampled by the colloid above the surface. This helps to illustrate the relationship between binding of target membrane proteins and association of nanoparticles to the surface of the cell.

In Fig. 7When $K_d = 630$ μM (Fig. 7.2A), the ligands only interact weakly with the proteins on the cell surface ($u_{min} = 2\,kT$). As a result, the particle samples heights further from the surface as only a few bonds form transiently between the ligands and membrane proteins.

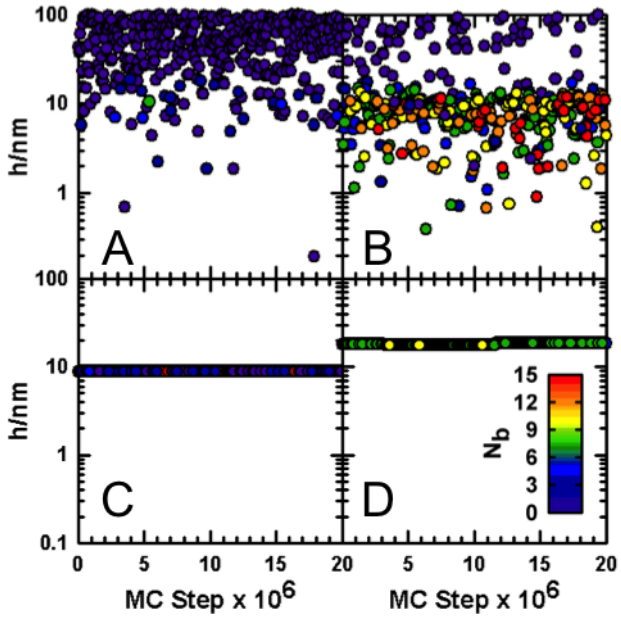

Figure 7.2 Sample trajectories of particle-cell surface separation, h versus step from MC simulations at ρ_{cell} = 256 μm^{-2} and (A) K_d = 630 μM, (B) K_d = 120 μM, (C) K_d = 14 μM (C), and K_d = 0.7 μM (D). Each data point has a linear color scale dependent upon the number of bridges formed in each step, N_b.

This contrasts with K_d = 120 μM (Fig. 7.2B) where ligands interact more strongly with the membrane proteins. This leads to stronger association with the surface of the cell and heights less than 10 nm are frequently sampled. Reversible association between the particle and cell surface is evident in this case as the ligand-membrane protein bonds formed vanish and h >> a_p are sampled. The ligand-membrane protein binding affinity was further increased and is shown in Fig. 7.2C with a K_d = 14 μM (u_{min} = 6 kT). While N_b fluctuates in this case, only a single height is sampled over the course of the simulation. This was also the case at K_d = 0.7 μM (u_{min} = 8 kT) shown in Fig. 7.2D. With ensembles of strong bridges present in each step, a very strong net particle-cell surface interaction is induced and the particle irreversibly associates with the surface of the cell. proteins (U_{min} = 4 kT) and form larger ensembles of bonds with the surface of the cell.

With the obtained distributions in height, net interaction potentials can be

determined provided adequate sampling of various h values. In the cases studied in this work, reversible particle-cell association was seen for $K_d < 40$ μM ($U_{min} < 5\ kT$) where a wide distribution of heights were sampled. When $K_d > 40$ μM, the particles irreversibly associated with the surface of the cell by only sampling limited distributions of h. Although effective particle-cell interaction potentials can be determined for these cases with methods shown in *Chapter 5*, it was not of interest in this study to quantitatively determine these potentials as they all will result in irreversible cell surface adhesion and the aim in this study is to demonstrate selectivity between cells with different membrane expression. In the next section, effective nanoparticle-cell interactions will be examined as a function of K_d and membrane protein density to further illustrate how sensitivity to specific cell surface protein expression levels can be designed in targeted nanoparticle vectors.

7.4.2 Particle-Cell Surface Interaction Potentials

In Figure 7.3, particle-cell surface interaction potentials are shown for fixed particle receptor spacing, ($s_{rec} = 20$ nm, $\langle N_{rec} \rangle = 230$), at 5 different membrane protein surface densities, ρ_{cell}, over a physiologically relevant range ($64/\mu m^2 - 256/\mu m^2$). Ligand-membrane protein mediated particle-cell surface interaction potentials are then determined at each ρ_{cell} for K_d ranging from 5200 μM – 40 μM to determine how affinity for the target membrane protein impacts the effective interaction of the particle with the cell.

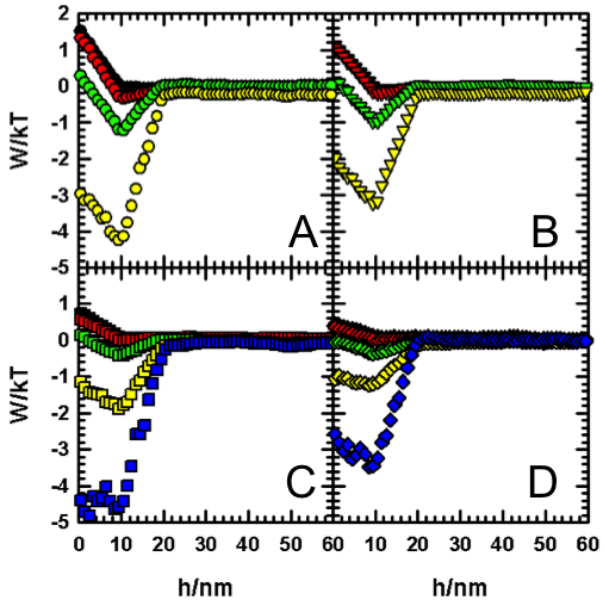

Figure 7.3 Particle-Cell Surface Interaction Potentials at (A) ρ_{cell} = 256 μm^2, (B) ρ_{cell} = 196μm^2, (C) ρ_{cell} = 100 μm^2, and (D) ρ_{cell} = 64 μm^2 and K_d = 5200 μM (black), K_d = 630 μM (red), K_d = 460 μM (green), and K_d = 120 μM (yellow) and) K_d = 40 μM (blue).

In Fig. 7.3A, net particle-cell interaction potentials are shown at ρ_{cell} = 256 μm^2 with 5200-120 μM. At K_d = 5200 μM and 630 μM (black and red circles), the particle has no net attractive interactions with the cell surface and at h < 10 nm, the particle has a net repulsive interaction with the cell surface. Repulsive interactions with the surface at h < a_p are due to hard sphere repulsive interactions between the membrane proteins with the particle and particle receptors when r < a_p in Eq. (7.1). At these low binding affinities (U_{min} from 1-2 kT), the effective particle-cell surface attraction generated by bonds formed is insignificant in comparison to the net repulsion due to the presence of hard spheres on the cell surface. When the affinity is increased to K_d = 460 μM and 120 μM (green and yellow circles), net attractive particle-cell interactions are induced once the receptors come within range of interacting with the membrane proteins at h < 20 nm. The

attractive well depth increases as a function of binding affinity as ensembles of ligand-membrane protein bonds form between the particle and the surface.

The expression of membrane proteins was decreased to measure these same particle-cell surface interactions with levels expected on healthy cells. In Figs.7.3B-D, net particle-cell interaction potentials were determined for membrane protein densities from 196/μm^2 – 64/μm^2, respectively. It is again seen at lower binding affinity cases with K_d = 5200 μM and 630 μM (black and red), no net attraction is generated as one would expect with lowered membrane protein densities. The net repulsion due to hard sphere interactions between the particle and particle receptors with the membrane proteins also decreases in strength as their density decreases on the surface. As the affinity increases to K_d = 460 μM and 120 μM, net attractive interactions are again induced with the magnitude of the attractive well depth decreasing with as the membrane protein decreases. In Fig. 7.3C-D, potentials are shown for K_d = 40 μM (U_{min} = 5 kT) as adequate sampling was obtained for these lower membrane protein densities. However, the attractive well depth for this case only decreases to ~3 kT at the lowest (healthy) cell expression levels shown which would still lead to significant association of the particle to the cell.

With varying surface densities of membrane proteins present on the surface of the cell, the interaction of the nanoparticle with the surface of the cell can change significantly dependent on the binding affinity between the ligand receptors and target membrane proteins. In order to introduce selectivity in targeted nanoparticle drug vectors, the interactions with the surface of the cell must vary from strong net attractive interactions with diseased cells to weak or ideally net repulsive interactions with healthy

cells. Of the cases shown in Fig. 7.3, net interactions were the most sensitive to membrane protein density at K_d = 120 μM with attractive well depths from ~4 kT at the highest membrane protein density to ~1 kT at the lowest membrane protein expression. By utilizing weak, reversible ligand-protein interactions, multi-valency on the particle scale can be introduced that allows for net particle-cell interactions that vary widely in strength. In the next sections, the influence of membrane expression levels and particle functionalization on particle-cell binding valency will be discussed to illustrate how it can be used to tailor these interactions for targeting specific cell types.

7.4.3 Particle-Cell Surface Binding Valency

To introduce selectivity for specific cell surfaces, ligand-membrane protein mediated interaction potentials can be tailored based on K_d and ρ_{cell} of the target membrane protein. Binding valency on the particle scale becomes an important factor in designing particles selective to specific membrane protein expression levels. For weaker affinity targets with K_d in μM range, multiple ligand-membrane protein bonds form in parallel to generate significant net particle-cell attraction as shown in Fig. 7.3. Figure 7.4 illustrates how this particle-cell binding valency varies over a range of K_d and ρ_{cell} for particles with $\langle N_{rec} \rangle$ = 230.

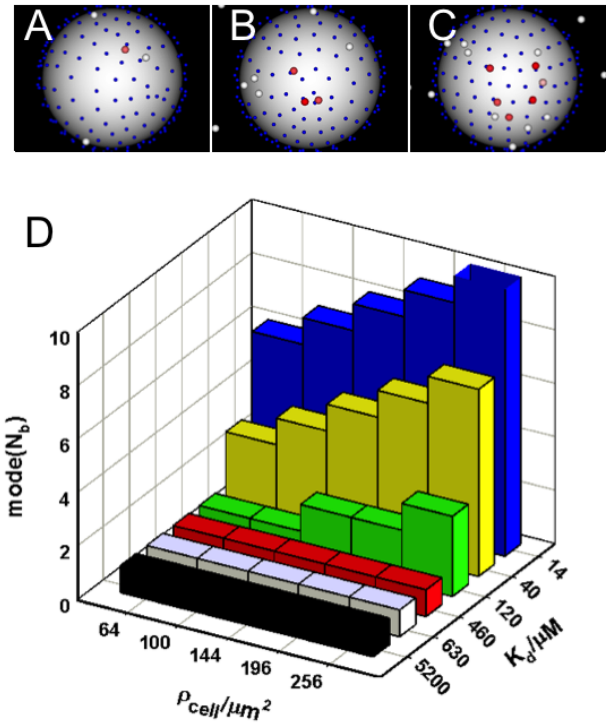

Figure 7.4 Representative snapshots with glass-bottom view from beneath nanoparticle with N_{rec}= 229 and (A) ρ_{cell} = 64/μm^2, (B) ρ_{cell} = 144/μm^2, and (C) ρ_{cell} = 256/μm^2 at K_d = 120 μM. Target membrane proteins have linear color scale depending on binding energy, U_{LPN}, ranging from white when unbound (U_{LPN} = 0) to red when tightly bound (U_{LPN} = U_{min}). (D) Mode valency of surface-bound nanoparticle configurations as a function of K_d and ρ_{cell}.

In Fig. 7.4A-C, representative snapshots are shown from below the particle to show the number of bonds present with K_d = 120 μM and N_{rec} = 229 at varied ρ_{cell}. The glass-bottom view of the particle above the cell surface helps to visualize how particle-cell binding valency changes at each membrane surface density. For each membrane protein (small spheres), a linear color scale is used to indicate ligand-protein binding energy, U_{LPN}, where particles turn from white when unbound (i.e. U_{LPN} = 0) to red when tightly bound (i.e. U_{LPN} = U_{min}). When ρ_{cell} = 64/μm^2 shown in Fig. 7.4A, only a single bond is present with between the particle and cell surface. When ρ_{cell} = 144/μm^2 shown in

Fig. 7.4B, multi-valent particle-cell binding is seen with 3 ligand-protein bonds formed simultaneously. Particle-cell binding valency further increases at $\rho_{cell} = 256/\mu m^2$, shown in Fig 7.4C, with 6 bonds present. The binding energy of each bond formed also varies in magnitude and is clearly shown in each case with the U_{LPN} color scale in Fig. 7.4. The number of bonds and distribution of bond energies will ultimately determine the net interaction induced between the particle and surface.

In Figure 7.4D, the mode of the particle-cell binding valency from all bound particle configurations is shown as a function of K_d and ρ_{cell} for more quantitative comparison. For the weakest binding affinities with K_d from 5200 μM - 460 μM, the particle-cell interactions are largely monovalent which explains the weak net particle-cell interactions seen in Fig. 7.3. At $K_d = 120$ μM, particle-cell binding valency transitions from monovalent binding at low membrane protein densities to multi-valent binding at higher membrane protein densities. This shift in binding valency explains the sensitivity of the net particle-cell interactions to ρ_{cell} seen in Fig. 7.3. Multi-valent binding occurs at all $K_d > 120$ μM on each cell surface independent of membrane protein density. With multi-valent particle-cell binding at both healthy and diseased membrane protein expression levels, net attractive interactions will be present at all cell surfaces and selectivity will be lost.

The valency of particle-cell binding can also be tuned by changing the density of ligands, N_{rec}, functionalized on the nanoparticle. This design parameter allows us to engineer nanoparticles to selectively bind to cells given a specific K_d and ρ_{cell}. We demonstrate this for a target membrane protein with a specific K_d and ρ_{cell} varied from $64/\mu m^2$ (healthy cells) to $256/\mu m^2$ (diseased cells) with nanoparticles functionalized with

varying amounts of ligands. Fig. 7.5 visualizes changes in valency for each N_{rec} investigated in Fig. 7.5A-C with quantitative comparison of all cases in Fig. 7.5D.

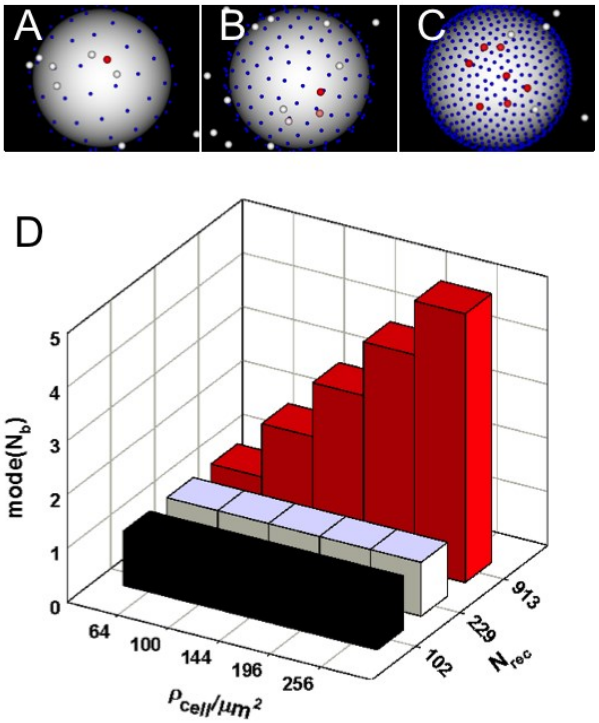

Figure 7.5 Representative snapshots with glass-bottom view from beneath nanoparticle with (A) N_{rec} = 102, (B) N_{rec} = 229, and (C) N_{rec} = 913 at ρ_{cell} = 256/μm^2 and K_d = 460 μM. Target membrane proteins have linear color scale depending on binding energy, U_{LPN}, ranging from white when unbound (U_{LPN} = 0) to red when tightly bound (U_{LPN} = U_{min}). (D) Mode valency of surface-bound nanoparticle configurations as a function of K_d and $\langle N_{rec} \rangle$.

In Fig. 7.5A-C, representative snapshots are shown again below the particle with a linear color scale of U_{LPN} for all membrane proteins for an example case with ρ_{cell} = 256/μm^2 and K_d = 460 μM. When N_{rec} = 102 shown in Fig. 7.5A, only a single bond is present between the particle and cell surface. When N_{rec} increased to 229 shown in Fig. 7.5B, multi-valent bonding is seen with 2 ligand-membrane protein bonds present. When

N_{rec} is further increased to 913 in Fig. 7.5C, 7 membrane proteins are tightly bound to particle lignad receptors. This shows how changes in nanoparticle design (i.e surface functionality) can impact the particle-cell binding valency and as a result, the effective particle-cell interactions will change dependent upon membrane protein expression.

In Fig. 7.5D, we examine the effects of nanoparticle ligand receptor density on particle-cell binding valency with diseased cells (ρ_{cell} = 256/μm^2) for the example cases discussed in Fig. 7.5A-C. With N_{rec} = 102 and N_{rec} = 229, the particle only binds monovalently with the cell surface at all target membrane protein densities. At N_{rec} = 913, we begin to see multi-valent binding that increases as a function of membrane protein density. As ligand-membrane protein binding is highly reversible at such high K_d, larger numbers of ligands must be present for multiple bonds to be formed simultaneously. These results illustrate how binding valency can be tuned with particle design and in the next section, the effects of particle design on selectivity for specific target membrane proteins will be discussed.

7.4.4 Selectivity for Diseased Versus Healthy Cells

In order to design super-selective nanoparticle drug carriers, the ligand receptor density must be carefully chosen to effectively tune the net particle-cell interactions to diseased cells with abnormal expression levels while also having very weak or ideally a net repulsive interaction with the surface of healthy cells. In this work, the fraction of surface-bound particle configurations (i.e. when $N_b \geq 1$), χ, was used as a measure of selectivity. In Fig. 7.6, we show how χ changes for 4 different target membrane proteins by varying K_d and 3 different nanoparticle designs by varying N_{rec}.

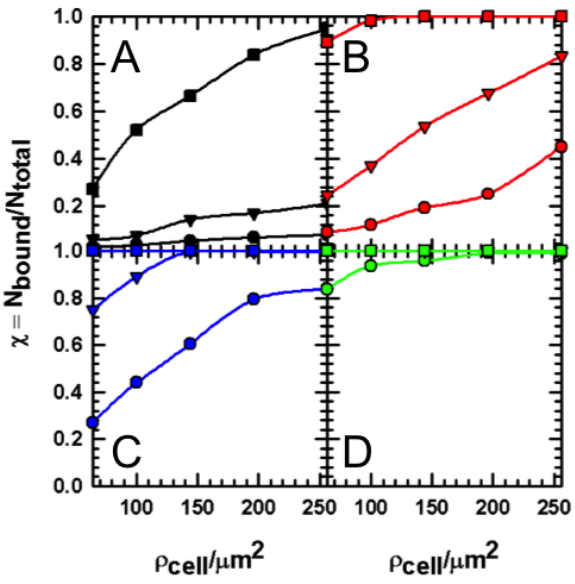

Figure 7.6 Fraction of particle configurations bound to cell surface, χ, versus ρ_{cell} at K_d = 630 μM (black), K_d = 460 μM (red), and K_d= 120 μM (blue) and K_d = 40 μM (green) with $\langle N_{rec} \rangle$ = 102 (circles), $\langle N_{rec} \rangle$ = 230 (triangles down), and $\langle N_{rec} \rangle$ = 923 (squares).

With $\langle N_{rec} \rangle$ = 102 (circles) and $\langle N_{rec} \rangle$= 230 (triangles down), only a small fraction of particle configurations were bound to the cell surfaces with $\chi < 0.2$ at all levels of membrane protein expression. As was discussed in the last section for this case, the number of ligands present was much too low to show multi-valent binding and as a result, only weak effective particle-cell interactions can be induced for these expression levels. At $\langle N_{rec} \rangle$ = 923 (squares), the fraction of bound particles increases dramatically from χ = 0.28 at healthy cells with $\rho_{cell} = 64/\mu m^2$ to $\chi = 0.95$ at diseased cells with $\rho_{cell} = 256/\mu m^2$. It was this case in Figure 7.5D that showed multi-valent particle cell binding in response to changes in ρ_{cell} and as a result, it shows the most selective binding to cell surfaces with high membrane protein expression.

Target membrane proteins with higher binding affinity were also investigated with K_d = 120 μM shown in Fig 7.6B and K_d = 40 μM shown in Fig. 7.6C. In these cases, the most selective binding was seen at $\langle N_{rec} \rangle$ = 230 for K_d = 120 μM and $\langle N_{rec} \rangle$ = 102 for K_d = 40 μM. At an even higher binding affinity with K_d = 120 μM shown in Fig 7.6D, the particle was only weakly selective at $\langle N_{rec} \rangle$ = 102 with χ = 0.85 at healthy cells with ρ_{cell} = 64/μm^2 to χ = 1.0 at diseased cells with ρ_{cell} = 256/μm^2. These results show how particle design could be directed to engineer super-selective nanoparticles given a specific K_d of target membrane protein and range of ρ_{cell} for diseased versus healthy cells. Using target proteins with μM-range K_d, particle-cell interactions can be further optimized by modifying the amount of ligand receptors immobilized to the nanoparticle surface.

7.5 Conclusions

In this work, nanoparticle interactions with the surface of cells mediated by specific binding to target membrane proteins was investigated using Monte Carlo Simulations with realistic, experimentally verified binding affinities and membrane protein expression levels. By measuring interactions of nanoparticles with both diseased cells having abnormal over-expression of target proteins and healthy cells expressing normal levels of target proteins, our results show that multi-valent nanoparticle-cell binding mediated by weak, reversible ligand-membrane protein interactions proved the most effective means to discriminate between healthy and diseased cell surfaces. While higher binding affinity targets (K_d < 1 nM) are attractive due to their specificity for target membrane proteins, they are most appropriate when only sparse amounts are present on healthy cells which is not always the case for diseases like cancer where abnormal

expression is common. Using lower affinity ligands ($K_d \approx 1$ μM – 1 mM) to target for diseased cells with marked overexpression of target membrane proteins, nanoparticles can be designed with the requirement of multi-valency on the nanoparticle scale to induce adhesion only at diseased cell surfaces. With this model, informed design choices for targeted nanoparticle drug delivery vectors can be made to maximize selectivity for specific diseased cell populations. In future work, comparisons between the interactions determined using this computational model and experimental measurements of particle-cell interactions in *Chapter 6* will help to identify additional parameters to improve the accuracy of the model.

8. CONCLUSIONS

The primary goal of this research is to combine experimental measurements made using diffusing colloidal probe microscopy (DCPM) with Monte Carlo (MC) simulation techniques to allow for more in-depth analysis of specific and non-specific biomacromolecular interactions at colloidal and live cell surfaces. DCPM has proven an effective means to make quantitative, sensitive measurements of weak, specific biomacromolecular interactions[72, 127, 215] and to image free energy landscapes of patterned interfaces (analogous to cell seeded substrates).[69] In this work, DCPM was used to measure colloidal interactions mediated by competitive protein-carbohydrate interactions. Additionally, image analysis techniques were developed to extend the use of DCPM for measuring specific and nonspecific biomacromolecular interactions with the surface of live cells. MC simulations have been used extensively to study biological and colloidal systems.[77, 216, 152, 163] Models of colloidal and surface interactions mediated by specific biomolecular binding were developed to further interpret these experimental results.

This work began with the sugar-binding protein, Concanavalin A (ConA), where colloidal association dynamics were measured in quasi-2D concentrated dispersions of dextran-modified colloidal particles in the presence of ConA and glucose. Specific adsorption of ConA was visualized with fluorescent assays to determine how competitive ConA-glucose interactions affected the amount of ConA surface adsorption. Aggregation kinetics were reversibly tuned by varying ConA and glucose over a range of concentrations on the order of each constituent dissociation constant. A secondary stability ratio analysis then relates net particle-particle interactions to initial aggregation kinetics in these dispersions as a function of ConA and glucose concentration.

To model this system, receptor-ligand mediated colloidal potentials of mean force were measured using MC Umbrella Sampling Simulations. Initial results focused on characterization of biomacromolecular interactions in the bulk and at interfaces which lead to development of an additional theoretical formalism to predict dissociation constants for a wide range of input receptor-ligand interaction potentials. With the dissociation constant and ligand size as inputs, colloidal potentials of mean force could then be determined for with parameters representative of the ConA-Dextran system. These results demonstrated how freely diffusing ConA nanospheres could adsorb to the surface of dextran-decorated colloids and induce net particle-particle attraction by formation of ensembles of ConA-dextran bridges. While our results were focused on this particular system, the model could be easily applied to a number of related biomacromolecular systems.

Next, diffusing colloidal probe microscopy was further developed for measurement of specific and non-specific interactions with the surface of live cells. Novel dark field imaging and particle-cell image analysis techniques allow for the direct, quantitative measurement of cell surface interactions. The diffusion of particles on the surface of cells was used to determine lateral diffusion rates on the cell, association lifetimes to the cell surface, and particle-cell surface interaction potentials. A variety of particle surface coatings relevant to drug delivery, biosensing and tissue engineering were investigated to determine their impact on net particle-cell surface interactions. The results from this work demonstrate for the first time how measurements of colloid-cell surface interactions can be made using diffusing colloidal probes.

Using the principles developed in *Chapter 5* to model colloids and biomacromolecules, nanoparticle interactions with the surface of cells mediated by specific binding to target membrane proteins was investigated using MC simulations. Realistic, experimentally verified binding affinities and membrane protein expression levels were input to determine the selectivity of specific nanoparticle designs for certain cell types (diseased or healthy). By measuring interactions of nanoparticles with both diseased cells having abnormal over-expression of target proteins and healthy cells expressing normal levels of target proteins, our results show that multi-valent nanoparticle-cell interactions mediated by weak, reversible ligand-membrane protein binding proved the most effective means to discriminate between healthy and diseased cell surfaces. Using lower affinity ligands to target for diseased cells with marked overexpression of target membrane proteins, nanoparticles can be designed with the requirement of multi-valency on the nanoparticle scale to induce adhesion to the cell surface leading to much improved selectivity for specific cell populations. With this model, experimental measurements of cell surface interactions can be further interpreted with realistic biological parameters.

The work in this dissertation aimed to develop (1) quantitative models of colloidal interactions mediated by biospecific interactions and (2) further extend DCPM to measure colloid and cell surface interactions mediated by specific and non-specific macromolecular interactions. Kinetic assays of colloidal association allow for dynamic and equilibrium characterization of particle-particle interactions mediated by weak, specific binding between proteins and carbohydrates. Weak, specific protein-carbohydrate and non-specific interactions were also studied for their impact on colloidal

interactions with the surface of cells. The experimental and computational techniques used in this work could be applied to study a variety of colloidal systems and biomolecules with relevance to fundamental biology and biomedical applications. In future work, comparisons between the interactions determined using the computational models and experimental measurement techniques developed in this dissertation will help in rational design of functionalized colloids and in identifying additional parameters to improve the accuracy of these models.

9. FUTURE RESEARCH

9.1 Association Dynamics of HA-Coated SiO_2 Colloids with Soluble CD44 and HA

In *Chapter 4*, the aggregation kinetics of colloids mediated by ConA-dextran interactions was investigated. The initial doublet formation rate was then also related to net particle-particle interactions. To probe CD44-HA interactions measured on MDA-MB-231 (MDA231) epithelial breast cancer cells in *Chapter 6*, soluble CD44 could be obtained with immunoprecipitation techniques[214] from MDA231 cells and association dynamics could be measured in quasi-2D concentrated dispersions of HA coated colloids, as shown in Fig. 9.1A. Soluble HA of different molecular weight could be added as a competitor which is illustrated in Fig. 9.1B to inhibit CD44-HA mediated particle-particle binding. These could be used as complementary measurements to those on actual cell surfaces to compare particle-particle interactions with different amounts of soluble HA. It is believed soluble HA production by metastatic cancer cells such as MD231 cells could facilitate invasiveness[10] and this assay could prove as a useful tool to study how competitive HA interactions could weaken cell-extracellular matrix adhesion.

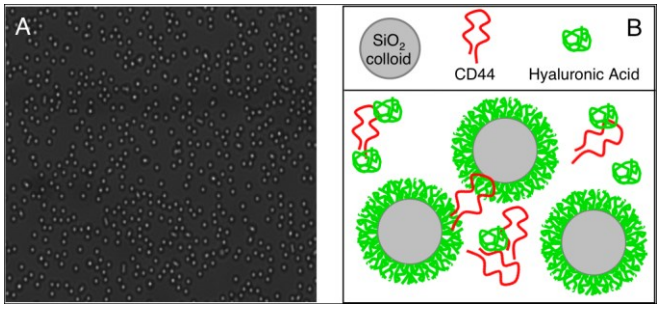

Fig 9.1 (A) Video microscopy image of Quasi-2D concentrated dispersion of HA coated silica particles on F108 coated substrate. (B) Schematic of CD44-HA mediated colloidal interactions.

9.2 Dextran/HA Hybrid SiO_2 Colloids Interacting with Cancerous MDA-MB-231 and Healthy MCF-10A Cells

For super-selective targeted drug vectors, we demonstrated in *Chapter 7* that changes in multi-valent particle cell interactions could help make particles selective only for diseased cells. In *Chapter 6*, strong net particle-cell surface interactions were induced by HA-coated silica particles due to specific CD44-HA interactions. Dextran coated colloidal silica only showed weak net attractive interactions with the cell surface. To control particle-cell binding valency, mixed hybrid coatings of dextran and HA could be used to modulate the net particle-cell interactions. Using the modeling tools developed in *Chapter 7* as a guide, different surface coverages could be interrogated and their interactions could be measured on cancerous MDA231 and healthy MCF-10A epithelial breast cancer cells where marked overexpression of CD44 is expected on cancerous cells.[177]

In Figure 9.2, some preliminary results on making hybrid dextran-HA coatings and their interactions with MDA231 cells are shown. To make the hybrid layer, polymer mixtures of dextran and HA are made and used to coat epoxy-silane modified silica particles. To determine if this produced hybrid layers, the particles were stained with FITC-ConA which only binds specifically to dextran. For 1% HA/dextran shown in Figure 9.2A, a large amount of ConA adsorbed to the particle and a large decrease in the amount of ConA adsorbed to the surface indicating a decrease in the amount of dextran present on the 10% HA / 90% Dextran coated silica. While the exact amounts of dextran and HA cannot be determined from this assay, it is clear this synthesis scheme is able to produce hybrid layers. The amount adsorbed at 10% HA / 90% dextran is very similar to the 100% HA case which could be due to steric screening of the dextran chains by the

large HA present with a molecular weight of 1 MDA ($R_g \approx 100$ nm).

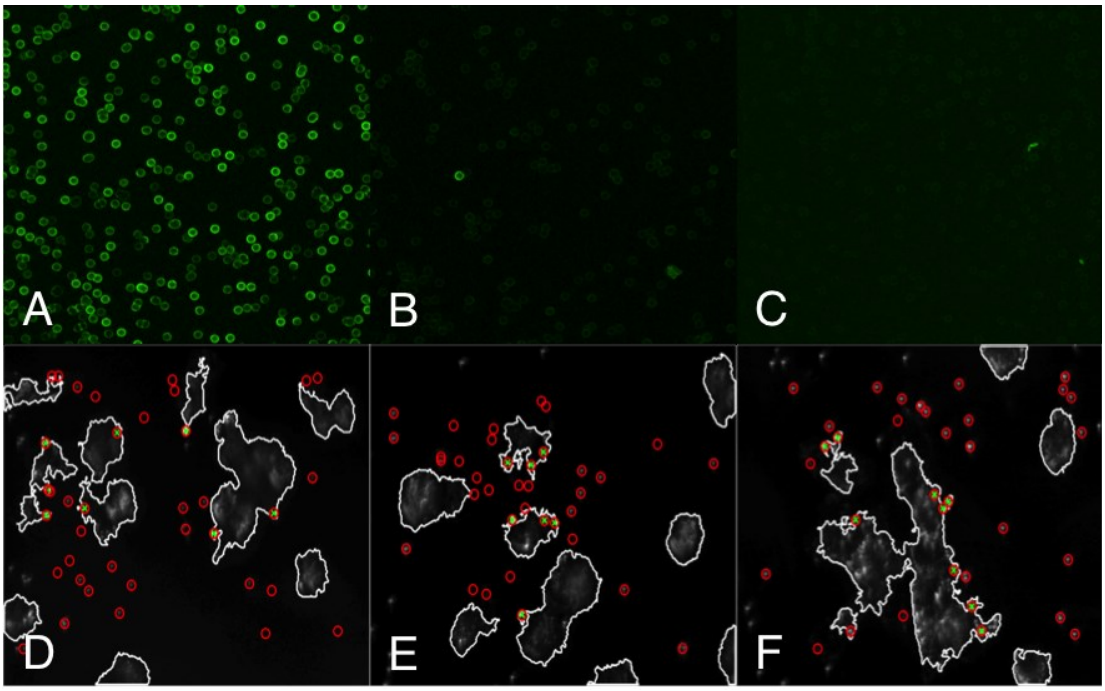

Fig 9.2 Fluorescent confocal microscopy images of (A) 1% HA/99% Dextran, (B) 10% HA / 90% Dextran and (C) 100% HA coated silica particles in 10 μM FITC-ConA. MATLAB analysis of dark field microscopy images of (A) 1% HA-Dextran, (B) 10% HA-Dextran and (C) 100% HA coated silica particles interacting with MDA-MB-231 cells.

The interactions of these hybrid particles with MDA231 cells were tested with dark field video microscopy and are shown in Figure 9.2D-F. These preliminary results showed a reduction in particle-cell surface association with less irreversibly bound particles on the MDA231 cell surface. However, many particles non-specifically adhered to the background HA-substrate which is not ideal when probing specific CD44-HA interactions on the cell. Future work will aim to optimize the hybrid HA/dextran coating protocol and test these hybrid particles with healthy MCF10A cells to see how the net particle-cell interactions are affected. Experimental results will be compared with those found through modeling to find additional parameters that could improve its accuracy.

9.3 Gold Nanoparticle Interactions With MDA-MB-231 Cells

Dark field scattering on metallic colloids is greatly enhanced to due local surface plasmon resonance effects. For gold nanoparticles, the enhancement of scattering intensities allows for imaging of diffraction-limited particles with sizes ranging from 10-100 nm. Particles in this size range would allow for both particle dynamics on the surface and intracellular transport upon uptake via endocytosis to be studied. Figure 9.3 shows some preliminary studies how changes in particle composition can lead to changes in net-particle cell interactions. In Fig. 9.3A, the mean squared displacement is shown for PEG-coated 400 nm colloidal gold on (green circles) and off (red circles) the MDA231 cell surface and it is clear the diffusion drastically hindered on the surface of the cell. While PEG-coated silica was highly stable on MDA231 cells, increases in van der Waals attraction could lead to nonspecific adhesion for gold nanoparticles. Figure 9.3B shows a 2D free energy landscape that helps to visualize the location and strength of adhesion showing that strong adhesion was most prevalent near the cell surface. Future work will interrogate to characterize intracellular transport of smaller 100 nm gold.

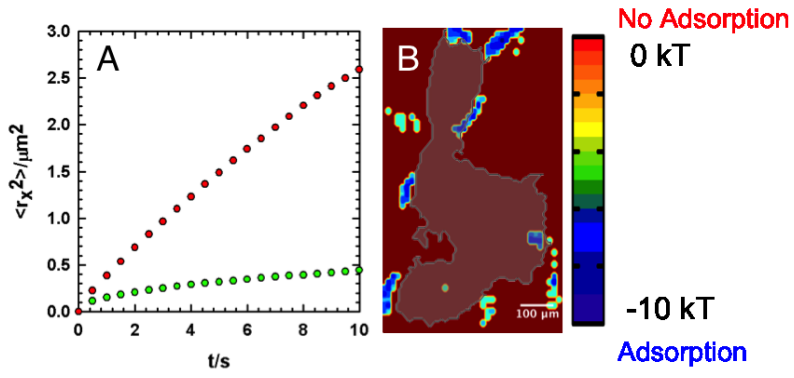

Fig 9.3 Mean squared displacement of 400 nm F108-coated gold nanoparticles on (green) and off (red) MDA231 cell surface. Two dimensional free energy landscape of 400 nm F108-coated gold nanoparticles on MDA231 cells (outlined black and shaded).

9.4 Measuring Cell Topography With Diffusing Colloidal Probes

In *Chapter 6*, diffusing colloidal probe measurements were used to measure specific and non-specific macromolecular interactions with live cell surfaces. For PEG-coated silica particles, particle-cell surface distance potentials of mean force, $W(r)$, showed repulsion at $r < 0$ believed to be due to gravitational effects from cell morphology. In order to further investigate this effect, smaller colloidal particles able to make larger height excursions to probe the height of the entire surface of the cell can be used. In Figure 9.4, we show some preliminary results from PEG-coated, fluorescently-labeled, 800 nm silica particles interacting with MDA231 cells. Fluorescent particles are used here to allow for fluorescent confocal microscopy imaging. Confocal microscopy also allows for 3D imaging which will be useful in verifying the heights particles samples on the cell surface.

In Figure 9.4A, confocal images from XY scans were taken of the colloidal particles on MDA231 cells. The particles (green spheres) were highly concentrated so that the entire surface could be sampled. The MDA231 cells are not stained but can be clearly seen as the dark regions where less particles have diffused. To relate the 2D positions sampled by each particle can be related to the topography, an inverse Boltzmann analysis can be used to convert a 2D (x,y) coordinate probability distributions to a 2D (x,y) coordinate free energy landscape. This landscape could then be interpreted as a measure of gravitational potential energy and the height on the cell at each position could be measured. Compared to typical techniques such as atomic force microscopy for measuring surface topography, this would allow for a less intrusive, higher throughput method to determine cell topography.

To verify the heights determined on cells, XZ scans of the sample, shown in Fig. 9.4B, could be used to visualize areas on the cell where the particles have “jumped”. It

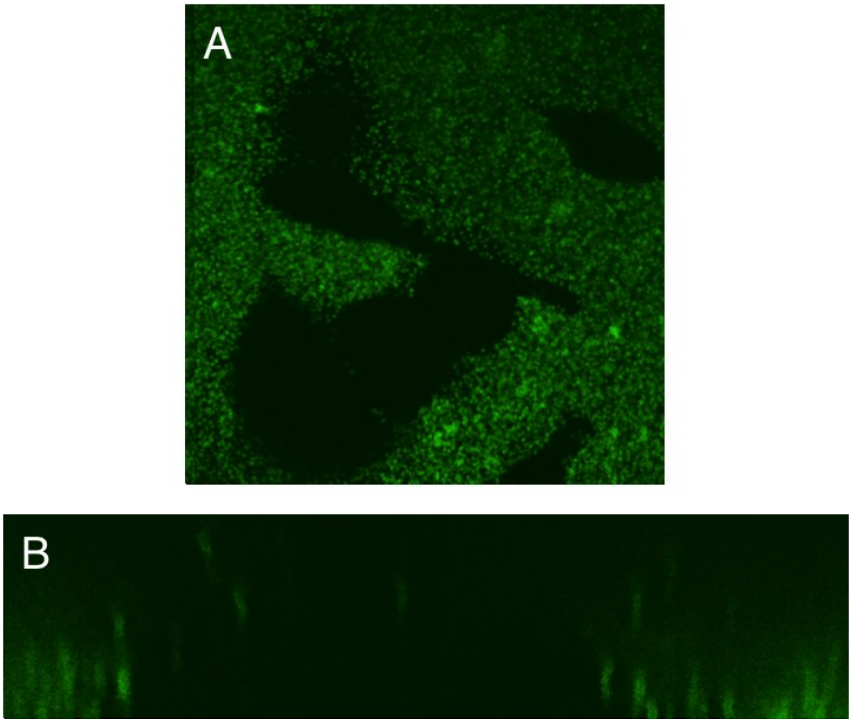

Fig 9.4 (A) XY and (b) XZ Scans from Fluorescent Confocal Microscopy for FITC-labeled 800 nm silica particles diffusing on MDA231 cells (dark regions).

can be seen in Fig. 9.4B that the particles are able to sample higher positions on the cell due to their smaller size. These XZ scans can be taken very rapidly compared to 3D confocal imaging via XYZ stacks allowing for single nanoparticles to be resolved. Future work will also include fluorescent imaging of the MDA231 cells to directly verify their topography. Particle-particle interactions will also need to be considered for appropriate handling of the measured 2D (x,y) coordirnate probability distributions and sedimentation equilibrium observed from XZ scans.

REFERENCES

1. Flemming, H.-c.; Wingender, J. The biofilm matrix. *Nature reviews. Microbiology* **2010,** *8*, 623-33.
2. Diggle, S. P.; Stacey, R. E.; Dodd, C.; Cámara, M.; Williams, P.; Winzer, K. The galactophilic lectin, LecA, contributes to biofilm development in Pseudomonas aeruginosa. *Environmental ...* **2006,** *8*, 1095-1104.
3. Stratford, M. Yeast flocculation: reconciliation of physiological and genetic viewpoints. *Yeast (Chichester, England)* **1992,** *8*, 25-38.
4. Goossens, K.; Willaert, R. Flocculation protein structure and cell-cell adhesion mechanism in Saccharomyces cerevisiae. *Biotechnology letters* **2010,** *32*, 1571-1585.
5. Verstrepen, K. J.; Derdelinckx, G.; Verachtert, H.; Delvaux, F. R. Yeast flocculation: what brewers should know. *Applied microbiology and biotechnology* **2003,** *61*, 197-205.
6. Alon, R.; Ley, K. Cells on the run: shear-regulated integrin activation in leukocyte rolling and arrest on endothelial cells. *Current opinion in cell biology* **2008,** *20*, 525-32.
7. Vicente-Manzanares, M.; Choi, C. K.; Horwitz, a. R. Integrins in cell migration - the actin connection. *Journal of Cell Science* **2009,** *122*, 1473-1473.
8. McEver, R. P. Selectin-carbohydrate interactions during inflammation and metastasis. *Glycoconjugate journal* **1997,** *14*, 585-91.
9. Lasky, L. A. Interpreters of Selectins : Cell-Specific Carbohydrate Information During Inflammation. *Science* **1992,** *258*, 964-969.
10. Zöller, M. CD44: can a cancer-initiating cell profit from an abundantly expressed molecule? *Nature reviews. Cancer* **2011,** *11*, 254-67.
11. Toole, B. P. Hyaluronan: from extracellular glue to pericellular cue. *Nature reviews. Cancer* **2004,** *4*, 528-539.
12. Zeng, X.; Andrade, C. A. S.; Oliveira, M. D. L.; Sun, X.-L. Carbohydrate–protein interactions and their biosensing applications. In *Analytical and Bioanalytical Chemistry*, 2012; Vol. 402, pp 3161-3176.
13. Scarano, S.; Mascini, M.; Turner, A. P. F.; Minunni, M. Surface plasmon resonance imaging for affinity-based biosensors. *Biosensors & bioelectronics* **2010,** *25*, 957-966.
14. Jelinek, R.; Kolusheva, S. Carbohydrate biosensors. *Chemical reviews* **2004,** *104*, 5987-6015.
15. Homola, J. Present and future of surface plasmon resonance biosensors. *Analytical and bioanalytical chemistry* **2003,** *377*, 528-539.
16. Hilt, J. Z.; Byrne, M. E. Configurational biomimesis in drug delivery: Molecular imprinting of biologically significant molecules. In *Advanced Drug Delivery Reviews*, 2004; Vol. 56, pp 1599-1620.
17. Bareford, L. M.; Swaan, P. W. Endocytic mechanisms for targeted drug delivery. In *Advanced Drug Delivery Reviews*, 2007; Vol. 59, pp 748-758.
18. Cho, K.; Wang, X.; Nie, S.; Chen, Z. G.; Shin, D. M. Therapeutic nanoparticles for drug delivery in cancer. *Clinical cancer research : an official journal of the American Association for Cancer Research* **2008,** *14*, 1310-1316.

19. Yamazaki, N.; Kojima, S.; Bovin, N. V.; André, S.; Gabius, S.; Gabius, H. J. Endogenous lectins as targets for drug delivery. In *Advanced Drug Delivery Reviews*, 2000; Vol. 43, pp 225-244.
20. Smart, J. D. Lectin-mediated drug delivery in the oral cavity. In *Advanced Drug Delivery Reviews*, 2004; Vol. 56, pp 481-489.
21. Minko, T. Drug targeting to the colon with lectins and neoglycoconjugates. In *Advanced Drug Delivery Reviews*, 2004; Vol. 56, pp 491-509.
22. Schurr, J. M. Dynamic light scattering of biopolymers and biocolloids. *CRC critical reviews in biochemistry* **1977,** *4*, 371-431.
23. Misra, P.; Dubinskii, M. A. *Ultraviolet spectroscopy and UV lasers*; CRC Press2002.
24. Aslan, K.; Lakowicz, J. R.; Geddes, C. D. Nanogold plasmon resonance-based glucose sensing. 2. Wavelength-ratiometric resonance light scattering. *Anal Chem* **2005,** *77* (7), 2007-14.
25. Aslan, K.; Lakowicz, J. R.; Geddes, C. D. Nanogold-plasmon-resonance-based glucose sensing. *Analytical biochemistry* **2004,** *330*, 145-55.
26. Barone, P. W.; Strano, M. S. Reversible Control of Carbon Nanotube Aggregation for a Glucose Affinity Sensor. *Angewandte Chemie* **2006,** *118*, 8318-8321.
27. Otsuka, H.; Akiyama, Y.; Nagasaki, Y.; Kataoka, K. Quantitative and Reversible Lectin-Induced Association of Gold Nanoparticles Modified with α-Lactosyl-ω-mercapto-poly(ethylene glycol). *Journal of the American Chemical Society* **2001,** *123*, 8226-8230.
28. Axelrod, D. Chapter 7: Total internal reflection fluorescence microscopy. *Methods in cell biology* **2008,** *89*, 169-221.
29. Homola, J.; Yee, S. S.; Gauglitz, G. Surface plasmon resonance sensors: review. *Sensors and Actuators B-Chemical* **1999,** *54* (1-2), 3-15.
30. Wang, Y.; Gildersleeve, J. C.; Basu, A.; Zimmt, M. B. Photo- and biophysical studies of lectin-conjugated fluorescent nanoparticles: reduced sensitivity in high density assays. *The journal of physical chemistry. B* **2010,** *114*, 14487-94.
31. Vedala, H.; Chen, Y.; Cecioni, S.; Imberty, A.; Vidal, S.; Star, A. Nanoelectronic detection of lectin-carbohydrate interactions using carbon nanotubes. *Nano letters* **2011,** *11*, 170-5.
32. Smith, E. a.; Thomas, W. D.; Kiessling, L. L.; Corn, R. M. Surface plasmon resonance imaging studies of protein-carbohydrate interactions. *Journal of the American Chemical Society* **2003,** *125*, 6140-8.
33. Liang, P.-H.; Wang, S.-K.; Wong, C.-H. Quantitative analysis of carbohydrate-protein interactions using glycan microarrays: determination of surface and solution dissociation constants. *Journal of the American Chemical Society* **2007,** *129*, 11177-84.
34. Munoz, E. M.; Correa, J.; Riguera, R.; Fernandez-Megia, E. Real-time evaluation of binding mechanisms in multivalent interactions: a surface plasmon resonance kinetic approach. *Journal of the American Chemical Society* **2013,** *135*, 5966-9.
35. Wang, W.; Wang, S.; Liu, Q.; Wu, J.; Tao, N. Mapping single-cell-substrate interactions by surface plasmon resonance microscopy. *Langmuir : the ACS journal of surfaces and colloids* **2012,** *28*, 13373-9.

36. Wang, Z.; Tiruppathi, C.; Minshall, R. D.; Malik, A. B. Size and dynamics of caveolae studied using nanoparticles in living endothelial cells. *ACS nano* **2009,** *3*, 4110-6.
37. Lisse, D.; Richter, C. P.; Drees, C.; Birkholz, O.; You, C.; Rampazzo, E.; Piehler, J. Monofunctional stealth nanoparticle for unbiased single molecule tracking inside living cells. *Nano Lett* **2014,** *14* (4), 2189-95.
38. Langdon, B. B.; Kastantin, M.; Walder, R.; Schwartz, D. K. Interfacial Protein-Protein Associations. *Biomacromolecules* **2013**.
39. Guo, S.-M.; Bag, N.; Mishra, A.; Wohland, T.; Bathe, M. Bayesian Total Internal Reflection Fluorescence Correlation Spectroscopy Reveals hIAPP-Induced Plasma Membrane Domain Organization in Live Cells. *Biophysical journal* **2014,** *106*, 190-200.
40. Ewers, H.; Smith, A. E.; Sbalzarini, I. F.; Lilie, H.; Koumoutsakos, P.; Helenius, A. Single-particle tracking of murine polyoma virus-like particles on live cells and artificial membranes. *Proceedings of the National Academy of Sciences of the United States of America* **2005,** *102*, 15110-5.
41. Müller, D. J.; Dufrêne, Y. F. Atomic force microscopy: a nanoscopic window on the cell surface. *Trends in cell biology* **2011,** *21*, 461-9.
42. Katan, A. J.; Dekker, C. High-speed AFM reveals the dynamics of single biomolecules at the nanometer scale. *Cell* **2011,** *147*, 979-82.
43. Francis, L. W.; Lewis, P. D.; Wright, C. J.; Conlan, R. S. Atomic force microscopy comes of age. *Biology of the cell / under the auspices of the European Cell Biology Organization* **2010,** *102*, 133-43.
44. Raman, a.; Trigueros, S.; Cartagena, a.; Stevenson, a. P. Z.; Susilo, M.; Nauman, E.; Contera, S. A. Mapping nanomechanical properties of live cells using multi-harmonic atomic force microscopy. *Nature nanotechnology* **2011,** *6*, 809-14.
45. Dufrêne, Y. F.; Martínez-Martín, D.; Medalsy, I.; Alsteens, D.; Müller, D. J. Multiparametric imaging of biological systems by force-distance curve-based AFM. *Nature methods* **2013,** *10*, 847-54.
46. Kirmizis, D.; Logothetidis, S. Atomic force microscopy probing in the measurement of cell mechanics. *International journal of nanomedicine* **2010,** *5*, 137-45.
47. El Kirat, K.; Morandat, S.; Dufrêne, Y. F. Nanoscale analysis of supported lipid bilayers using atomic force microscopy. *Biochimica et biophysica acta* **2010,** *1798*, 750-65.
48. Zhu, C.; Lou, J.; McEver, R. P. Catch bonds: physical models, structural bases, biological function and rheological relevance. *Biorheology* **2005,** *42* (6), 443-62.
49. Zhang, W.; Stack, A. G.; Chen, Y. Interaction force measurement between E. coli cells and nanoparticles immobilized surfaces by using AFM. *Colloids and surfaces. B, Biointerfaces* **2011,** *82*, 316-24.
50. Xu, L.-C.; Logan, B. E. Interaction forces measured using AFM between colloids and surfaces coated with both dextran and protein. *Langmuir : the ACS journal of surfaces and colloids* **2006,** *22*, 4720-7.
51. Vasir, J. K.; Labhasetwar, V. Quantification of the force of nanoparticle-cell membrane interactions and its influence on intracellular trafficking of nanoparticles. *Biomaterials* **2008,** *29*, 4244-52.

52. Roiter, Y.; Ornatska, M.; Rammohan, A. R.; Balakrishnan, J.; Heine, D. R.; Minko, S. Interaction of nanoparticles with lipid membrane. *Nano letters* **2008,** *8*, 941-4.
53. Ritchie, K.; Kusumi, A. Single molecule probe scanning optical force imaging microscope for viewing live cells. *Journal of Biological Physics* **2002,** *28* (4), 619-626.
54. Nishizaka, T.; Seo, R.; Tadakuma, H.; Kinosita, K.; Ishiwata, S. Characterization of single actomyosin rigor bonds: load dependence of lifetime and mechanical properties. *Biophysical journal* **2000,** *79*, 962-74.
55. Iyer, S.; Woodworth, C. D.; Gaikwad, R. M.; Kievsky, Y. Y.; Sokolov, I. Towards nonspecific detection of malignant cervical cells with fluorescent silica beads. *Small (Weinheim an der Bergstrasse, Germany)* **2009,** *5*, 2277-84.
56. Ebner, A.; Kienberger, F.; Kada, G.; Stroh, C. M.; Geretschläger, M.; Kamruzzahan, a. S. M.; Wildling, L.; Johnson, W. T.; Ashcroft, B.; Nelson, J.; Lindsay, S. M.; Gruber, H. J.; Hinterdorfer, P. Localization of single avidin-biotin interactions using simultaneous topography and molecular recognition imaging. *Chemphyschem : a European journal of chemical physics and physical chemistry* **2005,** *6*, 897-900.
57. Abu-Lail, N. I.; Camesano, T. a. Polysaccharide properties probed with atomic force microscopy. *Journal of microscopy* **2003,** *212*, 217-38.
58. Grier, D. G. A revolution in optical manipulation. *Nature* **2003,** *424* (6950), 810-816.
59. Svoboda, K.; Block, S. M. Biological applications of optical forces. *Annual review of biophysics and biomolecular structure* **1994,** *23* (1), 247-285.
60. Watanabe, T. M.; Iwane, A. H.; Tanaka, H.; Ikebe, M.; Yanagida, T. Mechanical Characterization of One-Headed Myosin-V Using Optical Tweezers. *PLoS ONE* **2010,** *5*, e12224.
61. Mirsaidov, U.; Scrimgeour, J.; Timp, W.; Beck, K.; Mir, M.; Matsudaira, P.; Timp, G. Live cell lithography: using optical tweezers to create synthetic tissue. *Lab on a chip* **2008,** *8*, 2174-81.
62. Valignat, M. P.; Theodoly, O.; Crocker, J. C.; Russel, W. B.; Chaikin, P. M. Reversible self-assembly and directed assembly of DNA-linked micrometer-sized colloids. *Proc Natl Acad Sci U S A* **2005,** *102* (12), 4225-9.
63. Biancaniello, P.; Kim, A.; Crocker, J. Colloidal Interactions and Self-Assembly Using DNA Hybridization. *Physical Review Letters* **2005,** *94*, 94-97.
64. Wu, K.-T.; Feng, L.; Sha, R.; Dreyfus, R.; Grosberg, A. Y.; Seeman, N. C.; Chaikin, P. M. Kinetics of DNA-coated sticky particles. *Physical Review E* **2013,** *88*, 022304.
65. Di Michele, L.; Varrato, F.; Kotar, J.; Nathan, S. H.; Foffi, G.; Eiser, E. Multistep kinetic self-assembly of DNA-coated colloids. *Nature communications* **2013,** *4*, 2007.
66. Everett, W. N.; Beltran-Villegas, D. J.; Bevan, M. A. Concentrated diffusing colloidal probes of Ca2+-dependent cadherin interactions. *Langmuir : the ACS journal of surfaces and colloids* **2010,** *26*, 18976-84.
67. Schoen, A. P.; Hommersom, B.; Heilshorn, S. C.; Leunissen, M. E. Tuning colloidal association with specific peptide interactions. *Soft Matter* **2013,** *9*, 6781.

68. Hiddessen, A. L.; Rodgers, S. D.; Weitz, D. A.; Hammer, D. A. Assembly of Binary Colloidal Structures via Specific Biological Adhesion. *Langmuir* **2000,** *16*, 9744-9753.
69. Bahukudumbi, P.; Bevan, M. A. Imaging energy landscapes with concentrated diffusing colloidal probes. *The Journal of chemical physics* **2007,** *126*, 244702.
70. Eichmann, S. L.; Meric, G.; Swavola, J. C.; Bevan, M. A. Diffusing colloidal probes of protein-carbohydrate interactions. *Langmuir : the ACS journal of surfaces and colloids* **2013,** *29* (7), 2299-310.
71. Everett, W. N.; Wu, H.-j.; Anekal, S. G.; Sue, H.-j.; Bevan, M. A. Diffusing Colloidal Probes of Protein and Synthetic Macromolecule Interactions. *Biophysical Journal* **2007,** *92*, 1005-1013.
72. Everett, W. N.; Bevan, M. a. kT-Scale interactions between supported lipid bilayers. *Soft Matter* **2014,** *10*, 332.
73. Wang, W.; Donini, O.; Reyes, C. M.; Kollman, P. A. Biomolecular simulations: recent developments in force fields, simulations of enzyme catalysis, protein-ligand, protein-protein, and protein-nucleic acid noncovalent interactions. *Annual review of biophysics and biomolecular structure* **2001,** *30*, 211-43.
74. Martinez-Veracoechea, F. J.; Mognetti, B. M.; Angioletti-Uberti, S.; Varilly, P.; Frenkel, D.; Dobnikar, J. Designing stimulus-sensitive colloidal walkers. *Soft matter* **2014**.
75. Mladek, B. M.; Fornleitner, J.; Martinez-Veracoechea, F. J.; Dawid, A.; Frenkel, D. Procedure to construct a multi-scale coarse-grained model of DNA-coated colloids from experimental data. *Soft Matter* **2013,** *9*, 7342.
76. Varilly, P.; Angioletti-Uberti, S.; Mognetti, B. M.; Frenkel, D. A general theory of DNA-mediated and other valence-limited colloidal interactions. *The Journal of chemical physics* **2012,** *137*, 094108.
77. Irvine, D. J.; Hue, K.-A.; Mayes, A. M.; Griffith, L. G. Simulations of cell-surface integrin binding to nanoscale-clustered adhesion ligands. *Biophysical journal* **2002,** *82*, 120-32.
78. Hagy, M. C.; Wang, S.; Dormidontova, E. E. Optimization of functionalized polymer layers for specific targeting of mobile receptors on cell surfaces. *Langmuir : the ACS journal of surfaces and colloids* **2008,** *24*, 13037-47.
79. Dzyaloshinskii, I. E.; Lifshitz, E. M.; Pitaevskii, L. P. The general theory of van der Waals forces. *Advances in Physics* **1961,** *10*, 165-209.
80. Bevan, M. a.; Prieve, D. C. Direct Measurement of Retarded van der Waals Attraction. *Langmuir* **1999,** *15*, 7925-7936.
81. Prieve, D. C.; Russel, W. B. Simplified Predictions of Hamaker Constants from Lifshitz Theory. *J. Colloid Interface Sci.* **1988,** *125*, 1.
82. Bevan, M. A.; Prieve, D. C. Direct measurement of retarded van der Waals attraction. *Langmuir* **1999,** *15* (23), 7925-7936.
83. Milner, S. T. Compressing Polymer Brushes - a Quantitative Comparison of Theory and Experiment. *Europhys. Lett.* **1988,** *7* (8), 695-699.
84. Milner, S. T. Polymer Brushes. *Science* **1991,** *251* (4996), 905-914.
85. Milner, S. T.; Witten, T. A.; Cates, M. E. Theory of the Grafted Polymer Brush. *Macromolecules* **1988,** *21* (8), 2610-2619.

86. Li, D. C.; Rogers, J.; Biswal, S. L. Probing the Stability of Magnetically Assembled DNA-Linked Colloidal Chains. *Langmuir* **2009,** *25* (16), 8944-8950.
87. Konowalow, D. D.; Hirschfelder, J. O. Intermolecular Potential Functions for Nonpolar Molecules. *Physics of Fluids* **1961,** *4*, 629.
88. Goldman, A. J.; Cox, R. G.; Brenner, H. Slow viscous motion of a sphere parallel to a plane wall—II Couette flow. *Chemical Engineering Science* **1967,** *22*, 653-660.
89. Anekal, S. G.; Bevan, M. a. Self-diffusion in submonolayer colloidal fluids near a wall. *The Journal of Chemical Physics* **2006,** *125*, 34906.
90. Alexander, B. M.; Prieve, D. C. Hydrodynamic Technique for Measurement of Colloidal Forces. *Langmuir : the ACS journal of surfaces and colloids* **1987,** *3* (5), 788-795.
91. Pagac, E. S.; Tilton, R. D.; Prieve, D. C. Hindered Mobility of A Rigid Sphere Near A Wall. *Chemical Engineering Communications* **1996,** *148-150*, 105-122.
92. Bevan, M. a.; Prieve, D. C. Hindered diffusion of colloidal particles very near to a wall: Revisited. *The Journal of Chemical Physics* **2000,** *113*, 1228.
93. Happel, J.; Brenner, H. Low Reynolds Number Hydrodynamics. In *Englewood Cliffs NJ*, 1965; Vol. 40, pp 329-331.
94. Anekal, S. G.; Bevan, M. a. Interpretation of conservative forces from Stokesian dynamic simulations of interfacial and confined colloids. *The Journal of Chemical Physics* **2005,** *122*, 34903.
95. Ristenpart, W. D.; Aksay, I. a.; Saville, D. a. Assembly of colloidal aggregates by electrohydrodynamic flow: Kinetic experiments and scaling analysis. *Physical Review E* **2004,** *69*, 021405.
96. Smoluchowski, M. *Z Physik Chem* **1916,** *92* (129).
97. Hardt, S. L. Rates of diffusion controlled reactions in one, two and three dimensions. *Biophysical Chemistry* **1979,** *10*, 239-243.
98. Fuchs, N. *Z Physik* **1934,** *89* (736).
99. Hogg, R.; Yang, K. C. Secondary coagulation. *Journal of Colloid and Interface Science* **1976,** *56*, 573-576.
100. Luo, H.; Sharp, K. On the calculation of absolute macromolecular binding free energies. *Proceedings of the National Academy of Sciences of the United States of America* **2002,** *99*, 10399-404.
101. Bevan, M. A.; Petris, S. N.; Chan, D. Y. C. Solvent Quality Dependent Continuum van der Waals. *Langmuir : the ACS journal of surfaces and colloids* **2002,** *104*, 7845-7852.
102. Frenkel, D.; Smit, B. Understanding molecular simulation: from algorithms to applications. *Academic Press* **2002,** *New York,* .
103. Liu, J.; Luijten, E. Rejection-Free Geometric Cluster Algorithm for Complex Fluids. *Physical Review Letters* **2004,** *92*, 1-4.
104. Luijten, E.; Liu, J. Cluster Algorithms : Beyond Suppression of Critical Slowing Down. **2003**, 225-231.
105. Torrie, G. M.; Valleau, J. P. Monte Carlo Free Energy Estimates Using Non-Boltzmann Sampling: Application to the Sub-Critical Lennard-Jones Fluid. *Chemical Physics Letters* **1974,** *28*, 578-581.

106. Bevan, M. A.; Prieve, D. C. Forces and Hydrodynamic Interactions between Polystyrene Surfaces with Adsorbed PEO−PPO−PEO. *Langmuir* **2000,** *16*, 9274-9281.
107. van Helden, A. K.; Jansen, J. W.; Vrij, A. Preparation and Characterization of Spherical Monodisperse Silica Dispersions in Non-Aqueous Solvents. *J. Colloid Interface Sci.* **1981,** *81* (2), 354-368.
108. Das, S.; Banquy, X.; Zappone, B.; Greene, G. W.; Jay, G. D.; Israelachvili, J. N. Synergistic Interactions between Grafted Hyaluronic Acid and Lubricin Provide Enhanced Wear Protection and Lubrication. **2013**.
109. Elender, G.; Kühner, M.; Sackmann, E. Functionalisation of Si/SiO2 and glass surfaces with ultrathin dextran films and deposition of lipid bilayers. *Biosensors & bioelectronics* **1996,** *11*, 565-77.
110. Hu, M.; Novo, C.; Funston, A.; Wang, H.; Staleva, H.; Zou, S.; Mulvaney, P.; Hartland, G. V. Dark-field microscopy studies of single metal nanoparticles : understanding the factors that influence the linewidth of the localized surface plasmon resonance. **2008**, 1949-1960.
111. Wu, H.-J.; Bevan, M. a. Direct measurement of single and ensemble average particle-surface potential energy profiles. *Langmuir : the ACS journal of surfaces and colloids* **2005,** *21*, 1244-54.
112. Crocker, J. C.; Grier, D. G. Methods of Digital Video Microscopy for Colloidal Studies. *Journal of Colloid and Interface Science* **1996,** *179*, 298-310.
113. Arvo, J. Fast Random Rotation Matrices. *Graphics Gems III* **1992**, 117-120.
114. Cummings, R.; Liu, F. Galectins. In *Essentials of Glycobiology*, 2nd ed.; Varki, A.; Cummings, R.; Esko, J., Eds.; Cold Spring Harbor, 2009.
115. Gorelik, E.; Galili, U.; Raz, A. On the role of cell surface carbohydrates and their binding proteins (lectins) in tumor metastasis. *Cancer Metastasis Reviews* **2001,** *20*, 245-77.
116. Rabinovich, G. a.; Toscano, M. a. Turning 'sweet' on immunity: galectin-glycan interactions in immune tolerance and inflammation. *Nature reviews. Immunology* **2009,** *9*, 338-52.
117. Toole, B. P. Hyaluronan: from extracellular glue to pericellular cue. *Nature reviews. Cancer* **2004,** *4*, 528-39.
118. Diggle, S. P.; Stacey, R. E.; Dodd, C.; Cámara, M.; Williams, P.; Winzer, K. The galactophilic lectin, LecA, contributes to biofilm development in Pseudomonas aeruginosa. *Environmental Microbiology* **2006,** *8*, 1095-1104.
119. Flemming, H.-c.; Wingender, J. The biofilm matrix. *Nature Reviews* **2010,** *8*, 623-633.
120. Sato, Y.; Yoshioka, K.; Murakami, T.; Yoshimoto, S.; Niwa, O. Design of biomolecular interface for detecting carbohydrate and lectin weak interactions. *Langmuir : the ACS journal of surfaces and colloids* **2012,** *28*, 1846-51.
121. Scurr, D. J.; Horlacher, T.; Oberli, M. a.; Werz, D. B.; Kroeck, L.; Bufali, S.; Seeberger, P. H.; Shard, A. G.; Alexander, M. R. Surface characterization of carbohydrate microarrays. *Langmuir : the ACS journal of surfaces and colloids* **2010,** *26*, 17143-55.

122. Matsubara, T.; Iijima, K.; Nakamura, M.; Taki, T.; Okahata, Y.; Sato, T. Specific binding of GM1-binding peptides to high-density GM1 in lipid membranes. *Langmuir : the ACS journal of surfaces and colloids* **2007,** *23*, 708-14.
123. Castro, L. B. R.; Kappl, M.; Petri, D. F. S. Adhesion forces between hybrid colloidal particles and concanavalin A. *Langmuir : the ACS journal of surfaces and colloids* **2006,** *22*, 3757-62.
124. Evans, E.; Leung, a.; Hammer, D.; Simon, S. Chemically distinct transition states govern rapid dissociation of single L-selectin bonds under force. *Proceedings of the National Academy of Sciences of the United States of America* **2001,** *98*, 3784-9.
125. Dörig, P.; Ossola, D.; Truong, A. M.; Graf, M.; Stauffer, F.; Vörös, J.; Zambelli, T. Exchangeable Colloidal AFM Probes for the Quantification of Irreversible and Long-Term Interactions. *Biophysical journal* **2013,** *105*, 463-72.
126. Eichmann, S. L.; Meric, G.; Swavola, J. C.; Bevan, M. A. Diffusing Colloidal Probes of Protein − Carbohydrate Interactions. *Langmuir : the ACS journal of surfaces and colloids* **2013,** *29*, 2299-2310.
127. Everett, W. N.; Beltran-Villegas, D. J.; Bevan, M. a. Concentrated diffusing colloidal probes of Ca2+-dependent cadherin interactions. *Langmuir : the ACS journal of surfaces and colloids* **2010,** *26*, 18976-84.
128. Liang, F.; Pan, T.; Sevick-Muraca, E. M. Measurements of FRET in a glucose-sensitive affinity system with frequency-domain lifetime spectroscopy. *Photochemistry and photobiology* **2005,** *81*, 1386-94.
129. Oda, Y.; Kasai, K.; Ishii, S. Studies on the specific interaction of concanavalin A and saccharides by affinity chromatography. Application of quantitative affinity chromatography to a multivalent system. *Journal of biochemistry* **1981,** *89*, 285-96.
130. Shimura, K.; Kasai, K. Determination of the affinity constants of concanavalin A for monosaccharides by fluorescence affinity probe capillary electrophoresis. *Analytical biochemistry* **1995,** *227*, 186-94.
131. Wang, X.; Ramström, O.; Yan, M. Quantitative analysis of multivalent ligand presentation on gold glyconanoparticles and the impact on lectin binding. *Analytical chemistry* **2010,** *82*, 9082-9.
132. Slutsky, M.; Mirny, L. a. Kinetics of protein-DNA interaction: facilitated target location in sequence-dependent potential. *Biophysical journal* **2004,** *87*, 4021-35.
133. Selkoe, D. J. Folding proteins in fatal ways. *Nature* **2003,** *426*, 900-4.
134. Toole, B. P. Hyaluronan: from extracellular glue to pericellular cue. *Nature reviews. Cancer* **2004,** *4*, 528-39.
135. Hamachi, I.; Nagase, T.; Shinkai, S.; V, K. U. A General Semisynthetic Method for Fluorescent Saccharide-Biosensors Based on a Lectin. *Journal of the American Chemical Society* **2000**, 12065-12066.
136. Simnick, A. J.; Valencia, C. A.; Liu, R.; Chilkoti, A. Morphing low-affinity ligands into high-avidity nanoparticles by thermally triggered self-assembly of a genetically encoded polymer. *ACS Nano* **2010,** *4*, 2217-27.
137. Weiss, S. Fluorescence Spectroscopy of Single Biomolecules. *Science* **1999,** *283*, 1676-1683.

138. Smith, E. A.; Thomas, W. D.; Kiessling, L. L.; Corn, R. M. Surface plasmon resonance imaging studies of protein-carbohydrate interactions. *Journal of the American Chemical Society* **2003,** *125*, 6140-8.
139. Li, F.; Redick, S. D.; Erickson, H. P.; Moy, V. T. Force measurements of the alpha5beta1 integrin-fibronectin interaction. *Biophysical journal* **2003,** *84*, 1252-62.
140. Ounkomol, C.; Yamada, S.; Heinrich, V. Single-cell adhesion tests against functionalized microspheres arrayed on AFM cantilevers confirm heterophilic E- and N-cadherin binding. *Biophysical journal* **2010,** *99*, L100-2.
141. Wang, S.; Dormidontova, E. E. Nanoparticle design optimization for enhanced targeting: Monte Carlo simulations. *Biomacromolecules* **2010,** *11*, 1785-95.
142. Moore, N. W.; Kuhl, T. L. The role of flexible tethers in multiple ligand-receptor bond formation between curved surfaces. *Biophysical Journal* **2006,** *91*, 1675-87.
143. Irvine, D. J.; Hue, K.-A.; Mayes, A. M.; Griffith, L. G. Simulations of cell-surface integrin binding to nanoscale-clustered adhesion ligands. *Biophysical Journal* **2002,** *82*, 120-32.
144. Wu, Y.; Honig, B.; Ben-Shaul, A. Theory and simulations of adhesion receptor dimerization on membrane surfaces. *Biophysical journal* **2013,** *104*, 1221-9.
145. J., N.; Liu, X. Y. Protein Interactions in Undersaturated and Supersaturated Solutions: A Study Using Light and X-Ray Scattering. *Biophysical Journal* **2003,** *84* (1), 523-532.
146. Piazza, R.; Peyre, V.; Degiorgio, V. "Sticky hard spheres" model of proteins near crystallization: A test based on the osmotic compressibility. *Physical Reveiw E* **1998,** *58* (3), 2733-2736.
147. Ravichandran, S.; Talbot, J. Mobility of Adsorbed Proteins: A Brownian Dynamics Study. *Biophysical Journal* **2000,** *78* (1), 110-120.
148. Dickinson, E. Adsorption of Sticky Hard Spheres: Relevance to Protein Competitive Adsorption. *Journal of the Chemical Society. Faraday Transactions I* **1992,** *88* (24), 3561-3565.
149. Bryce, R. A.; Hillier, I. H.; Naismith, J. H. Carbohydrate-protein recognition: molecular dynamics simulations and free energy analysis of oligosaccharide binding to concanavalin A. *Biophysical Journal* **2001,** *81*, 1373-88.
150. Woo, H.-j.; Roux, B. Calculation of absolute protein – ligand binding free. *Proceedings of the National Academy of Sciences of the United States of America* **2005,** *102* (19), 6825-6830.
151. Marsili, S.; Barducci, A.; Chelli, R.; Procacci, P.; Schettino, V. Self-healing umbrella sampling: a non-equilibrium approach for quantitative free energy calculations. *The Journal of Physical Chemistry B* **2006,** *110*, 14011-3.
152. Beltran-Villegas, D. J.; Bevan, M. a. Free energy landscapes for colloidal crystal assembly. *Soft Matter* **2011,** *7*, 3280.
153. Blaak, R.; Auer, S.; Frenkel, D.; Löwen, H. Crystal Nucleation of Colloidal Suspensions under Shear. *Physical Review Letters* **2004,** *93*, 4-7.
154. Virnau, P.; Muller, M. Calculation of free energy through successive umbrella sampling. *Journal of Chemical Physics* **2004,** *120* (23), 10925-30.

155. Malherbe, J. G.; Amokrane, S. Asymmetric mixture of hard particles with Yukawa attraction between unlike ones : a cluster algorithm simulation study *Molecular Physics* **1999,** *97*, 677-683.
156. Vink, R. L. C.; Horbach, J. Critical behaviour and interfacial fluctuations in a phase-separating model colloid–polymer mixture: grand canonical Monte Carlo simulations. *Journal of Physics: Condensed Matter* **2004,** *16*, 3807-3820.
157. Aslan, K.; Lakowicz, J. R.; Geddes, C. D. Nanogold Plasmon Resonance-Based Glucose Sensing. 2. Wavelength-Ratiometric Resonance Light Scattering. *Analytical Biochemistry* **2005,** *77*, 2007-2014.
158. Chern, C. S.; Lee, C. K.; Tsai, Y. J.; Ho, C. C. Colloidal stability of dextran-modified latex particles toward adsorption of concanavalin A. *Colloid & Polymer Science* **1998,** *276*, 427-433.
159. Zhang, J.; Roll, D. Aggregation of silver nanoparticle-dextran adducts with concanavalin A and competitive complexation with glucose. *The Journal of Physical Chemistry B* **2004,** *108*, 12210-12214.
160. Barone, P. W.; Strano, M. S. Reversible Control of Carbon Nanotube Aggregation for a Glucose Affinity Sensor. *Angewandte Chemie* **2006,** *118* (48), 8318-8321.
161. Liang, F.; Pan, T.; Sevick-Muraca, E. M. Measurements of FRET in a glucose-sensitive affinity system with frequency-domain lifetime spectroscopy. *Photochemistry and photobiology* **2005,** *81* (6), 1386-94.
162. Oda, Y.; Kasai, K.-i.; Ishii, S.-i. Studies on the Specific Interaction of Concanavalin A and Saccharides by Affinity Chromotography to a Multivalent System. *The Journal of Biochemistry* **1981,** *89* (1), 285-296.
163. Martinez-Veracoechea, F. J.; Frenkel, D. Designing super selectivity in multivalent nano-particle binding. *Proceedings of the National Academy of Sciences of the United States of America* **2011,** *108*, 10963-8.
164. Nel, A. E.; Mädler, L.; Velegol, D.; Xia, T.; Hoek, E. M. V.; Somasundaran, P.; Klaessig, F.; Castranova, V.; Thompson, M. Understanding biophysicochemical interactions at the nano-bio interface. *Nature materials* **2009,** *8*, 543-557.
165. Israelachvili, J. Differences between non-specific and bio-specific, and between equilibrium and non-equilibrium, interactions in biological systems. *Quarterly reviews of biophysics* **2005,** *38*, 331-337.
166. Giebel, K.; Bechinger, C.; Herminghaus, S.; Riedel, M.; Leiderer, P.; Weiland, U.; Bastmeyer, M. Imaging of cell/substrate contacts of living cells with surface plasmon resonance microscopy. *Biophysical journal* **1999,** *76*, 509-516.
167. Hoover, D. K.; Lee, E.-J.; Yousaf, M. N. Total internal reflection fluorescence microscopy of cell adhesion on patterned self-assembled monolayers on gold. *Langmuir : the ACS journal of surfaces and colloids* **2009,** *25*, 2563-2566.
168. Parsons, J. T.; Horwitz, A. R.; Schwartz, M. A. Cell adhesion: integrating cytoskeletal dynamics and cellular tension. *Nature reviews. Molecular cell biology* **2010,** *11*, 633-643.
169. Steyer, J. A.; Almers, W. A real-time view of life within 100 nm of the plasma membrane. *Nature reviews. Molecular cell biology* **2001,** *2*, 268-275.
170. van der Merwe, P. A.; Barclay, A. N. Analysis of cell-adhesion molecule interactions using surface plasmon resonance. *Current Opinion in Immunology* **1996,** *8*, 257-261.

171. Ziblat, R.; Lirtsman, V.; Davidov, D.; Aroeti, B. Infrared surface plasmon resonance: a novel tool for real time sensing of variations in living cells. *Biophysical journal* **2006,** *90*, 2592-2599.
172. Eichmann, S. L.; Meric, G.; Swavola, J. C.; Bevan, M. A. Diffusing colloidal probes of protein-carbohydrate interactions. *Langmuir : the ACS journal of surfaces and colloids* **2013,** *29*, 2299-2310.
173. Mailänder, V.; Landfester, K. Interaction of nanoparticles with cells. *Biomacromolecules* **2009,** *10*, 2379-400.
174. Chauhan, V. P.; Jain, R. K. Strategies for advancing cancer nanomedicine. *Nature materials* **2013,** *12*, 958-62.
175. Eichmann, S. L.; Bevan, M. A. Direct measurements of protein-stabilized gold nanoparticle interactions. *Langmuir : the ACS journal of surfaces and colloids* **2010,** *26*, 14409-14413.
176. Das, S.; Banquy, X.; Zappone, B.; Greene, G. W.; Jay, G. D.; Israelachvili, J. N. Synergistic interactions between grafted hyaluronic acid and lubricin provide enhanced wear protection and lubrication. *Biomacromolecules* **2013,** *14*, 1669-77.
177. Agus, D. B.; Alexander, J. F.; Arap, W.; Ashili, S.; Aslan, J. E.; Austin, R. H.; Backman, V.; Bethel, K. J.; Bonneau, R.; Chen, W.-C.; Chen-Tanyolac, C.; Choi, N. C.; Curley, S. A.; Dallas, M.; Damania, D.; Davies, P. C. W.; Decuzzi, P.; Dickinson, L.; Estevez-Salmeron, L.; Estrella, V.; Ferrari, M.; Fischbach, C.; Foo, J.; Fraley, S. I.; Frantz, C.; Fuhrmann, A.; Gascard, P.; Gatenby, R. A.; Geng, Y.; Gerecht, S.; Gillies, R. J.; Godin, B.; Grady, W. M.; Greenfield, A.; Hemphill, C.; Hempstead, B. L.; Hielscher, A.; Hillis, W. D.; Holland, E. C.; Ibrahim-Hashim, A.; Jacks, T.; Johnson, R. H.; Joo, A.; Katz, J. E.; Kelbauskas, L.; Kesselman, C.; King, M. R.; Konstantopoulos, K.; Kraning-Rush, C. M.; Kuhn, P.; Kung, K.; Kwee, B.; Lakins, J. N.; Lambert, G.; Liao, D.; Licht, J. D.; Liphardt, J. T.; Liu, L.; Lloyd, M. C.; Lyubimova, A.; Mallick, P.; Marko, J.; McCarty, O. J. T.; Meldrum, D. R.; Michor, F.; Mumenthaler, S. M.; Nandakumar, V.; O'Halloran, T. V.; Oh, S.; Pasqualini, R.; Paszek, M. J.; Philips, K. G.; Poultney, C. S.; Rana, K.; Reinhart-King, C. A.; Ros, R.; Semenza, G. L.; Senechal, P.; Shuler, M. L.; Srinivasan, S.; Staunton, J. R.; Stypula, Y.; Subramanian, H.; Tlsty, T. D.; Tormoen, G. W.; Tseng, Y.; van Oudenaarden, A.; Verbridge, S. S.; Wan, J. C.; Weaver, V. M.; Widom, J.; Will, C.; Wirtz, D.; Wojtkowiak, J.; Wu, P.-H. A physical sciences network characterization of non-tumorigenic and metastatic cells. *Scientific reports* **2013,** *3*, 1449.
178. Boddohi, S.; Kipper, M. J. Engineering nanoassemblies of polysaccharides. *Advanced materials (Deerfield Beach, Fla.)* **2010,** *22*, 2998-3016.
179. Fu, B. M.; Tarbell, J. M. Mechano-sensing and transduction by endothelial surface glycocalyx: composition, structure, and function. *Wiley interdisciplinary reviews. Systems biology and medicine* **2013,** *5*, 381-90.
180. Qazi, H.; Palomino, R.; Shi, Z.-D.; Munn, L. L.; Tarbell, J. M. Cancer cell glycocalyx mediates mechanotransduction and flow-regulated invasion. *Integrative biology : quantitative biosciences from nano to macro* **2013,** *5*, 1334-43.
181. Monopoli, M. P.; Walczyk, D.; Campbell, A.; Elia, G.; Lynch, I.; Bombelli, F. B.; Dawson, K. A. Physical-chemical aspects of protein corona: relevance to in vitro

and in vivo biological impacts of nanoparticles. *Journal of the American Chemical Society* **2011,** *133*, 2525-34.
182. Jedlovszky-Hajdú, A.; Bombelli, F. B.; Monopoli, M. P.; Tombácz, E.; Dawson, K. A. Surface coatings shape the protein corona of SPIONs with relevance to their application in vivo. *Langmuir : the ACS journal of surfaces and colloids* **2012,** *28*, 14983-91.
183. Varshosaz, J. Dextran conjugates in drug delivery. In *Expert Opinion on Drug Delivery*, 2012; Vol. 9, pp 509-523.
184. Kozak, D.; Chen, A.; Bax, J.; Trau, M. Protein resistance of dextran and dextran-poly(ethylene glycol) copolymer films. *Biofouling* **2011,** *27*, 497-503.
185. Pasut, G.; Veronese, F. M. PEG conjugates in clinical development or use as anticancer agents: An overview. In *Advanced Drug Delivery Reviews*, 2009; Vol. 61, pp 1177-1188.
186. Banerji, S.; Wright, A. J.; Noble, M.; Mahoney, D. J.; Campbell, I. D.; Day, A. J.; Jackson, D. G. Structures of the Cd44-hyaluronan complex provide insight into a fundamental carbohydrate-protein interaction. *Nature structural & molecular biology* **2007,** *14*, 234-9.
187. Curtis, A.; Wilkinson, C. Topographical control of cells. In *Biomaterials*, 1997; Vol. 18, pp 1573-1583.
188. Brannon-Peppas, L.; Blanchette, J. O. Nanoparticle and targeted systems for cancer therapy. *Advanced Drug Delivery Reviews* **2012,** *64*, 206-212.
189. Schrama, D.; Reisfeld, R. a.; Becker, J. C. Antibody targeted drugs as cancer therapeutics. *Nature reviews. Drug discovery* **2006,** *5*, 147-59.
190. Olsen, N. J.; Stein, C. M. New drugs for rheumatoid arthritis. *The New England journal of medicine* **2004,** *350*, 2167-79.
191. Sievers, E. L.; Senter, P. D. Antibody-drug conjugates in cancer therapy. *Annual review of medicine* **2013,** *64*, 15-29.
192. Rose, J. W.; Foley, J.; Carlson, N. Monoclonal antibody treatments for multiple sclerosis. *Current neurology and neuroscience reports* **2008,** *8*, 419-26.
193. Arosio, D.; Manzoni, L.; Araldi, E. M. V.; Scolastico, C. Cyclic RGD functionalized gold nanoparticles for tumor targeting. *Bioconjugate chemistry* **2011,** *22*, 664-72.
194. Kunjachan, S.; Pola, R.; Gremse, F.; Theek, B.; Ehling, J.; Moeckel, D.; Hermanns-Sachweh, B.; Pechar, M.; Ulbrich, K.; Hennink, W. E.; Storm, G.; Lederle, W.; Kiessling, F.; Lammers, T. Passive versus Active Tumor Targeting Using RGD- and NGR-Modified Polymeric Nanomedicines. *Nano letters* **2014**.
195. Simnick, A. J.; Valencia, C. A.; Liu, R.; Chilkoti, A. Morphing low-affinity ligands into high-avidity nanoparticles by thermally triggered self-assembly of a genetically encoded polymer. *ACS nano* **2010,** *4*, 2217-27.
196. Bhang, S. H.; Won, N.; Lee, T.-J.; Jin, H.; Nam, J.; Park, J.; Chung, H.; Park, H.-S.; Sung, Y.-E.; Hahn, S. K.; Kim, B.-S.; Kim, S. Hyaluronic acid-quantum dot conjugates for in vivo lymphatic vessel imaging. *ACS nano* **2009,** *3*, 1389-98.
197. Cho, H.-J.; Yoon, H. Y.; Koo, H.; Ko, S.-H.; Shim, J.-S.; Lee, J.-H.; Kim, K.; Kwon, I. C.; Kim, D.-D. Self-assembled nanoparticles based on hyaluronic acid-ceramide (HA-CE) and Pluronic® for tumor-targeted delivery of docetaxel. *Biomaterials* **2011,** *32*, 7181-90.

198. Choi, K. Y.; Chung, H.; Min, K. H.; Yoon, H. Y.; Kim, K.; Park, J. H.; Kwon, I. C.; Jeong, S. Y. Self-assembled hyaluronic acid nanoparticles for active tumor targeting. *Biomaterials* **2010,** *31*, 106-14.
199. Choi, K. Y.; Yoon, H. Y.; Kim, J.-H.; Bae, S. M.; Park, R.-W.; Kang, Y. M.; Kim, I.-S.; Kwon, I. C.; Choi, K.; Jeong, S. Y.; Kim, K.; Park, J. H. Smart nanocarrier based on PEGylated hyaluronic acid for cancer therapy. *ACS nano* **2011,** *5*, 8591-9.
200. Platt, V. M.; Szoka, F. C. Anticancer therapeutics: targeting macromolecules and nanocarriers to hyaluronan or CD44, a hyaluronan receptor. *Molecular pharmaceutics* **2009,** *5*, 474-86.
201. Moore, N. W.; Kuhl, T. L. The role of flexible tethers in multiple ligand-receptor bond formation between curved surfaces. *Biophysical journal* **2006,** *91*, 1675-87.
202. Zhang, C.-z.; Wang, Z.-g. Polymer-tethered ligand-receptor interactions between surfaces II. *Langmuir : the ACS journal of surfaces and colloids* **2007,** *23*, 13024-39.
203. Wang, S.; Dormidontova, E. E. Nanoparticle design optimization for enhanced targeting: Monte Carlo simulations. *Biomacromolecules* **2010,** *11*, 1785-1795.
204. Sarvestani, A. S. The effect of substrate rigidity on the assembly of specific bonds at biological interfaces. *Soft Matter* **2013,** *9*, 5927.
205. Liu, J.; Weller, G. E. R.; Zern, B.; Ayyaswamy, P. S.; Eckmann, D. M.; Muzykantov, V. R.; Radhakrishnan, R. Computational model for nanocarrier binding to endothelium validated using in vivo, in vitro, and atomic force microscopy experiments. *Proceedings of the National Academy of Sciences of the United States of America* **2010,** *107*, 16530-5.
206. Martinez-Veracoechea, F. J.; Frenkel, D. Designing super selectivity in multivalent nano-particle binding. *Proceedings of the National Academy of Sciences of the United States of America* **2011,** *108*, 10963-10968.
207. Parsons, M.; Messent, A. J.; Humphries, J. D.; Deakin, N. O.; Humphries, M. J. Quantification of integrin receptor agonism by fluorescence lifetime imaging. *Journal of cell science* **2008,** *121*, 265-71.
208. Meinecke, R.; Meyer, B. Determination of the Binding Specificity of an Integral Membrane Protein by Saturation Transfer Difference NMR: RGD Peptide Ligands Binding to Integrin α IIb β 3 †. *Journal of Medicinal Chemistry* **2001,** *44*, 3059-3065.
209. Liu, L.-k.; Finzel, B. C. Fragment-Based Identification of an Inducible Binding Site on Cell Surface Receptor CD44 for the Design of Protein-Carbohydrate Interaction Inhibitors. *Journal of medicinal chemistry* **2014,** *57*, 2714-25.
210. Wild, M. K.; Huang, M. C.; Schulze-Horsel, U.; van der Merwe, P. a.; Vestweber, D. Affinity, kinetics, and thermodynamics of E-selectin binding to E-selectin ligand-1. *The Journal of biological chemistry* **2001,** *276*, 31602-12.
211. Vellon, L.; Menendez, J. a.; Lupu, R. AlphaVbeta3 integrin regulates heregulin (HRG)-induced cell proliferation and survival in breast cancer. *Oncogene* **2005,** *24*, 3759-73.
212. Pyne, S.; Hu, X.; Wang, K.; Rossin, E.; Lin, T.-I.; Maier, L. M.; Baecher-Allan, C.; McLachlan, G. J.; Tamayo, P.; Hafler, D. a.; De Jager, P. L.; Mesirov, J. P. Automated high-dimensional flow cytometric data analysis. *Proceedings of the*

National Academy of Sciences of the United States of America **2009,** *106*, 8519-24.
213. Irish, J. M.; Kotecha, N.; Nolan, G. P. Mapping normal and cancer cell signalling networks: towards single-cell proteomics. *Nature reviews. Cancer* **2006,** *6*, 146-55.
214. Alves, C. S.; Burdick, M. M.; Thomas, S. N.; Pawar, P.; Konstantopoulos, K. The dual role of CD44 as a functional P-selectin ligand and fibrin receptor in colon carcinoma cell adhesion. *American journal of physiology. Cell physiology* **2008,** *294*, C907-16.
215. Eichmann, S. L.; Meric, G.; Swavola, J. C.; Bevan, M. A. Di ff using Colloidal Probes of Protein − Carbohydrate Interactions. **2013**.
216. Mac Gabhann, F.; Yang, M. T.; Popel, A. S. Monte Carlo simulations of VEGF binding to cell surface receptors in vitro. *Biochimica et biophysica acta* **2005,** *1746*, 95-107.

VITA

Name:	Gregg A. Duncan
Birth:	March, 05, 1987, Saint Petersburg, FL
Address:	Gregg A. Duncan may be contacted through Dr. M. A. Bevan at the Chemical and Biomolecular Engineering Department, Johns Hopkins University, Baltimore, MD 21218
Email Address:	gduncan@jhu.edu
Education:	B.S., Chemical Engineering, Florida State University, Tallahassee, FL, 2009
Research:	Light Scattering From Mixtures of Nanoparticles with S. Ramakrishnan, Florida State University, Tallahassee, FL, 2007-2009